DIPLOMA THESIS

VENIANAKI AIKATERINI

Thesis Supervisor
Prof. Dr. Ioannis K. Nikolos

Flow simulation around a double airfoil of a Formula Student vehicle.

MARCH, 2024

TECHNICAL UNIVERSITY OF CRETE
TURBOMACHINES & FLUID DYNAMICS
LABORATORY (TURBOLAB-TUC)

Technical Univeristy of Crete
SCHOOL OF PRODUCTION ENGINEERING & MANAGEMENT
TURBOMACHINES & FLUID DYNAMICS LABORATORY
(TURBOLAB-TUC)

DIPLOMA THESIS

Flow simulation around a double airfoil of a Formula Student vehicle.

VENIANAKI AIKATERINI

APPROVED BY THE COMMITTEE

Prof. Anargiros I. Delis

Prof. Ioannis K. Nikolos

Assoc. Prof. Georgios Arampatzis

CHANIA, MARCH 2024

To my grandmother Antigoni,

I want to express my heartfelt gratitude to the people who made this thesis possible. Firstly, a huge thank you to my thesis supervisor, Prof. Dr. Ioannis K. Nikolos, for his constant support, guidance, and mentorship. I would also like to thank my friends and family for always being there and supporting me throughout this journey.

Katerina

ABSTRACT

This thesis delves into an in-depth analysis of the aerodynamic performance of a double front wing, designed for the Formula Student competition vehicle of the Technical University of Crete. The design phase involved utilizing Computer-Aided Design (CAD) software, namely CATIA V5 R20, to create a detailed CAD model of the double front wing. Employing parametric modeling techniques ensured accuracy and adaptability in the design process. Subsequently, simulations were conducted using ANSYS 2019 R2 CFX, delving into the realm of computational fluid dynamics (CFD) to evaluate the airflow characteristics surrounding the double airfoil configuration.

The study commences with an exploration of aerodynamics in Formula 1 race cars, encompassing fundamental concepts such as downforce, lift, drag, and their respective coefficients. Theoretical foundations of wing theory are then examined, elucidating the influence of geometrical characteristics such as airfoil shape, camber, and thickness on aerodynamic performance. Further investigation extends to mechanics of boundary layers, ground effect phenomena, and utilization of aerodynamic devices in Formula 1 racing, including front and rear wings.

Transitioning into the design and development phase, the thesis adheres to a comprehensive design process aligned with Formula SAE regulations. Leveraging parametric modeling techniques within CATIA V5 R20 facilitates the creation of a detailed CAD model, imperative for subsequent flow simulation analyses.

The thesis progresses into iterative refinement, leveraging the initial simulation as a foundational point for innovation and improvement. Two additional models, representing enhanced iterations of the original design, are meticulously developed and subjected to simulation scrutiny. Design variations encompass the integration of Gurney Flaps and Vortex Generators. This iterative process utilizes insights gleaned from CFD analysis to inform design refinements, ultimately optimizing aerodynamic performance and efficiency.

This investigation not only enhances understanding of aerodynamic principles in Formula Student vehicle design but also offers practical insights into the design and simulation of race car aerodynamics. In conclusion, this thesis showcases a comprehensive approach to aerodynamic development and optimization of a front wing, harnessing advanced CAD and CFD techniques.

KEYWORDS

Aerodynamics

Airflow

Airfoils

ANSYS CFX

CAD

CATIA V5

CFD

Drag

Downforce

Formula 1

Formula SAE

Front Wing

Gurney Flap

Lift

Race Car

Rear Wing

Vortex Generators

Wing Profile

TABLE OF CONTENTS

LIST OF FIGURES

LIST OF NOMENCLATURE

A	Wing Area
AoA	Angle of Attack
c	Length of the airfoil chord
CAD	Computer Aided Design
CAE	Computer Aided Engineering
CAM	Computer Aided Manufacture
CATIA	Computer Aided Three-dimensional Interactive Application
C_D	Coefficient of Drag
CFD	Computational Fluid Dynamics
C_L	Coefficient of Lift
$C_{L,max}$	Maximum value of Lift Coefficient
CNC	Computer Numerical Control
C_P	Center of Pressure
D	Drag Force
DRS	Drag Reduction System
DS	Dassault Systèmes
FIA	Fédération Internationale del'Automobile
FSAE	Formula Society of Automotive Engineers
L	Lift Force
NACA	National Advisory Committee for Aeronautics
p	Pressure
PLM	Product Lifecycle Management
Re	Reynolds number
T	Temperature
t	Maximum thickness or depth of the airfoil
t_w	Shear stress at the wall

V	Velocity
VG	Vortex Generator
α_0	Lift slope
$\alpha_{L=0}$	Zero lift angle of attack
δ	Maximum camber of the airfoil
δ	Boundary layer thickness
μ	Coefficient of viscosity
ρ	Fluid Density

INTRODUCTION

CHAPTER 1

Formula 1 is one of the most renowned motor racing sports in the world, and its cars are marvels of modern engineering *(Figure 1.1)*. It is a complex and highly competitive sport that relies on a multitude of factors that converge to attain optimal performance. Among these crucial elements are power units, electronic systems, tire selection, suspension and transmission mechanisms, fuel efficiency, driver expertise, brakes, as well as the ever-changing variables of weather and track conditions. However, for the past few years, aerodynamics has been the focus of attention.

1.1 SAE International

SAE International, also known as the Society of Automotive Engineers, is a global association that brings together over 138,000 engineers and technical experts. It was founded in 1905 by Henry Ford, Andrew L. Riker, Edward Birdsall, and John Wilkinson. SAE's mission is to be the primary source of knowledge for the engineering profession, promoting both knowledge and expertise across a wide range of industries such as aerospace, automotive, and commercial vehicles (SAE International, 2024).

One of SAE International's notable contributions is the development of technical standards, commonly known as SAE standards. In the early 1900s, the emerging automobile and aviation industries recognized the need for engineering standards, and SAE International has been fulfilling that role ever since. As the world's leading authority in mobility standards development, SAE promotes and facilitates safety, productivity, reliability, efficiency, and certification throughout the mobility engineering industry.

SAE's rich history and global presence demonstrate its commitment to being a premier resource for mobility engineering professionals. It transcends boundaries and contributes to the advancement of the entire engineering community (SAE International, 2024).

Figure 1.1 Formula 1's redesigned car, by Nikolaos Tombazis, for the season 2022 due to FIA's new technical regulations.

[Available at: https://www.amazon.science/latest-news/the-science-behind-the-next-gen-2022-f1-car]

1.1.1 Formula SAE (FSAE)

FSAE, which stands for Formula Society of Automotive Engineers, represents one of the world's most prestigious and well-established academic motorsport competitions. Functioning under the auspices of the Society of Automotive Engineers (SAE).

The event's roots trace back to 1980 when it was initiated as FSAE, originating from the SAE student branch at the University of Texas at Austin. Over the years, the competition has experienced exponential growth, transforming into a highly regarded international platform. Presently, more than 500 universities from all corners of the world actively participate in this preeminent event, providing their students with invaluable practical engineering exposure.

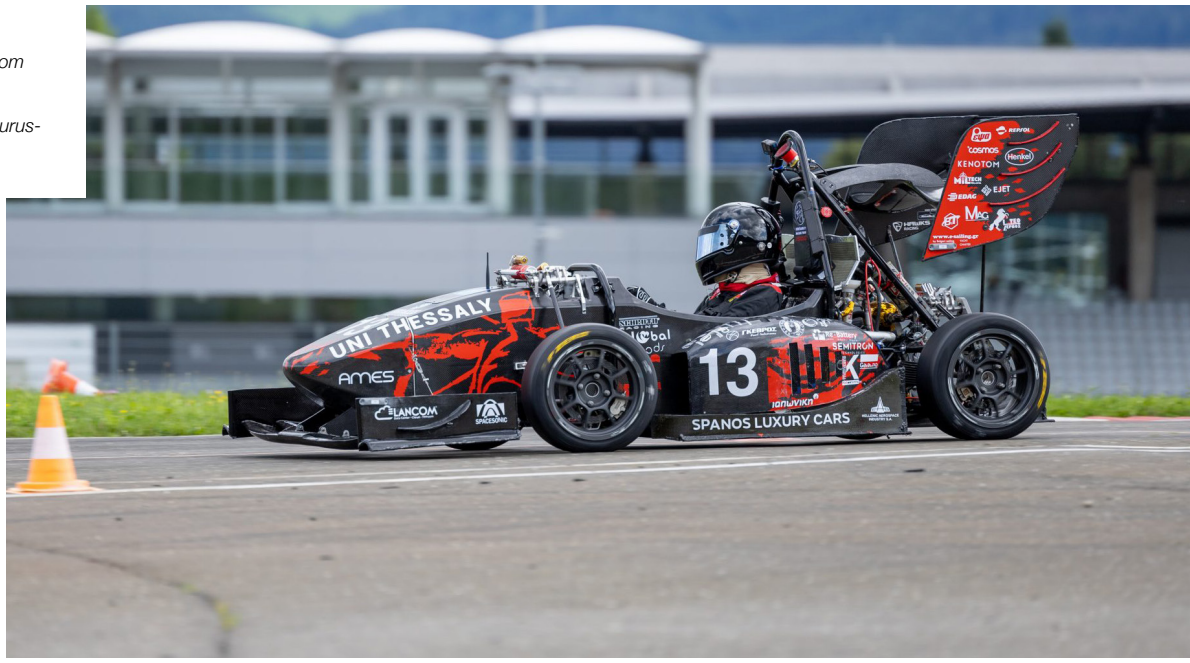

Figure 1.2 'Pyrius,' car by Centaurus Racing Team from Thessaly University.

[Available at: https://centaurus-racing.gr/pyrius/]

Through this competition process, undergraduate and postgraduate university students are invited to form a multidisciplinary team with members who possess different skill sets and expertise. Their objective is to conceive, design, fabricate, develop, and compete with a small-scale formula-style racing car meticulously crafted to conform to certain specifications, rules, and regulations set by SAE *(Figure 1.2).* In this realm of the Formula SAE series competitions, participating teams are afforded the opportunity to exhibit their creativity, practical engineering acumen, and collaborative spirit, nurturing innovation, fostering teamwork, and cultivating leadership qualities. From comprehensive research to construction, testing, development, marketing, management, and fundraising, the competition envelops all facets of car manufacturing. Embracing student teams

from all over the globe, this dynamic and competitive environment gives them the opportunity to put theory into practice through real-world racing scenarios.

In a meticulous evaluation process, the design of each student team is appraised and compared to other competing designs through a series of events, both on and off the track. The ultimate goal is to identify the vehicle that most effectively fulfills the competition's objectives. These vehicles are expected to exhibit high performance and the requisite durability to successfully navigate all events at Formula SAE competitions.

The competition comprises two distinct categories: static and dynamic events. Static events focus on evaluating the teams' design decisions, cost analysis, and business presentation skills. Dynamic events, on the other hand, put the car's performance to the test under race-like conditions. These events include the acceleration test, skid pad, autocross, endurance race, and assessment of efficiency.

In conclusion, Formula SAE has an indispensable role to fulfill in the education of engineers. It is not only a prestigious competition but also a transformative educational experience that equips students with the necessary tools to become future leaders in the automotive industry, capable of tackling complex problems. As an arena for innovation, collaboration, and technical prowess, FSAE continues to inspire and empower the next generation of automotive engineers, propelling the field of mobility engineering forward.

CHAPTER 2

AERODYNAMICS OF FORMULA 1 RACE CAR

2.1 Introduction to Formula 1 Aerodynamics

Aerodynamics, at its core, delves into the intricate interplay between air and objects in motion. In the context of Formula 1, it revolves around the art of manipulating airflow around the car. This mastery of aerodynamics wields immense influence over the vehicle's speed, thus emerging as a pivotal determinant of which car will be the fastest.

In addition to speed, the aerodynamic configuration of a Formula 1 car encompasses a variety of advantages. It can improve not only its acceleration and handling but also bolster stability, fuel efficiency, and sustainability as well. The ability to execute as swift and efficient turns, braking, and acceleration as possible is fundamental to success.

Conversely, lackluster aerodynamics can augment resistance against the car's forward motion, slowing it down and making it less responsive to driver inputs. In addition to the aforementioned elements, aerodynamics also plays a crucial role in ensuring driver safety. The forces generated by the car's aerodynamic design play a pivotal role in preserving the car's stability at high speeds and during turns and tight corners, thereby minimizing the risk of accidents. Moreover, it has a significant impact on the driver's visibility and overall comfort as well. Therefore, the prowess of aerodynamic design emerges as the defining factor between winning and losing a race.

2.2 Downforce, Lift, Lift Coefficient, Drag Force, and Drag Coefficient

Downforce, lift, lift coefficient, drag force, and drag coefficient represent the most vital elements in race car's aerodynamics.

The aerodynamic force that is applied perpendicular to the relative free-stream flow or "relative wind direction" over the surface of a car is called lift. There can be either positive (upward) or negative (downward) **lift,** *(Figure 2.2).* depending on the car's design, speed, and angle of attack (AoA) which is the angle between the body's reference line and the airflow. Aerodynamic lift is the same principle that allows an airplane to take off. However, in Formula 1 is not desirable and constitutes a great concern, particularly on high-speed circuits with long straights, where excessive lift is produced and can lead to the car becoming airborne or losing traction, resulting in a loss of control (*Figure 2.1).*

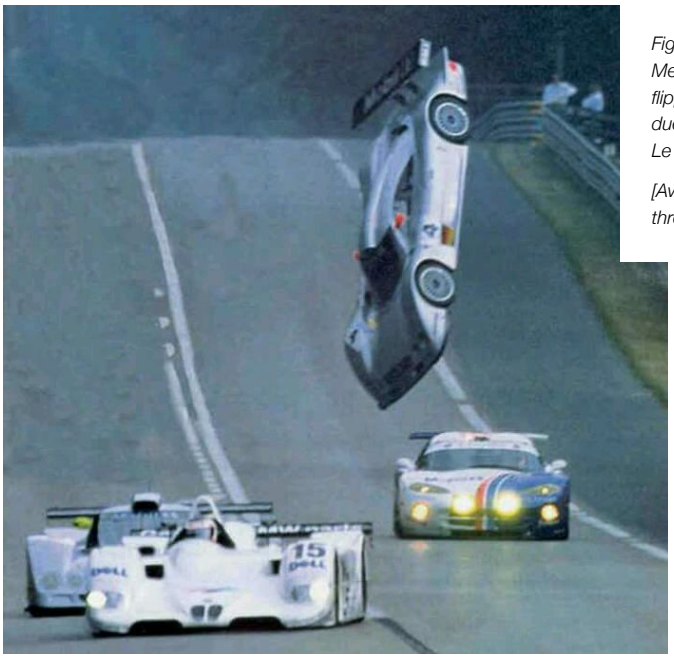

Figure 2.1 Mark Webber's Mercedes CLR accident, as it flipped and disintegrated mid-air due to aerodynamic instabilities, Le Mans 1999.

[Available at: https://www.car-throttle.com/post/wv6289m/]

Since we have lift, we also have the **coefficient of lift (C_L)**. In fluid dynamics, the lift coefficient (C_L) is a dimensionless coefficient that relates the lift generated by an object to the fluid density around the body, the fluid velocity, and an associated reference area. Thus, it measures the amount of lift generated by an object, factoring in its size, and shape, as well as the fluid density, velocity, and angle of attack (AoA). To put it simply, the lift coefficient quantifies the efficiency of an object in producing lift and can be influenced by the various factors mentioned earlier. A higher lift coefficient signifies greater lift generation under specific conditions, while a lower value indicates reduced lift. To counteract lift, Formula 1 aerodynamic engineers concentrate on generating downforce. Lift can be determined by the following equation: $L = \frac{1}{2} C_L \rho V^2 A$

where L is the lift force, A is the relevant plan area, ρ is the fluid density and V is the flow velocity (Oxyzoglou, 2017).

Downforce, in essence, is a negative lif *(Figure 2.2).* Specifically, it represents the vertical force applied to the car that increases the normal load on the tires without the equivalent increase in mass, helping it enhance traction and enabling faster performance on the track. In other words, it is the force that pushes the car down to the ground. As a consequence, the car's grip is improved, thus minimizing slippage and the risk of losing control, thereby enabling the car to navigate corners and

brake faster with superior stability and handling (*Figure 2.3)* (Oxyzoglou, 2017).

Undoubtedly, downforce is extremely desirable in race cars, and based on Bernoulli's law, it can be achieved by creating a difference in pressure between the upper and lower body of the car, and in particular when the pressure on the top surface of the car is higher than the bottom surface. In simpler terms, it is created when the velocity of the air above the car is not as fast as the velocity of the air moving below the car. Consequently, Bernoulli's principle states that there is an inverse relationship between the velocity of a fluid and the pressure it exerts. As the velocity of a fluid increases, the pressure it exerts decreases, and vice versa (Jalappa, 2015). Nevertheless, the existence of downforce also implies the presence of drag.

Drag represents another crucial facet of aerodynamics and, is the force that opposes the car's forward motion as it moves through the air *(Figure 2.2).* This force operates in parallel to the relative direction of the wind, exerting its impact on the vehicle's body**.** Drag is a primary factor that limits the car's top speed and acceleration. Note: the drag force and lift are proportional to each other.

Likewise, with lift, there is the **drag coefficient (C_D)** which is a non-vector value that quantifies the drag an object experiences as it moves through a fluid. Similar to the lift coefficient, it is affected by the shape, size, and surface of the object, as well as the fluid density, velocity, and angle of attack. The lower the value of the coefficient, the less drag the object experiences and the more aerodynamic it is. Consequently, during bodywork design, aerodynamic engineers strive to achieve the lowest possible C_D value. Drag can be determined by the following equation: $D = \frac{1}{2} C_D \rho V^2 A$

where D is the drag force, A is the relevant plan area, ρ is the fluid density and
V is the flow velocity (Oxyzoglou, 2017).

Achieving the right balance between downforce and drag can be challenging since, heightened downforce can lead to excessive levels of drag, while insufficient downforce can make the car un-

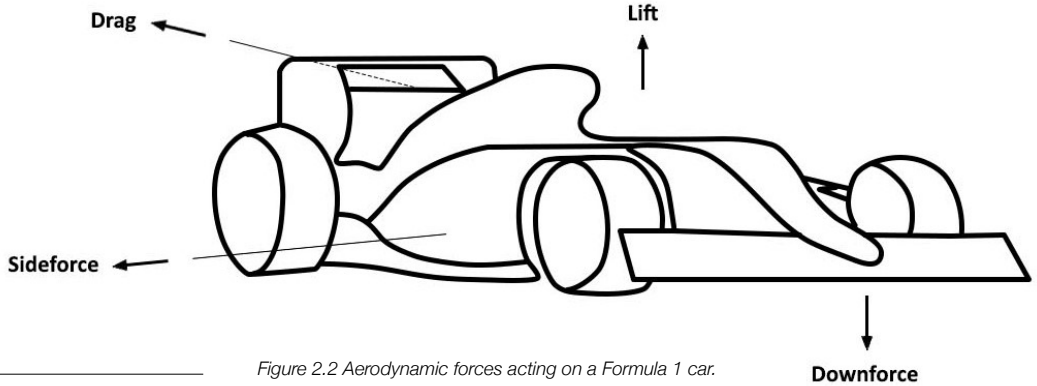

Figure 2.2 Aerodynamic forces acting on a Formula 1 car.

steady and easy to lose traction and control. Formula 1 teams devote substantial time and effort trying to harmonious balance these forces, which will lead them to best lap times. As David Tremayne (2006) aptly stated, the team that will be able to generate more downforce for less drag than any of their rivals will win.

Race designers and engineers need

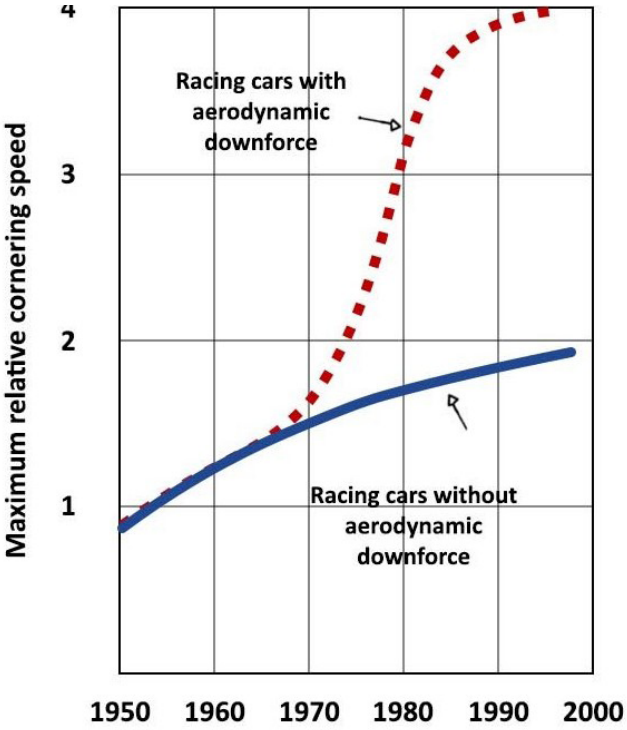

Figure 2.3 The increase of maximum cornering speed with aerodynamic downforce.

to comprehend and optimize these crucial aspects, as well as how air flows around, within, and through the body, its apertures, and its aerodynamic devices with the aim of building the most efficient cars possible, which are competitive on the track.

2.3 The Evolution of Aerodynamics in Formula 1

The pursuit of optimal airflow conditions for cars led aerodynamic engineers to embark on a journey of experimentation, eventually, after decades, introducing the concept of airfoils in the world of motor racing. More in particular, one of the pioneering teams in utilizing aerodynamic wings was Colin Chapman's Lotus team, who brought the concept to Formula 1 with the Lotus 49B at the 1968 Monaco Grand Prix, *(Figure 2.4),* 18 years after the first official Formula 1 race which took place in 1950. Lotus already had incorporated a simple aerodynamic device at the rear, but in Monaco, the first wings appeared. Subsequently, at the following race in Belgium, Braham and Ferrari teams took it a step further by adding distinct rear wings. Since then, wings have come in all sorts of heights, shapes, and sizes as experimentation and computer modeling have developed wing complexity further and faster, leading to the modern Formula 1 we recognize today.

The use of inverted aircraft wings on Formula 1 cars, with the purpose of generating downforce, rather than lift, was a breakthrough moment that gave birth to Formula 1's first ground effect aerodynamics. This technology aims to suction the car towards the track from below, and Lotus, known for their innovation in Formula 1 and having pioneered aerodynamics with their winged cars a decade earlier, debuted the first ground effect aerodynamics with the Lotus 78 at the opening round of the 1977 season in Argentina. The Lotus 78 featured sidepod skirts - bodywork extensions that dropped from the car's edges to the track surface *(Figure 2.5).* When these skirts were lowered, the resulting lower air pressure created underneath the car gave them huge amounts of

Figure 2.4 Lotus 49B driven by Graham Hill at the 1968 Monaco Grand Prix.

[Available at: https://primotipo.com/2015/07/12/wings-clipped-lotus-49-monaco-grand-prix-1969/]

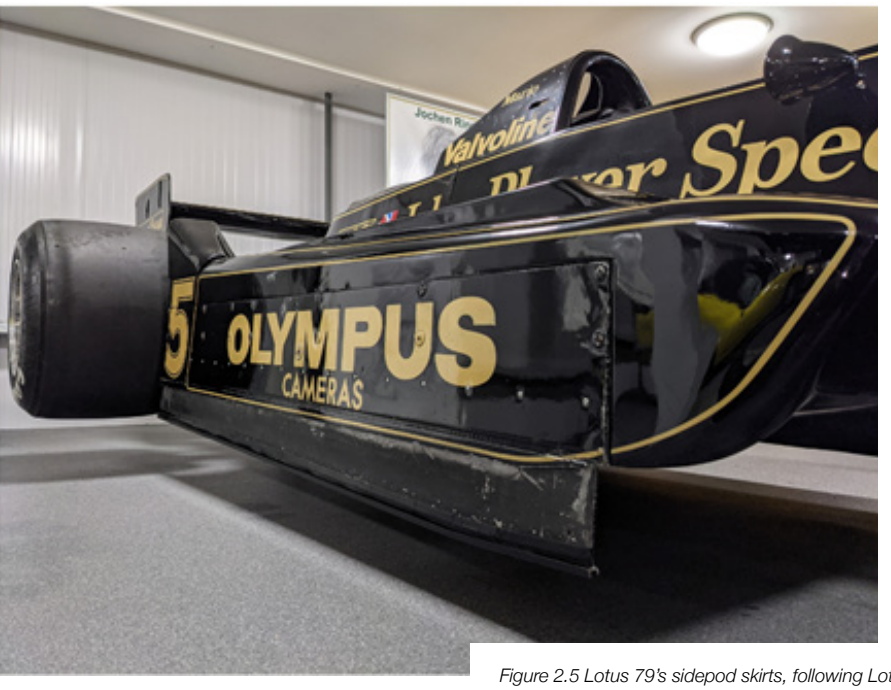

Figure 2.5 Lotus 79's sidepod skirts, following Lotus 78 that ushered in the 'ground-effect' era.

[Available at: https://classicteamlotus.co.uk/en/news/posts/2021/secrets-of-the-lotus-79-skirts/]

downforce without the accompanying drag that comes with wings.

The groundbreaking ground effect aerodynamics introduced by the Lotus 78 enabled it to generate levels of downforce three times greater than those of the other cars on the grid. The absence of such innovations in the other cars left them unable to match the significant downforce achieved by the Lotus Team. This breakthrough technology revolutionized Formula 1 aerodynamics, providing the Lotus team with a competitive edge during that era.

However, this was discovered rather than designed. When the team attached a car to keep an experimental sidepod design in place in the wind tunnel, the unexpected amounts of downforce pitched their developments down to a completely new car. The other teams quickly took notice, and the skirts were widely copied, ushering in the ground effect era. Although sidepod skirts are no longer used in Formula 1, the importance of floor aerodynamics remains crucial to this day, a legacy from that chance discovery in the Lotus wind tunnel 40 years ago.

Over time, additional aerodynamic devices such as front wings, diffusers, bargeboards, flip-ups, brake ducts, and more have been increasingly fitted to the car's body. The aerodynamic interaction between these various body components is significant, with every curve and contour designed to control the airflow of the car and create a low-pressure area underneath it, hence downforce (Formula 1, 2019).

2.4 Wing Theory and Geometrical Characteristics

An airfoil, also known as a wing profile, is a fundamental element of wings *(Figure 2.6).*

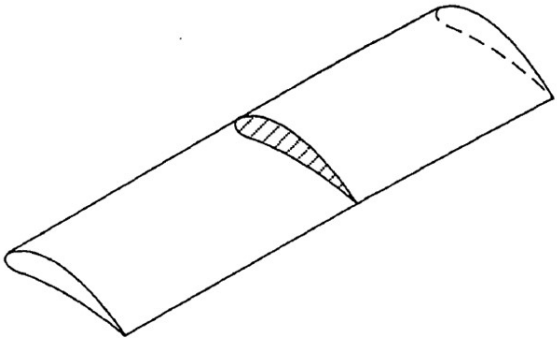

Figure 2.6 The airfoil is the shaded shape shown on the wing (Katz, 1995).

Its shape is designed to generate lift as air passes over it. The meticulous design of an airfoil focuses on creating a pressure difference between its upper and lower surfaces, resulting in the production of lift *(Figure 2.7).* The shape of the airfoil causes the air above the wing to flow faster than the air below it. This phenomenon aligns with Bernoulli's principle, which states that faster-moving air

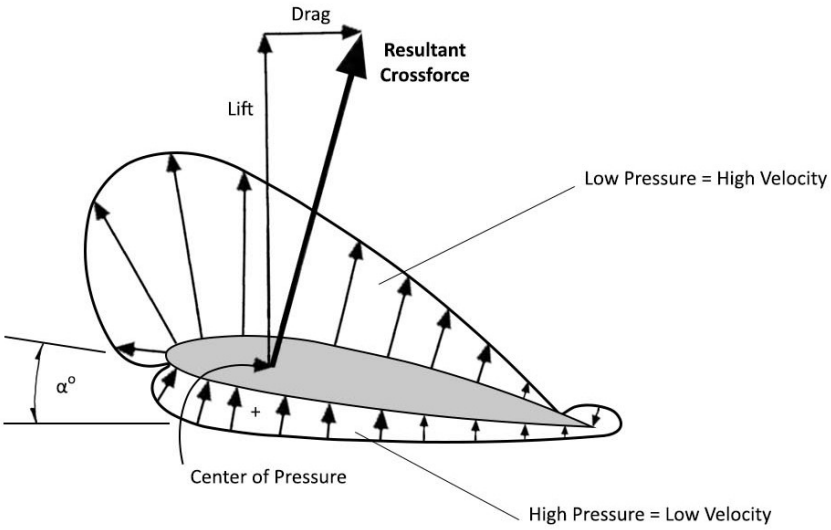

Figure 2.7 How a moving airfoil produces lift due to pressure differential.

has lower air pressure while slower-moving air has higher air pressure. Thus high air pressure underneath the wing pushes the aircraft upwards (lift), and correspondingly inverted wings push the car downwards (downforce). The upper and lower surfaces of the airfoil are also known as suction and pressure surfaces, respectively. Therefore, any shape that creates a pressure difference when exposed to airflow is considered an airfoil.

Furthermore, according to Newton's third law, "Action and Reaction," which states that for every action - force - in nature, there is an equal and opposite reaction, we can conclude that if the airfoil

exerts a downward force on the air, the air will reciprocate by exerting an opposing force of equal magnitude in an upward direction onto the airfoil (Oxyzoglou, 2017).

In Formula 1, the airfoils utilized for the front and the rear wing by the teams vary from one another. Nevertheless, all airfoils share certain common geometric characteristics which will be analyzed in this chapter.

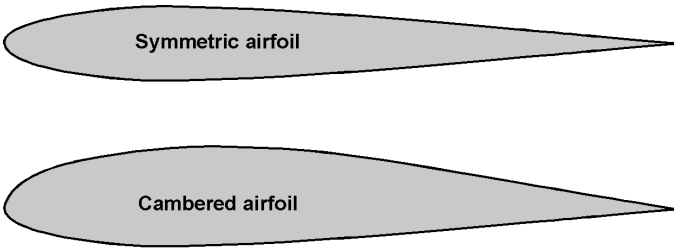

Figure 2.8 The shape types of an airfoil.

[Available at: https://eaglepubs.erau.edu/introductiontoaerospaceflightvehicles/chapter/airfoil-geometries/]

2.4.1 Shape of an Airfoil

As illustrated in the figure below *(Figure 2.8),* airfoils can come in two shapes: symmetric and cambered. Symmetric airfoils have the same shape and curvature on both the upper and lower surfaces, while cambered airfoils have differing curvature on the upper and lower surfaces.

2.4.2 Geometry of an Airfoil

The inherent structure of an airfoil is established by its profile configuration, which governs the curvature exhibited by its upper and lower surfaces. Illustrated in the accompanying figure *(Figure 2.9)* are the essential geometric factors that precisely characterize the form and composition of an airfoil.

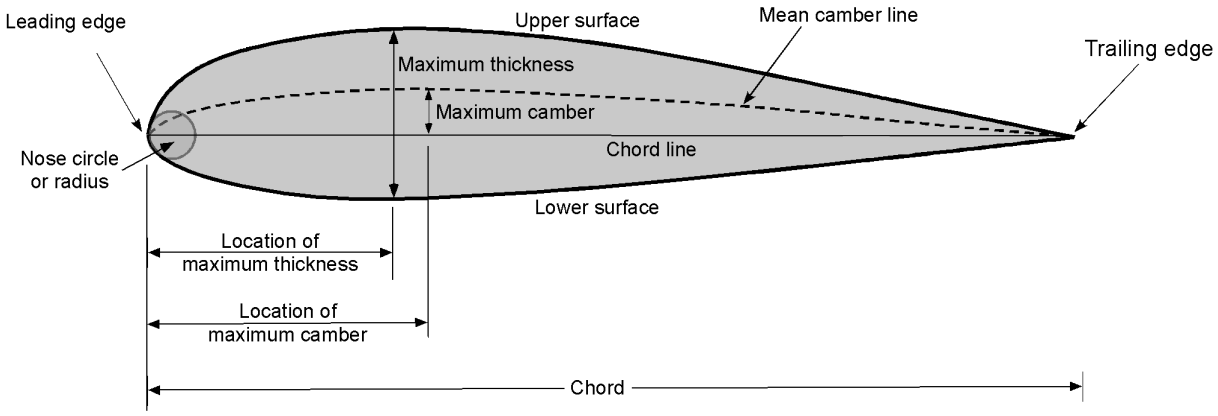

Figure 2.9 The key geometric parameters that define the shape of an airfoil.

[Available at: https://eaglepubs.erau.edu/introductio toaerospaceflightvehicles/chapter/airfoil-geometries/]

More specifically,

Leading Edge

Positioned at the forefront of the airfoil, the leading edge represents the foremost location characterized by the highest degree of curvature and the smallest radius. It signifies one of the two defining extremities, the forward extremity, forming the overall contour of the airfoil (Oxyzoglou, 2017).

Typically, the leading edge of an airfoil exhibits a circular shape, characterized by a leading-edge radius approximately equal to 0.02 times the chord length (0.02c).

Trailing Edge

Located at the terminal point of the airfoil, the trailing edge marks the conclusion of its structure, serving as the second extremity, the rearward extremity that defines the airfoil's shape. While possessing its own radius of curvature, the trailing edge exhibits a notably smaller magnitude compared to that of the leading edge.

Chord Line

The chord line, an essential element of the airfoil, refers to a line that traverses through the centers of maximum curvature found at both the leading and trailing edges. It can be described as a straight line that seamlessly connects the extremities of these edges. This line intersects the airfoil section at each endpoint. Denoted by c, the length of the chord line is commonly referred to as the airfoil chord.

Note: To establish a reference point, the intersection of the chord line with the front of the section is selected as the origin for a set of axes. The x-axis is aligned with the chord line, while the y-axis runs perpendicular to the chord line, with positive values denoting the upward direction (Houghton & Carpenter, 2003).

Camber Line

Within the span of the chord, it is possible to designate a midpoint between the upper and lower surfaces. This midpoint serves as a reference point along the section and forms a curved locus when connected with other corresponding midpoints. This curve, commonly known as the **mean camber line**, represents the average contour of the section.

The maximum vertical distance between the mean camber line and the chord line, known as the ***maximum camber*** and denoted by **δ**, quantifies the peak separation between these two lines. Typically is expressed as a percentage or fraction of the chord. The quantity is called the ***percentage camber*** of the section.

Airfoil sections generally exhibit cambers that fall within a range of 0 (symmetrical section) to 5%. In symmetrical airfoils, the chord line coincides with the mean camber line, indicating equal camber on both the upper and lower surfaces. On the other hand, non-symmetrical airfoils feature distinct camber variations between their upper and lower surfaces (Houghton & Carpenter, 2003).

Angle of Attack (AoA)

The angle of attack specifies the acute angle formed between the chord line of the airfoil and the direction of the relative airflow.

When symmetrical airfoils are subjected to a zero angle of attack, they produce zero lift.

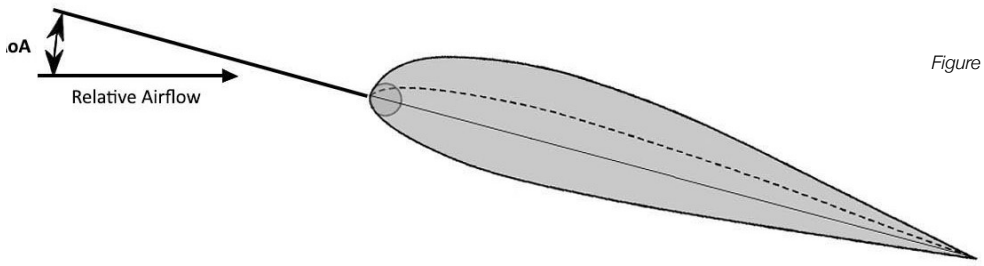

Figure 2.10 Angle of attack defined.

Aerodynamic Center

The aerodynamic center corresponds to a specific chord-wise position along the airfoil, where the pitching moment -the tendency of a cambered airfoil to rotate its nose downwards when generating lift- remains unaffected by changes in the lift coefficient and AoA.

Center of Pressure (C_p)

The center of pressure is the precise location on the airfoil where the resultant pressure exerts its force *(Figure 2.7).* It is also the chord-wise location about which the pitching moment is zero.

In the case of symmetrical airfoils, the movement of the center of pressure remains relatively consistent when the angle of attack varies.

Determining the center of pressure on an airfoil is crucial as it affects the airfoil's stability and con-

trol characteristics, being the primary cause of undesired rotation during movement. However, determining the center of pressure is challenging because the pressure at each point of the airfoil changes with each adjustment in the angle of attack, causing the center of pressure to shift (Fareeq, 2015).

Maximum Thickness

Once the camber line has been determined, the distances from this line to both the upper and lower surfaces can be measured. Notably, these distances are consistently equal. Measurements can be taken at various points along the chord and plotted against the corresponding x-values, resulting in a symmetrical shape known as the **thickness distribution** or symmetrical fairing.

A significant parameter of the thickness distribution is the **maximum thickness** or depth, denoted by **t.** The maximum thickness of an airfoil represents the greatest separation between its upper and lower edges. When expressed as a fraction of the chord, it is referred to as the thickness-to-chord ratio, and calculated as a percentage: $\frac{100t}{c}\%$ .Additionally, the location along the chord where the maximum thickness occurs serves as another important parameter. Typically, the values for this parameter range between 30% and 60% of the chord length, measured from the leading edge (Leloudas, 2015; Oxyzoglou, 2017; Houghton & Carpenter, 2003).

2.4.3 Parameters Affecting the Performance of an Airfoil

To achieve precise geometric construction of airfoil profiles, it is necessary to be meticulous about how exactly the airfoil shape is defined. This entails determining the value and position of the maximum thickness (thickness to chord ratio), the value and position of the maximum camber, as well as the nose radius. By paying close attention to these factors, an accurate representation of the airfoil's geometry can be attained.

Airfoils exhibit unique flight characteristics based on their design. Efficiency is determined by the lift to drag ratio or the coefficient of lift (C_L), where higher values indicate greater efficiency.

The coefficient of lift varies with the angle of attack and is also influenced by the airfoil's thickness and camber. The interplay of these factors shapes its overall performance.

2.4.3.1 Critical Angle of Attack

The angle at which the air hits the airfoil is a decisive factor for the lift generated, thus representing a fundamental aspect of the performance of the airfoil. The increase in angle up to a certain point is proportional to the increase in lift. After this point, the airfoil may experience a breakdown in lift circulation, known as a ***stall***. The respective angle of attack is referred to as the ***stall angle of attack***. Below this critical angle of attack, and as the angle tends to reach it, the lift coefficient C_L exhibits an upward trend. Conversely, when the angle of attack exceeds the critical angle, the airflow over the airfoil's upper surface becomes less streamlined and begins to flow less smoothly, causing it to separate transiently. At the critical angle of attack, the airfoil produces maximum lift and the separation of airflow is more separated on the upper surface. As the angle increases further, the flow becomes more and more separated, resulting in the airfoil producing less and less lift *(Figure 2.11).* Consequently, the lift coefficient C_L diminishes, while the drag coefficient C_D experiences a rapid increase. For many standard airfoils, this critical angle of attack typically falls within the range of 12° to 20°. It signifies a crucial threshold that affects the performance characteristics of the airfoil, highlighting the importance of understanding and managing the airflow conditions within this operating regime.

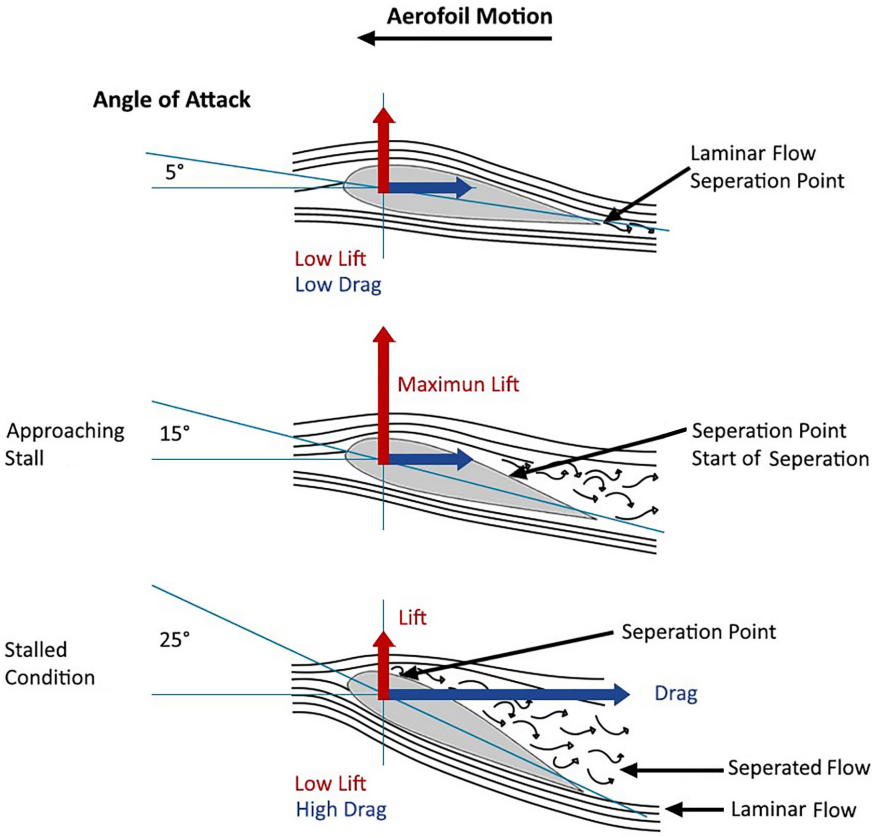

Figure 2.11 Behavior of airflow around an airfoil at rising angles of attack.

More specifically, the coefficient of lift C_L varies linearly with the angle of attack (α) at low to moderate angles, as depicted in the accompanying diagram, Figure 2.12. The slope of this straight line is called the **lift slope** and is denoted by $\boldsymbol{a_0}$**.**

In this area, the airflow exhibits a coherent and undisturbed movement over the airfoil, remaining attached to most of the surface, as visually demonstrated in the left side of Figure 2.12. However, as the angle of attack (α) increases, the airflow gradually disengages from the upper surface of the airfoil, resulting in the formation of a notable wake of stagnant air, commonly referred to as "dead air", trailing behind the airfoil. This phenomenon is visually depicted on the right side of Figure 2.12.

Within this separated region, the airflow undergoes recirculation, with a portion of the flow moving in the opposite direction of the free stream, also known as reverse flow. Viscous effects are responsible for the occurrence of this separated flow, and at high angles of attack (α), it results in a notable reduction in lift and a substantial increase in drag. Such conditions are indicative of the airfoil being in a stalled state. Note: The separation of the flow by angle of attack is also shown in Figure 2.11).

The maximum value of lift coefficient, denoted by $C_{L,max}$, is attained just prior to the stall. A higher $C_{L,max}$ corresponds to a lower stalling speed. As illustrated in Figure 2.12, the lift coefficient C_L exhibits a linear increase with the angle of attack (α) until the point where flow separation begins to take effect. At this point, the curve becomes nonlinear, C_L reaches a maximum value, and consequently the airfoil enters the stall condition.

The lift on an airfoil reaches zero only when it is inclined to a negative angle of attack. The angle of attack at which lift equals zero is called the **zero lift angle of attack** and is denoted by $\boldsymbol{\alpha_{L=0}}$. In the case of a symmetric airfoil, $\alpha_{L=0} = 0$, whereas for all airfoils with positive camber (camber above the chord line), $\boldsymbol{\alpha_{L=0}}$ is typically a negative value, usually around –2° or –3°.

It is important to note that the lift slope, denoted as a_0, remains unaffected by the Reynolds number (Re). Conversely, the maximum lift coefficient $C_{L,max}$ is influenced by the Reynolds number (Re).

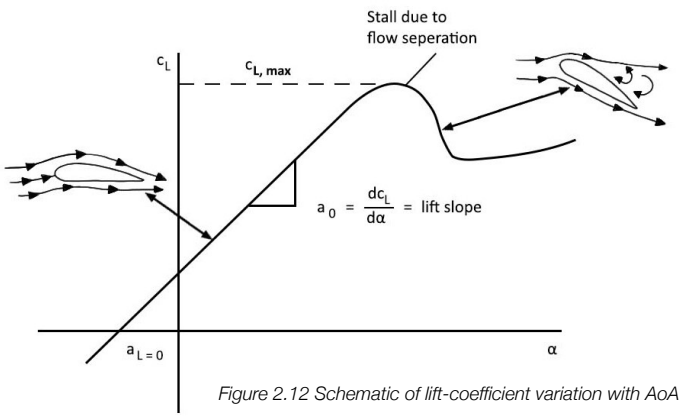

Figure 2.12 Schematic of lift-coefficient variation with AoA for an airfoil (Anderson, 2017).

A primary objective for engineers during airfoil design is to achieve a stall characteristic that allows for an expanded performance range at the maximum lift coefficient $C_{L,max}$. Thus, a high lift airfoil is crucial to attain a soft stall behavior that ensures the maintenance of $C_{L,max}$ or close proximity to it across a wide range of angles of attack. This characteristic provides flexibility in tuning the airfoil's performance to meet varying requirements (Oxyzoglou, 2017; Anderson, 2017).

2.4.3.2 Camber

The integration of camber into airfoil configurations facilitates the creation of lift even at relatively low angles of attack. Incorporating a camber into an airfoil generally amplifies the lift coefficient across its complete spectrum of angles of attack, encompassing the maximum value. Precisely, this inclusion shifts the "zero lift angle of attack" of the airfoil to a negative magnitude, resulting in the production of positive lift at small negative angles as well. Moreover, the lift coefficient experiences augmentation as the camber ratios and angles of attack increase.

Symmetric airfoils, or airfoils without camber, produce zero lift at zero angle of attack ($\alpha=0$). Conversely, airfoils with positive camber, characterized by greater curvature on their upper surfaces, tend to produce more lift even at slight negative angles, as previously discussed. Obviously, negatively curved airfoils tend to produce less lift compared to positively curved airfoils. This discrepancy arises from the pressure differential created by the curved shape between the upper and lower surfaces, contributing to lift generation. Higher camber ratios result in elevated lift coefficients, particularly at higher angles of attack (Roy et al., 2021). Generally, greater camber in an airfoil profile correlates with increased lift coefficients as well as drag coefficients.

The key parameters of camber that significantly impact airfoil performance are the value and location of the maximum camber.

The value primarily affects the maximum lift coefficient as well as the drag production, whereas the position of the maximum camber influences the distribution of lift along the airfoil opening and the behavior at different angles of attack.

Augmenting the maximum camber value typically results in an increase in the airfoil's maximum lift coefficient. However, higher camber airfoils tend to exhibit greater drag due to the amplified pressure differential between their upper and lower surfaces. This is attributed to the larger surface area resulting from increased curvature, which in turn leads to heightened frictional drag. Consequent-

ly, selecting the appropriate maximum camber value depends on the desired balance between lift and drag for a specific application. While higher maximum camber provides enhanced lift, it comes at the expense of increased resistance. Thus, highly cambered airfoils are recommended for achieving high lift, whereas less cambered airfoils are preferred for minimizing drag (Gupta and Saxena, 2017).

Knowing the location of the maximum camber is crucial as it directly influences the camber distribution along the airfoil, which in turn affects the pitching moment. The pitching moment refers to the tendency of a cambered airfoil to rotate its nose downwards when generating lift, as previously explained. The magnitude of the pitching moment depends on the camber distribution.

When the maximum camber of an airfoil is positioned closer to the leading edge, it concentrates the lift distribution towards the front, resulting in a higher pitching moment. This configuration can enhance stability but may also contribute to increased drag. Conversely, airfoils with the maximum camber located towards the trailing edge exhibit a lift distribution that is more rearward, leading to a reduced pitching moment and the potential for decreased drag.

Typically, as the location of the maximum camber is shifted either forward or backward from the approximate mid-chord position, there is a general increase in the maximum lift coefficient.

Furthermore, the positioning of the maximum camber has an impact on the aerodynamic characteristics of the airfoil at different angles of attack. Airfoils with the maximum camber situated closer to the leading edge tend to exhibit a more pronounced stalling behavior, characterized by an abrupt loss of lift at the stall angle of attack. In contrast, airfoils with the maximum camber positioned closer to the trailing edge demonstrate a more gradual stalling behavior, facilitating a smoother transition and improved controllability at higher angles of attack.

Hence, the choice of the location of the maximum camber is dependent on the desired lift distribution, stalling behavior, and overall aerodynamic performance required, in our case, particularly tailored to each Formula 1 track

Both the value and location of the maximum camber interact with various other parameters of the airfoil, such as angle of attack and thickness, which will be explored in greater detail in the subsequent section (Roy et al., 2021).

2.4.3.3 Thickness

The thickness of the airfoil is another decisive factor in the profile of an airfoil. Likewise, both the value and position of the maximum thickness significantly impact the lift, drag and overall aerodynamic characteristics of the airfoil. Additionally, the distribution of thickness along the chord of the airfoil holds equal importance in shaping its behavior.

Expanding the thickness of the airfoil provides greater space for airflow, enabling the generation of lift and leading to elevated maximum lift coefficients. Thicker airfoils inherently exhibit increased camber, which contributes to a larger pressure differential between the upper and lower surfaces, thereby enhancing lift production. Furthermore, an increase in thickness $\left(\frac{t}{c}\right)$ slightly amplifies the slope of the airfoil's lift curve (Gupta and Saxena, 2017). Generally, thicker airfoils possess a larger surface area that interacts with the airflow, enabling them to generate more lift.

Nevertheless, it is important to note that thicker airfoils also tend to generate higher levels of drag and elevated drag coefficients due to their increased surface area and pressure drag, which can adversely affect overall performance. The larger surface area of thicker airfoils leads to heightened frictional drag along the airfoil's surface. Moreover, thicker airfoils may experience more pronounced separation of the boundary layer, further contributing to increased drag.

Note: The subsequent section will provide a detailed explanation, offering a comprehensive understanding of the role and implications of boundary layers.

Similar to the decision-making process for the maximum camber value, selecting the optimal maximum thickness value involves striking a balance between lift and drag requirements. Opting for a higher maximum thickness yields greater lift, albeit at the expense of increased drag. Conversely, reducing the maximum thickness reduces lift while potentially reducing resistance.

Regarding the angle of attack, thicker airfoils demonstrate improved performance at higher angles of attack due to their ability to generate a higher lift-to-drag ratio and consequently higher lift coefficients. Therefore, it is advisable to employ thinner airfoils at lower angles of attack and opt for thicker airfoils when encountering higher angles of attack (Roy et al., 2021).

The position of the maximum thickness plays a role in determining the lift distribution across the span of the airfoil. Airfoils with the maximum thickness positioned closer to the leading edge tend to exhibit a lift distribution that is more concentrated towards the front, leading to an increased pitching moment. While this configuration enhances stability, it may also contribute to higher drag.

Conversely, airfoils with the maximum thickness located towards the trailing edge display a lift distribution that is more rearward-focused, resulting in a reduced lift moment and potentially decreased drag (Roy et al., 2021).

Furthermore, the positioning of the maximum thickness has a notable impact on the aerodynamic behavior of the airfoil. It influences how the airfoil responds to variations in the angle of attack. Airfoils with the maximum thickness positioned closer to the leading edge tend to display a more abrupt stall behavior, which is characterized by a sudden loss of lift at the stall angle of attack. In contrast, airfoils with the maximum thickness located further towards the trailing edge demonstrate a more gradual stalling behavior. This smoother transition allows for improved controllability and better handling at high angles of attack (Roy et al., 2021).

Therefore, the choice of the location of the maximum thickness is determined by the desired stability, control, and performance characteristics of the airfoil under specific operating conditions, thus the unique demands of each track. This decision involves a careful balance between lift distribution, stall behavior, and overall aerodynamic performance.

Finally, the thickness distribution of an airfoil along its chord length directly impacts its lift and drag characteristics. Airfoils with a concentration of thickness towards the leading edge typically exhibit higher maximum lift coefficients, albeit at the expense of increased drag. Conversely, airfoils with more evenly distributed thickness along the chord length tend to achieve lower maximum lift coefficients and reduced drag (Roy et al., 2021).

As mentioned earlier, it is worth noting that the thickness of an airfoil interacts with other crucial parameters such as camber and angle of attack to collectively determine its overall aerodynamic behavior.

2.5 Boundary Layers

For a better comprehension of this chapter, it is essential to note the difference between viscous and inviscid flow. All real flows fall under the umbrella of viscous flows, where the influence of friction, thermal conduction, and diffusion is present. In contrast, inviscid flow represents an idealized state devoid of these influences. While true inviscid flows do not exist in nature, numerous practical aerodynamic scenarios exhibit minimal influence from transport phenomena, enabling the modeling of flows as inviscid. For such flows, the impact of friction, thermal conduction, and diffusion is confined to the boundary layer (Anderson, 2017).

In the distant area of the flow field, the velocity gradients remain relatively small, and friction assumes a negligible role. However, as we approach the thin region within the flow near the surface, velocity gradients become significant, and friction emerges as a defining factor. Ludwig Prandtl, a renowned German fluid dynamicist, initially recognized this intrinsic duality in 1904, concerning how the significance of friction varies dramatically between two distinct regions.

After Prandtl's pioneering revelation, theoretical analyses of aerodynamic flows have generally followed a two-fold approach. The area far from the body is viewed as an inviscid flow, where dissipative effects attributed to friction, thermal conduction, or mass diffusion are ignored. On the other hand, in contrast to this region, the thin layer proximate to the body surface is considered viscous, and characterized by these dissipative effects during analysis *(Figure 2.13)* (Anderson, 2017).

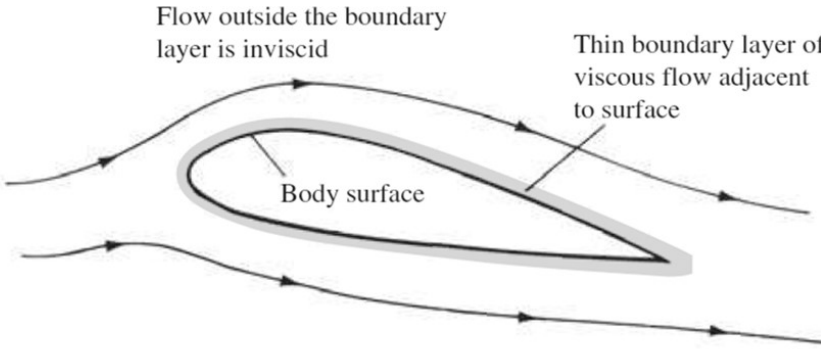

Figure 2.13
The classification of a flow into two distinct regions: (1) the thin viscous boundary layer adjoining the body surface, and (2) the inviscid flow extending beyond the boundary layer (Anderson, 2017)..

In fluid dynamics, this thin viscous layer of air that extends across and is adjacent to the surface of the airfoil is called the boundary layer. It stands as a pivotal element when examining the complex interaction between air and surfaces exposed to airflow, such as airfoils.

Though diminutive compared to the overall flow, this thin region has a substantial influence. In most aerodynamic studies, the slender nature of the boundary layer contrasts with its profound impact. It is responsible for the generation of friction drag on aerodynamic bodies, making it crucial for understanding and optimizing aerodynamic performance.

Note: Flow separation phenomena, mentioned in subsection 2.4.3.1 "Critical Angle of Attack", are closely related to the presence of the boundary layer (Anderson, 2017).

We shall delve into the factors contributing to the significant velocity gradients observed within the boundary layer.

To commence the discussion, let us examine the inviscid flow characteristics over the airfoil profile illustrated in Figure 2.14. In this idealized scenario, friction effects are absent by definition, leading

to the slip of the streamline over the body's surface. At a specific point, denoted as 'b' on the surface, the flow velocity attains a finite value unaffected by frictional influences. However, in reality, the infinitesimally thin layer of air molecules directly adjacent to the body surface adheres to it due to the presence of friction, resulting in a relative zero velocity with respect to the surface. This phenomenon, recognized as the no-slip condition, is responsible for the emergence of substantial velocity gradients within the boundary layer (Anderson, 2017).

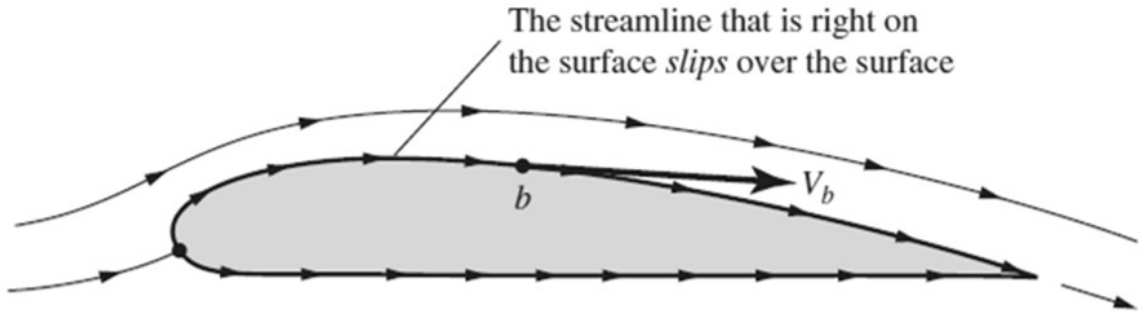

Figure 2.14 Inviscid flow (Anderson, 2017).

Directly above this adhered layer, the adjacent layer of air molecules is set in motion, propelled by a third layer situated close to the free stream of air.

Note: The kinetic theory of gases acknowledges a slip velocity proportional to the velocity gradient (Abbott and Doenhoff, 1959), indicating that the velocity at the surface is not precisely zero.

We will now embark on a deeper exploration of this subject. Consider the flow displayed in Figure 2.15. The boundary layer is significantly magnified in thickness for clarity. At point 'a' on the body surface, the flow velocity is zero, adhering to the no-slip condition. Moving above point 'a', the velocity progressively increases until it reaches the value of V_b at point 'b', located at the outer edge of the boundary layer. Given the thinness of the boundary layer, it is assumed that V_b at point 'b' in Figure 2.15 is equivalent to V_b at point 'b' on the body in the inviscid flow as depicted in Figure 2.14. The conventional analysis of the boundary layer posits that the flow conditions at the outer perimeter of this layer mirror the surface flow conditions observed in an inviscid flow analysis.

Upon closer inspection of Figure 2.15, the flow velocity within the boundary layer undergoes an increase from zero at point 'a' to a substantial finite velocity at point 'b.' This rapid increase occurs over a very short distance due to the thinness of the boundary layer, resulting in large velocity gradients, i.e., significant local values of $\frac{\mathbf{dV}}{\mathbf{dy}}$. Consequently, the boundary layer emerges as an area of

the flow where frictional forces have greater influence.

Figure 2.15 also displays the shear stress at the wall, denoted as τ_w, and the boundary layer thickness, represented by δ. These two parameters hold significant importance in determining boundary layer theory, with a vast portion of it dedicated to their computation.

Both experimentally and theoretically, it can be demonstrated that the pressure across the bound-

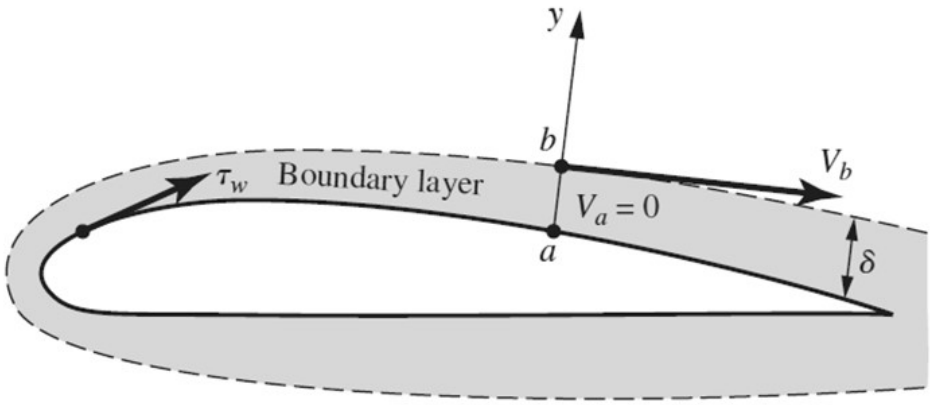

Figure 2.15 Boundary layer in magnification (Anderson, 2017)

ary layer in a direction perpendicular to the surface remains constant. Referring to Figure 2.15, where the y-axis is perpendicular to the body at point 'a', consider p_a and p_b as the pressures at points a and b respectively; p_a indeed equals p_b, p_a=p_b.

The accurate representation of actual surface pressures is achieved through the calculation of the inviscid flow's surface pressure distribution (as depicted in Figure 2.14). This outcome can be attributed to the fact that correct outer-edge pressure at the thin boundary layer (point b as illustrated in Figure 2.15) is made available by inviscid calculations, and these pressures remain unaltered as they are transmitted through the boundary layer all the way down to the surface at point 'a'.

The aforementioned statements hold true for thin boundary layers that remain connected with the body surface. However, they do not apply to areas where flow is detached.

Upon closer examination of the boundary layer, Figure 2.16 displays the velocity profile within it. The velocity initiates at zero on the surface and gradually escalates to V_b at its outer extremity (Anderson, 2017).

Stated differently, the velocities of the air layers increase progressively as they move away from the surface, until they reach the free stream velocity. It is crucial to note that all these velocities are subject to the influence of the free stream.

Establishing coordinate axes x and y involves aligning x parallel to the surface and y perpendicular

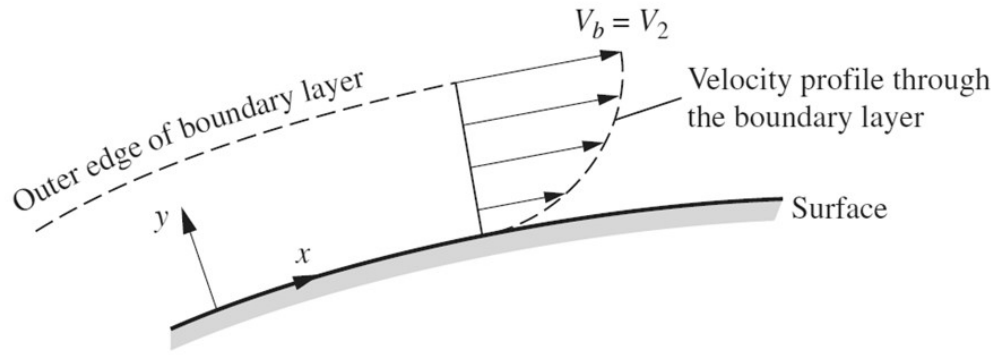

Figure 2.16 Velocity profile through a boundary layer (Anderson, 2017).

to the surface, as illustrated in Figure 2.16. By definition, a velocity profile gives the variation of velocity in the boundary layer as a function of y. Generally, the velocity profiles at various x-stations are different.

The inclination of the velocity profile at the wall holds significant importance as it dictates the shear stress experienced by the wall. To explain this, let $\left(\frac{dV}{dy}\right)_{y=0}$ denote the velocity gradient at the wall. Consequently, the shear stress at the wall is expressed as $\tau_w = \left(\frac{dV}{dy}\right)_{y=0}$ (Equation 1), where μ represents the absolute viscosity coefficient, also known as the viscosity, of the gas.

The viscosity coefficient, μ, is an inherent physical property of the fluid, and it differs for various gases and liquids. Additionally, μ undergoes changes with temperature (T). In the case of liquids, μ decreases with an increase in temperature, while for gases, μ tends to increase with rising temperatures.

Until this juncture in our discourse, we have regarded flow streamlines as being sleek and regular curves within space. Nevertheless, the reality of viscous flows, especially within boundary layers, is more intricate. Viscous flow manifests in two primary forms: laminar flow and turbulent flow.

Laminar flow, is characterized by smooth and regular streamlines, where fluid elements move seamlessly along their paths without inducing eddying motion. On the contrary, turbulent flow is characterized by the breakdown of streamlines, leading fluid elements to follow in a random, irregular, and convoluted path, distinguished by the presence of numerous small eddies.

The disparities between laminar and turbulent flow are profound, exerting a significant influence on aerodynamic processing. (Anderson, 2017).

Examining the velocity profiles within a boundary layer, as illustrated in Figure 2.17, reveals distinctions based on whether the flow is laminar or turbulent. Compared to the laminar profile, the turbulent version appears larger and fuller in appearance. In the turbulent profile, the velocity remains relatively close to the freestream velocity from the outer edge to a point near the surface, after which it rapidly drops to zero at the surface. Conversely, for the laminar velocity profile, there is a gradual diminish to zero from the outer edge to the surface.

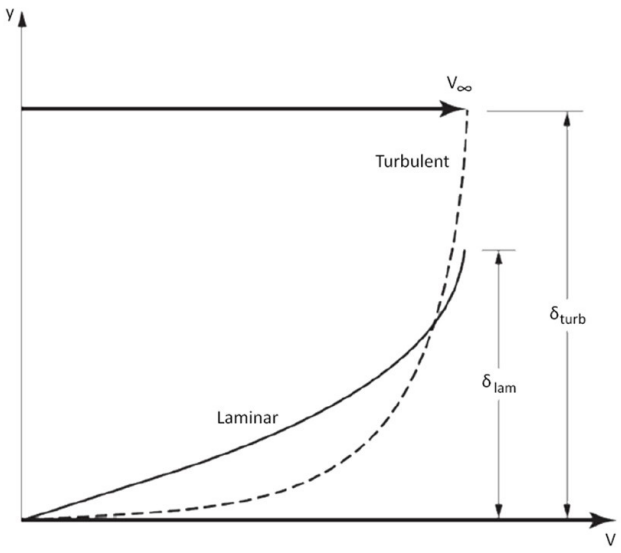

Figure 2.17 Depiction of velocity profiles in both laminar and turbulent boundary layers. Note that the turbulent boundary layer has a greater thickness compared to the laminar boundary layer (Anderson, 2017)

As previously mentioned, the velocity gradient at the wall is denoted as $\left(\frac{dV}{dy}\right)_{y=0}$.It is worth noting that for laminar flow, the value of $\left(\frac{dV}{dy}\right)_{y=0}$ is generally smaller compared to its counterpart in turbulent flow Thus, it is true that $\left(\frac{dV}{dy}\right)_{y=0}$ for laminar flow < $\left(\frac{dV}{dy}\right)_{y=0}$ for turbulent flow (Anderson, 2017).

Put simply, the eddies within the turbulent layer facilitate the transfer of momentum from the comparatively fast-moving outer regions of the boundary layer to the areas nearer to the surface. As a consequence, the average velocity distribution is characterized by higher velocities in proximity to the surface and an increased total boundary-layer thickness in a turbulent state compared to a laminar boundary layer developed under identical conditions. This leads to higher skin friction in turbulent boundary-layer flow compared to laminar flow (Abbott and Doenhoff, 1959). Nevertheless, a turbulent boundary layer exhibits a higher level of kinetic energy, enhancing its ability to conform to a shape more effectively than a laminar flow.

It may seem contradictory, but turbulence and vortices which contribute to prolonging the attachment of a flow, stand in direct opposition to the desire for low drag. Despite laminar flow causing less drag than any other type, its delicately balanced nature and susceptibility to tripping into turbulence often make it more problematic than advantageous. Once laminar flow breaks down and prematurely separates, the airfoil experiences a loss of lift and heightened drag compared to a scenario where the boundary layer had been initially turbulent yet remained attached (Stinton, 1983).

Reflecting on Equation (1) regarding τ_w, it becomes evident that the laminar shear stress is inherently less than turbulent shear stress: $(\tau_w)_{laminar} < (\tau_w)_{turbulent}$ - a vital fundamental fact. Thus, as mentioned earlier, the skin friction experienced by an airfoil is contingent on whether the boundary layer on the surface is laminar or turbulent, with laminar flow resulting in lower skin friction drag (Anderson, 2017).

In broader terms, the characteristics of the boundary layer play a pivotal role in determining crucial aerodynamic parameters such as the maximum lift coefficient, stalling behavior, form drag values, and, to some extent, etc. Additionally, several factors like object size and texture roughness along with fluid viscosity and velocity affect the nature and expansion rate of this layer, as highlighted by Darrol Stinton (1983).

2.6 Ground Effect

Ground effect is the aerodynamic phenomenon where the airflow around the car is affected by the proximity of the car's underbody to the track surface. Until the early 1980s, it was one of the main contributors to downforce in Formula 1 cars. However, due to several fatal accidents, the FIA banned its use for safety reasons (FIA Foundation, 2024).

In 2022, one of the most groundbreaking aerodynamic alterations to the Formula 1 model took place, causing the return of the apparent ground effect in a quite different form. Lotus' famous skirts (*Figure 2.5*) remained banned, giving way to the introduction of smaller yet equally effective aerodynamic components on the car, ultimately leading to a safer alternative.

Formula 1 cars utilize various aerodynamic devices to induce ground effect, including the side pods, diffuser, and underfloor. As for the wings, the main difference between wing application in aviation and car racing arises from the direct contact of cars with the track surface. Therefore, the wings experience some additional effects due to ground proximity (Seljak, 2008). Of particular significance is the front wing, positioned extremely close to the ground, as we will see in the following section, resulting in the induction of ground effect.

2.6.1 Mechanics of Ground Effect

The primary advantage of the ground effect lies in its capacity to generate less induced drag while producing an equivalent or more amount of downforce. Consequently, wings positioned in close

proximity to the ground are notably more efficient *(Figure 2.18)* (Toet, 2013).

Analyzing Bernoulli's principle, we conclude that downforce is inversely proportional to ground clearance (Soliman et al., 2015). This implies that a wing positioned in close proximity to the ground experiences amplified downforce due to the heightened acceleration of air between the bottom of the wing and the track surface, leading to a reduction in suction pressure (Houghton and Carpenter, 2003). Lower pressure corresponds to higher speed and vice versa. As a result, the flow velocity under the car increases as ground clearance decreases and vice versa.

In addition, when a wing operates close to the ground, the ground interferes with the trailing vortices, diminishing the downwash generated by the wing. This decrease in downwash increases the effective angle of attack of the wing, resulting in more lift and less drag than it would otherwise. This effect is even more pronounced when the wing operates nearer to the ground (Seljak, 2008).

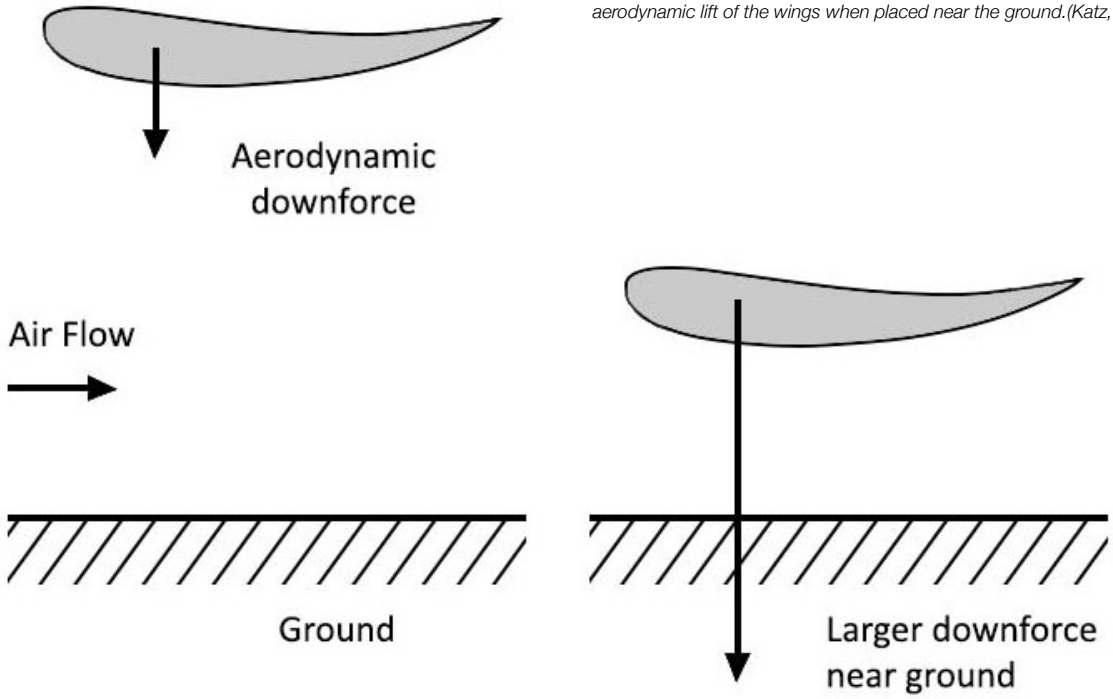

Figure 2.18 Schematic description of the "Ground Effect" that increases the aerodynamic lift of the wings when placed near the ground.(Katz, 1995).

The volume of airflow between the vehicle and the ground is heavily contingent on the car's orientation concerning the track surface. When the car maintains an extremely low ground clearance, it results in positive lift, since there is minimal airflow between the underbody and the ground. Conversely, as ground clearance increases, the airflow generates lower pressures that cause the overall lift to decrease to negative values, and then to increase again as ground clearance continues to increase.

However, if the ground clearance reaches excessively low levels, the adverse pressure gradient over the rear of the wing becomes notably more severe, heightening the risk of a stall. Even in cases where a stall is averted, maintaining such proximity to the ground can give rise to substantial and uncontrollable fluctuations in downforce. These fluctuations stem from inevitable minor alterations in ride height due to track undulations or shifts in vehicle roll and pitch. Sudden and large changes in downward force, which inevitably result in sudden changes to the vehicle's center of pressure, have the potential to render the car exceedingly challenging to handle (Houghton and Carpenter, 2003).

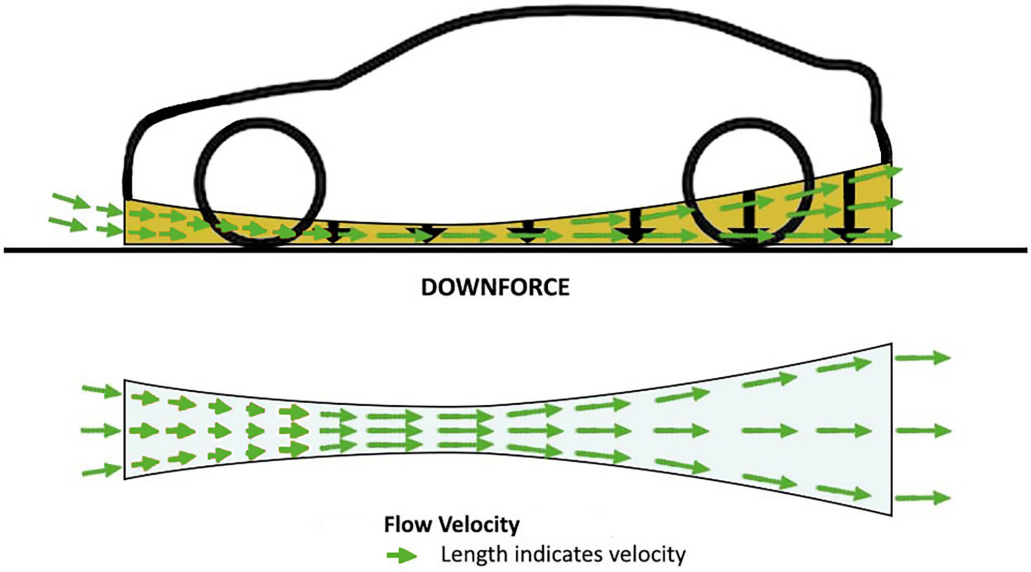

Figure 2.19 Ground effect on a moving car.

In summary, the ground effect operates similarly in all types and profiles of wings. When a wing maintains a considerable height within the sphere of ground effect, the airflow over the suction surface is accelerated more compared to that in a free stream, leading to greater suctions on the suction surface. As the wing draws closer to the ground, this airflow acceleration intensifies, leading to an augmentation in peak suction and pressure recovery. However, there exists a pivotal point at a certain height where the pressure recovery exhibits a steep incline, ultimately resulting in boundary-layer separation at the trailing edge of the suction surface. Further reducing the wing's height continues to amplify downforce production, albeit at a progressively slower rate, ultimately reaching a maximum value before undergoing a decline. Below this critical height, downforce experiences a sharp decrease, a phenomenon previously discussed (Oxyzoglou, 2017).

Ground Effect technology operates on the foundation of the "Venturi Effect," *(Figure 2.19),* a concept derived from Bernoulli's principle. This effect is observed when a fluid that is flowing through

a funnel, in this context, air, is compelled to traverse a narrow section, leading to a concurrent decrease in pressure and an increase in velocity (Oxyzoglou, 2017). The mathematical description of this phenomenon is aptly encapsulated in the Bernoulli equation.

In the realm of fluid dynamics, as a fluid negotiates a constriction, its velocity experiences an increase, adhering to the fundamental principle of mechanical energy conservation. Any increase in kinetic energy, arising from the fluid's acceleration through the narrowing passage, is offset by a corresponding decrease in pressure. To simplify, the speed of air passing through a funnel increases as the space decreases *(Figure 2.19).*

2.6.2 Camber and Thickness in Ground Proximity

It has been observed that several aerodynamic parameters of an airfoil are altered by the presence of the ground. In this subsection, we will analyze the effect of camber, thickness, and angle of attack on the aerodynamic properties of airfoils near the ground. Our objective is to identify the optimal combination of these parameters that leads to the greatest lift increase when close to the ground. We will explore two scenarios: in the first case, we will maintain a constant camber in the wing profile while varying its thickness, and in the second case, we will maintain a constant thickness while altering the camber of the wing profile.

2.6.2.1 Effect of Varying Thickness with Fixed Camber

Enhancing the thickness of an airfoil can initially cause a substantial reduction in the lift coefficient when it operates close to the ground and at low angles of attack. Nevertheless, this situation can be reversed with a slight increment in the angle of attack, due to the favorable ground effect resulting from a decrease in ground clearance. Generally, in the vicinity of the ground, airfoils with lower thickness profiles exhibit higher negative lift generation compared to those with greater thickness profiles. This is a notable departure from the behavior observed in airfoils operating outside the influence of the ground, in free stream (Rad and Kazemi, 2001).

2.6.2.2 Effect of Varying Camber with Fixed Thickness

In this case, we have noted that the variation of camber has a more pronounced effect in com-

parison to thickness variation. For instance, in the case of a symmetric airfoil, that has no camber, no lift is generated in free air. However, reducing its distance from supporting surface results in a substantial downward force.

This phenomenon also applies to low-cambered airfoils at low angles of attack, particularly when their thickness exceeds a certain threshold due to the venturi-shaped channel formed between the airfoil's lower surface and the ground. In applications such as race cars, where enhanced stability at high speeds requires increased downforce, symmetric or even negatively cambered thick wing sections become necessary. Furthermore, elevating the camber in the ground effect leads to a reduction in the normalized lift coefficient. Consequently, a symmetric airfoil experiences approximately 40% more lift increase than a relatively high-cambered airfoil.

Based on our findings, we conclude that the airfoil that works best in ground proximity is the airfoil with the smallest camber and thickness. This configuration yields the highest lift coefficient and represents the most suitable choice, taking the best advantage of the ground effect.

2.6.3 Center of Pressure in Ground Proximity

An additional aerodynamic parameter that undergoes alteration in close proximity to the ground is the center of pressure of the airfoil.

Through the reduction of ground clearance, a consequential adjustment occurs in the positioning of the center of pressure. The ground effect primarily exerts its influence on the pressure distribution along the lower surface of the airfoil. As the distance from the airfoil to the ground decreases, the pressure coefficient (Cp) on the lower surface of the airfoil progressively approaches a value of 1, corresponding to the stagnation condition. This shift towards a more uniform pressure distribution contributes to the rearward relocation of the center of pressure, moving it closer to the airfoil's trailing edge.

2.7 Formula 1 Aerodynamic Devices

2.7.1 Front and Rear Wing

The movement of air around a moving vehicle affects all of its components in one way or another. In a Formula 1 racing car, the wings and body are the two main parts that impact the car's aero-

dynamic shape.

More specifically, the front and rear wings are lifting surfaces that generate downforce to improve the car's performance. They are typically curved on the top surface and flat on the bottom, which creates a pressure difference.

In the early days of Formula 1 racing, the design of front and rear wings was relatively simple. The front wing was a small, flat plate mounted to the front of the car, while the rear wing was a simple airfoil mounted on the back of the car. However, over the years, wing design has become more intricate, incorporating multiple components such as airfoils, endplates, and winglets that collaborate to produce the intended downforce. The number and configuration of these elements are dependent on each team's distinct design approach.

2.7.1.1 Front Wing

The front wing, *(Figure 2.20)*, which is located at the front of the car, operates within a strong ground effect as already mentioned, generating downforce by directing air underneath the car. This improves cornering speed, grip, and stability of the front tires. Its design creates a high-pressure zone at the front, producing about 20-30% of the car's downforce. Furthermore, it is the first part of the car to interact with air, thus, besides creating downforce, its main task is to guide the air efficiently toward the body and rear of the car, as turbulent flow impacts the efficiency of the rear wing. Another function of the front wing is to direct the air around the front wheels in order to reduce the resistance produced by them. In simpler terms, it minimizes the region of turbulent air around the

Figure 2.20 Front wing illustrated by Giorgio Piola in 2023.

[Available at: https://www.motorsport.com/f1/news/the-mercedes-and-ferrari-f1-wing-ideas-many-thought-were-banned/10433837/]

front tires, resulting in less debris being left behind. Achieving this can tremendously benefit other aerodynamic areas of the car, ultimately improving its overall performance. As a result, a well-designed front wing can significantly enhance the car's performance (Fareeq, 2015).

The importance of the front wing is so huge, that even the slightest damage to it will prompt teams to call the driver in for a replacement. Although a pit stop can be time-consuming, it is worth it due to the potential loss of downforce resulting from wing damage. For that reason, the front wing is one of the most quickly replaceable parts in a Formula 1 car, after the tires.

The unparalleled efficiency of the front wing positions it as the utmost aerodynamic device on the car. (Oxyzoglou, 2017)

2.7.1.2 Rear Wing

The rear wing is located at the back of the car *(Figure 2.21)*, and serves several functions, similar to the front wing. It has a short and wide design, with a very small aspect ratio and generates downforce by directing air over the car, improving motoring performance and enhancing traction and stability of the rear tires during acceleration and cornering. This is especially important when the car needs to generate large downforce at a relatively low speed. The rear wing stabilizes the rear end of the car and prevents it from skidding on turns. By creating a low-pressure zone at the back of the car, the rear wing, in combination with the high-pressure zone generated by the front wing, produces a net downforce. The operation of the rear wing takes place within the vehicle's wake, which inherently limits its ability to generate high levels of downforce in comparison to the front wing. Consequently, the efficiency of producing substantial downforce by the rear wing is signifi-

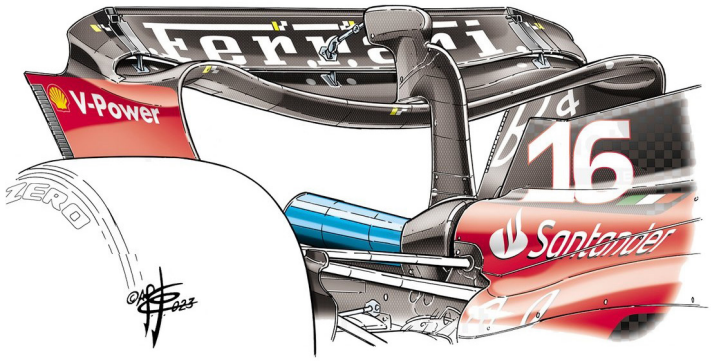

Figure 2.21Rear wing illustrated by Giorgio Piola in 2023.

[Available at: https://www.motorsport.com/f1/news/why-new-rear-wing-hints-at-change-of-f1-approach-for-mercedes-/10438499/]

cantly lower than that of the front wing. Typically, in order to uphold the requisite center of pressure in the car, design engineers try to ensure that the rear wing produces over double the amount of downforce compared to the front wing, but that depends on the type and applications of the car. Modern rear wings contribute approximately 30-35% of the total downforce (Fareeq, 2015).

Note: Drivers face challenges when closely following the car ahead due to a deficiency in grip and downforce. Specifically, when racing in close proximity, cars encounter a reduction of up to 50% in their overall downforce, which is attributed to the turbulent wake generated by the wings and bodywork. The turbulence generated by the leading car causes instability and reduced grip for the trailing car, ultimately leading to a sliding effect. This decline in downforce substantially compounds the difficulty of overtaking maneuvers.

2.7.1.3 Endplates

Endplates are components mounted at the outer ends of a car's front and rear wings *(Figure 2.22)*. They fulfill several essential functions, playing an unequivocally crucial role in optimizing the vehicle's performance. Their main function is to increase the overall efficiency of the wing by controlling the airflow around it. Functioning as vertical "fences," they effectively prevent air spillage over the wing's sides, a potential compromise to its efficiency *(Figure 2.23)* (Tremayne, 2006). The endplates play a pivotal role in directing airflow either over or under the wing, thereby augmenting its overall effectiveness. Specifically, on the inner side, they prevent airflow spillage from the front wing, while on the outer side, they are adeptly shaped to guide air around the front tires. Furthermore, they actively contribute to drawing air over the front wing, maximizing its efficacy, and aiding in smoothing the airflow toward the rear of the car (Tremayne, 2006). But how exactly do endplates work?

Figure 2.22 Front wing enplates illustrations by Giorgio Piola in 2022.

[Available at: https://www.autosport.com/f1/news/how-f1s-new-rules-era-has-impacted-front-wing-philosophy/10422705/]

The pivotal function of this feature is to avert the migration of high-pressure air from the wing's upper surface to the low-pressure region beneath, thereby eliminating induced drag (Oxyzoglou, 2017). Contributing to heightened front wing efficiency and overall performance optimization, the endplate serves to guide airflow towards the rear wing, preventing spillage over the sides and consequentially reducing drag while enhancing the efficiency of other aerodynamic devices (Tremayne, 2006). The endplates play a crucial role in directing the optimal airflow back towards the undertray and subsequently to the diffuser, ensuring the optimal functionality of both these components (Tremayne, 2006). In relation to the tires, endplates redirect airflow around the front tires, strategically diverting oncoming airflow away from them and minimizing drag. This redirection allows the airflow to persist towards the side pods and the car floor, contributing to an overall improvement in aerodynamic (Fareeq, 2015).

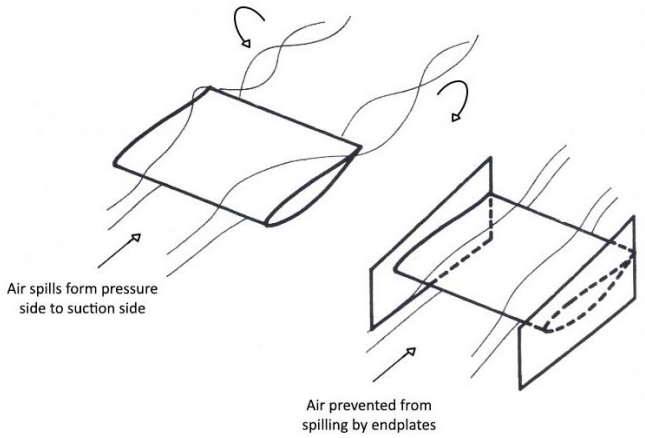

Figure 2.23 The function of the endplate.

Note: Sidepods, as explained by Tremayne (2006), refer to panels situated on the side of the car that house water radiators and an area of deformable structure.

Furthermore, endplates are designed to deter the infiltration of "dirty air" generated by the front tires from reaching beneath the car's floor (Oxyzoglou, 2017).

Similarly, the rear wing endplates serve a specific purpose, primarily focused on preventing air spillage around the wing tips. This effective prevention delays the formation of strongly concentrated trailing vortices, known as induced drag, which represents the primary source of drag for any type of wing (*Figure 2.24).*

Moreover, the rear endplates play an additional role in minimizing the impact of upflow from the wheels. By forcing the airflow to move in a specific direction, they contribute to a delay in the initiation of vortices on the wing compared to configurations without endplates. This is because the motion of the airflow is constrained and can only begin to swirl after reaching the rear wing (Oxyzoglou, 2017; Tremayne, 2006).

All these functions collectively contribute to an overall increase in the lift coefficient (C_L) and a significant reduction in the drag coefficient (C_D), (Fareeq, 2015).

It is important to note that endplates are the parts of the car that tend to undergo the most changes during the design process.

2.7.1.4 Gurney Flap

Gurney flap is a small and very simple yet significant device. Mounted at a large angle, often approaching 90**°,** onto the trailing edge of a wing *(Figure 2.25)*—be it at the front or rear, and having

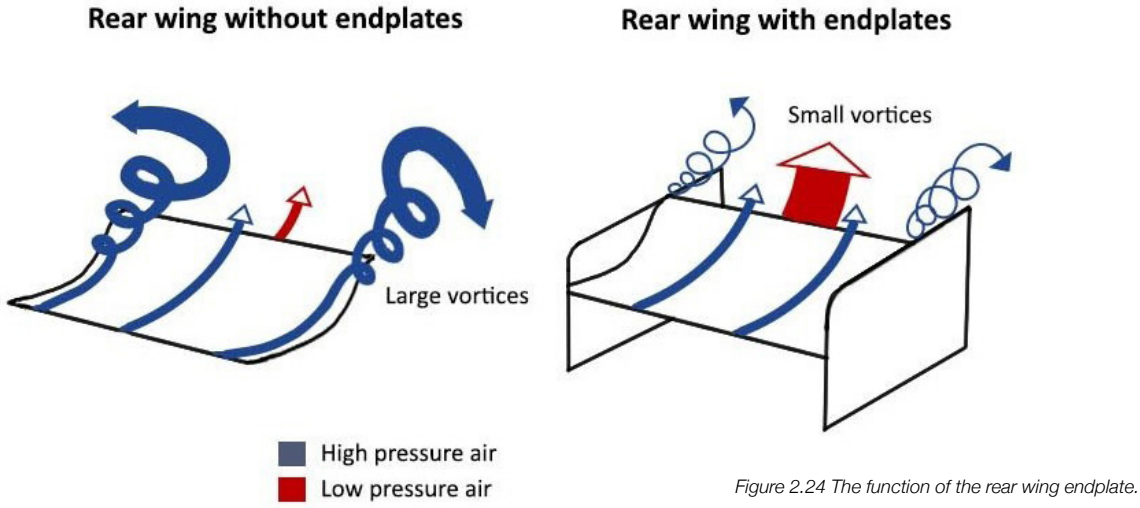

Figure 2.24 The function of the rear wing endplate.

a height on the order of a few percent of the wings' chord, usually less than 5%, is used to make fine adjustments in downforce (Katz, 1995; Milliken and Milliken, 1995; Tremayne, 2006).

Note: It is important to remember that the high-pressure side of the airfoil is called the pressure side, and the low-pressure side is called the suction side.

Its effectiveness becomes particularly pronounced at high angles of attack, where the air struggles to adhere to the contour of the wing's lower surface, potentially leading to detachment (stall), reduced wing efficiency, and heightened drag (Oxyzoglou, 2017).

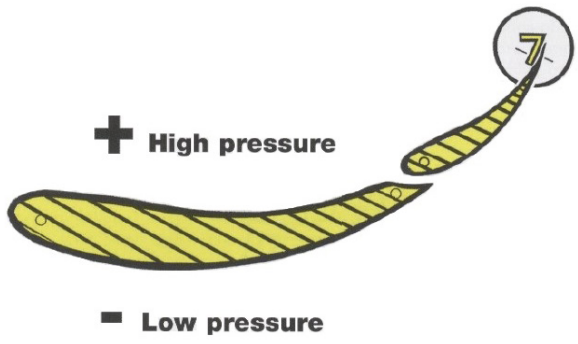

Figure 2.25 Configuration of two airfoil profiles, with the second element featuring a Gurney flap —a lip positioned on the trailing edge (Tremayne, 2006).

In response, the addition of a Gurney flap on the trailing edge, as with any flap, induces a decrease in pressure behind it. This decrease mitigates trailing edge separation on the airfoil to which

it is attached, by drawing the lower flow closer to the wing surface (Milliken and Milliken, 1995; Mortel, 2003). But how does the Gurney flap achieve this?

The Gurney flap's operation involves a reduction in the thickness of the boundary layer on the suction side of the trailing edge due to the sharp turn at the trailing edge. For wings operating near high lift coefficients, this reduction minimizes trailing edge separation, consequently enhancing lift. The flap achieves this by altering pressure distribution—increasing pressure on the wing's pressure side while decreasing it on the suction side, thereby aiding in keeping the boundary layer flow attached to the trailing edge on the suction side of the airfoil (Katz, 1995; Oxyzoglou, 2017).

Moreover, the Gurney flap generates additional lift through the creation of contra-rotating vortices behind it. These vortices, as discussed earlier, can delay or eliminate flow separation near the trailing edge, resulting in increased suction on the airfoil. Additionally, a trapped vortex forms immediately ahead of the flap. The intricate twin-vortex flow field is depicted in Figure 2.26 (Houghton and Carpenter, 2003; Oxyzoglou, 2017).

Figure 2.26 The flow configuration following a Gurney flap (Houghton and Carpenter, 2003).

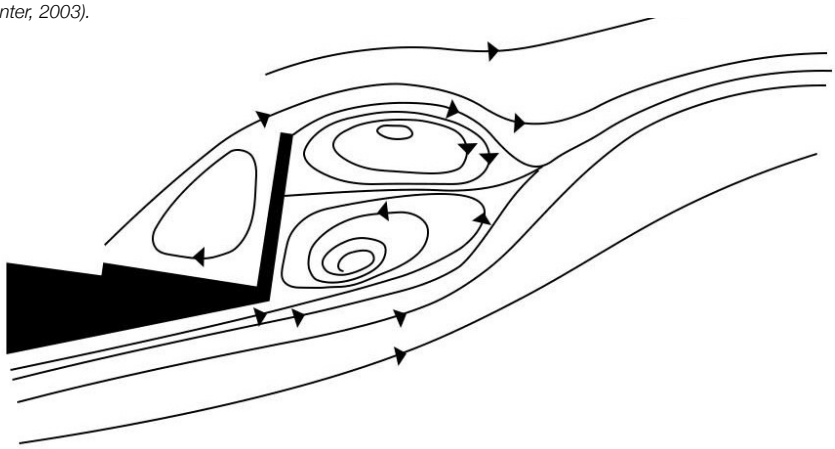

Note: The figure may be misleading as it cannot accurately represent the unsteady nature of the flow field.

On the other hand, when wings operate at lower lift coefficients while having thin trailing edge boundary layers, the addition of a Gurney flap will increase drag and reduce the wing's lift-to-drag ratio (Katz, 1995).

In conclusion, a Gurney flap is a small lip typically set at higher AoAs on the high-pressure side of an airfoil. It significantly enhances the performance of a simple airfoil, approaching the capabilities of a complex high-performance design (Oxyzoglou, 2017). While introducing some additional drag, it permits the wing to operate at higher AoAs, generating more downforce (Mortel, 2003). The

ability to adjust the flap's size offers teams a means of swiftly modifying aerodynamic loads (Katz, 1995; Oxyzoglou, 2017).

Note: The Gurney flap is typically situated on the trailing edge of the wing's last element.

2.7.1.5 Vortex Generators

In the pursuit of optimizing a car's performance, various modifications come into play. Earlier, we delved into the significance of Gurney flaps, and now, we shift our focus to another impactful modification: vortex generators (VGs).

Vortex generators stand out as simple yet highly effective flow control devices, widely acknowledged in the field (Katz, 1995; Milliken and Milliken, 1995). Their strategic placement on the car's bodywork, including sidepods, diffusers, and endplates, imparts versatility. However, our exploration centers specifically on vortex generators located on the car's wings.

VGs are one of the most effective control devices, mainly used to control boundary-layer flows *(Figure 2.27)*. Beyond influencing boundary-layer transition, they excel in delaying flow separation on a wing's suction side *(Figure 2.28)* (Katz, 1995; Milliken and Milliken, 1995). This delay is instrumental in promoting the reattachment of separated boundary layers within separation bubbles, effectively postponing fully developed stalls (Houghton and Carpenter, 2003).

The operational mechanism of vortex generators is distinctive. Introducing disturbances through these devices allows for the forced transition of the turbulent boundary layer, enabling it to stay attached longer. Drag benefits due to a reduction in separated flow can also be gained by using this technique (Katz, 1995).

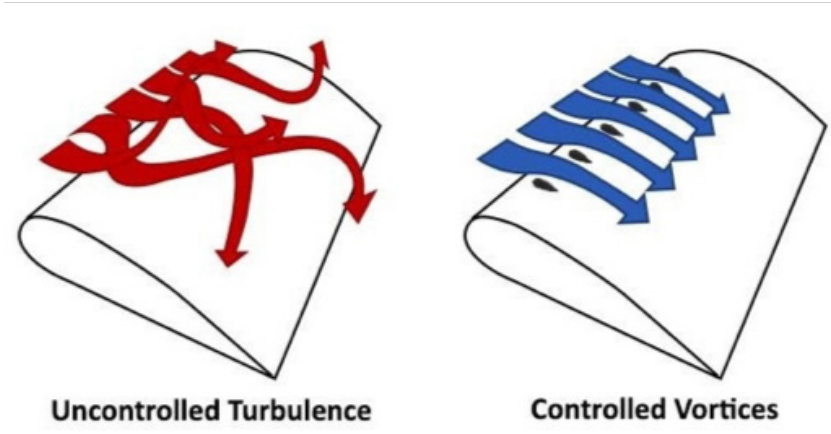

Figure 2.27 Illustration depicting the role of vortex generators in controlling airflow around the wing surface.

Vortex generators exhibit diverse configurations and shapes, as illustrated in Figure 2.28. Their size, typically aligned with the local boundary-layer thickness, facilitates the creation of vortices that infuse fresh momentum from the free stream into the boundary layer (Katz, 1995). Simply put, each vortex generator produces streamwise vortices, fostering increased mixing between the high-energy air in the free stream and outer bounder layer, with the relatively low-energy air nearer the surface. In this way, the boundary layer is re-energized (Houghton and Carpenter, 2003).

Strategically placing these metal strips near the expected separation line adds momentum, effectively delaying flow separation. The adaptability of vortex generators is a key feature, finding application in various locations of incipient separation (Milliken and Milliken, 1995).

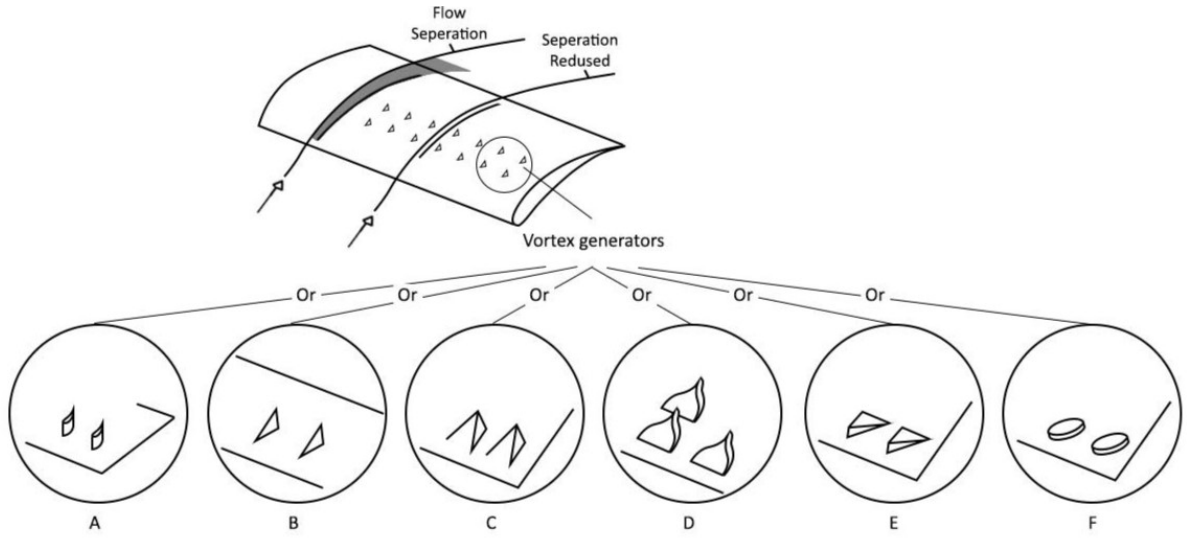

Figure 2.28 Visualization demonstrating how vortex generators (VGs) effectively delay flow separation on the wing's suction side, alongside showcasing various VG shapes.

The overall impact of vortex generators is profound. At higher lift coefficients, they contribute to a gain in maximum lift and a reduction in boattail drag, attributed to minimized separated flow regions. However, at lower lift coefficients, there may be an increase in drag. Therefore, their effectiveness shines when addressing specific flow problems (Milliken and Milliken, 1995)).

In the context of Formula 1, VGs find a prominent place on the car's front wing, a primary source of downforce.

In summary, VGs emerge as sophisticated aerodynamic tools, elevating overall efficiency by effectively controlling airflow. They play a pivotal role in preventing stalls, enhancing downforce production, and contributing to the seamless interaction between aerodynamics and performance in the world of racing.

2.7.2 Downforce, Drag and Angle of Attack

As previously mentioned, downforce and drag are interdependent. The addition of both front and rear wings increases the overall area of the car's model, which results in additional drag. However, the front wings have minimal impact on drag, making the rear wings the primary cause of its existence. To counteract this effect, teams start experimenting and adjusting various features such as the angle of attack, for both wings, according to the requirements of each track (Bhatnagar, 2014).

The angle of attack refers to the angle at which the wing meets the airflow, as previously stated. Increasing the angle, up to a certain point, can result in higher downforce and drag force, and enhance braking. In contrast, decreasing the angle can result in lower forces. Therefore, steeper angles of attack are preferred on tracks with many turns, while smaller angles are more useful on tracks with long straights in order to reduce air drag and achieve higher top speeds (Kurec et al., 2019).

More specifically, regarding the rear wing, angles of attack beyond a certain point can also function as an aerodynamic brake. This generates a significant increase in drag, which decreases the braking distance and leads to improved handling and braking performance.

The significant drag generated by the wings places significant limitations on the car's top speed, as is apparent. However, the benefits gained in cornering speeds due to the increased downforce outweigh the drag penalty (Kurec et al., 2019).

2.7.2.1 Active Aerodynamics

The size and position of the wings on the car, also affect their performance. A larger wing can create more downforce but also drag, while a wing positioned too far forward or backward may not be as effective.

To address these issues, aerodynamic designers came up with the idea of movable airfoils, also known as active aerodynamics. Movable airfoils work by changing the orientation or shape of the wing in real-time to adjust the airflow around the car, with the aim of controlling the amount of downforce or drag produced by it. In Formula One, the most well-known examples of movable airfoils are the drag reduction system (DRS) on the rear wing and the adjustable front wing flaps.

2.7.2.1.1 Drag Reduction System (DRS)

The drag reduction system (DRS) on the rear wing is an innovative and groundbreaking aerodynamic feature that allows the driver to alter the size of the wing during the race at predetermined points of the track. With this modification the driver has the ability to control the amount of downforce the wing generates, either increasing or decreasing it. The DRS system improves the car's performance by allowing it to move faster down the straights and makes overtaking easier. When activated, the wing's leading edge lifts to create a larger slot gap, which reduces the wing's angle of attack and the frontal area of the car. This results in less drag and a boost in top speed (Loução, et al., 2022).

The driver can electronically open the flap by using a button located on the steering wheel. This is only possible if the car is within one second of the leading car and in specific sections of the track designated as "DRS zones", as previously mentioned. The system is deactivated when the driver exits these zones or applies the brakes. However, the effectiveness of DRS can be limited by factors such as wind conditions and the track layout. Additionally, there are restrictions on when and where it can be used. Despite these limitations, DRS has revolutionized the dynamics of Formula 1 and remains an important aspect of the sport.

The adjustable front wing flaps are a feature of the drag reduction system and operate similarly to those on the rear wing. Located in front of the wheels, they can be adjusted by the driver during the race as well. This leads to the intended decrease in drag and increase in straight-line speed. The adjustment of front wing flaps can be achieved through two methods: angle of attack and flap opening. The angle of attack adjustment is similar to the one described earlier, as it refers to the angle at which the wing is positioned relative to the airflow. Flap opening, on the other hand, refers to the angle of the individual flaps that comprise the front wing. By manipulating the opening and closing of these flaps, the driver can fine-tune the amount of downforce generated by the wing to a greater degree (Loução, et al., 2022).

2.7.2.2 Functional Designing

The design of both front and rear wing must be highly accurate since their interaction must be perfectly functional to distribute the aerodynamic loads between the front and rear axles of the car as desired. For example, a slight adjustment of the angle of attack on the rear wing can affect the

amount of downforce generated by the front wing. The balance of the aerodynamic loads acting on the car is fundamental because they can affect the handling of the vehicle. For instance, an imbalance in favor of the rear axle can cause oversteering at high speeds, and a decrease in the load on the front axle can shift the balance of the car towards understeer (Vardhan, 2023).

Understeer is a condition where the front wheels of the car lose traction and slide out towards the outside of a turn. As perceived, it is a negative characteristic reducing the car's cornering ability, resulting in slower lap times coupled with the cause of excessive tire wear and heat, as the front tires are forced to work harder to maintain grip. On the other hand, oversteering is a condition where the rear wheels of the car lose traction and slide out towards the outside of a turn. Unlike understeering, oversteering can be controlled by the driver as he can countersteer to correct the slide and maintain control of the car. However, oversteering is often seen as a driving style preference since drivers prefer a loose or oversteered car that allows for more aggressive turn-in and throttle application, even if it can result in slower lap times and reduced tire life due to the additional sliding (Hasanovic, 2018).

The design and analysis of these wings are different from typical airplane wings. Achieving optimum results requires consideration of multiple factors, due to the strong interactions between the wings and other vehicle components, such as the diffuser, the body, the wheels, or other wings. Both front and rear wings are designed using complex mathematical equations and computer simulations to optimize their shape, position, size, and angle of attack, in order to create wings that effectively manipulate the airflow around the car. All these factors are critical for generating the ideal amount of downforce while maintaining drag force at low levels. Therefore, teams are investing a significant amount of time and resources in aerodynamic research and development, with the aim of gaining a competitive advantage.

Note: Chapter 3 will cover the process of designing and developing a wing.

2.8 Standard Airfoil Parts Used in Formula 1 and FSAE

Formula SAE race cars exemplify finely tuned machines reliant on aerodynamics to optimize performance on the track. Among the critical components, the front and rear wings stand as vital ele-

ments, significantly enhancing downforce, improving grip, and ensuring stability during high-speed maneuvers, as stated and before.

Airfoils, which are cross-sectional shapes embedded into the car's rear and front wings, play a pivotal role in shaping their aerodynamic performance. Formula 1 teams devote extensive time and resources to crafting custom-designed and intricate airfoils meticulously tailored to their precise requirements. This assiduous approach ensures the utilization of highly optimized airfoils, finely tuned to augment the car's performance.

In contrast, Formula Student teams contend with certain limitations, relying on standardized airfoils to streamline the design process and ensure consistent outcomes. These airfoils boast simpler shapes while adhering to specific regulations, designed to meet the required criteria while providing a more straightforward solution compared to the proprietary designs witnessed in Formula 1. However, these standard airfoils are well-established profiles with known aerodynamic characteristics, tested and used in various industries, making them reliable options for Formula SAE teams.

Within this chapter, we delve into the application of standard airfoils for designing the front and rear wings of Formula SAE cars, exploring the selection criteria, aerodynamic principles, and the consequential impact on overall car performance.

Building upon the terminology of airfoils elucidated in chapter 2.4, "Wing Theory and Geometrical Constraints," we acquaint ourselves with essential parameters such as camber, thickness, and chord length. These critical parameters play an instrumental role in determining the aerodynamic characteristics of wings. Armed with this fundamental understanding of airfoil design, we now possess a comprehensive grasp of the criteria underpinning the selection of suitable standard airfoils. Such criteria encompass assessing aerodynamic efficiency, lift-to-drag ratio, performance at different angles of attack, and compatibility with specific speed ranges and track conditions

Note: The selection of airfoils for our car necessitates careful consideration of attaining the desired balance between front and rear downforce production.

Before classifying the standard airfoils used for the front and rear wings, it is important to reiterate the following for their proper selection.

The front wing's contribution to the total downforce generated by the vehicle typically ranges between 20% and 30%, whereas the rear wing's contribution falls within the range of 30% to 35%. However, it's worth noting that actual downforce levels can fluctuate depending on the team's

design philosophy, specific car characteristics, and the demands of individual tracks. Additionally, for the front wing, ground effects, as mentioned in Chapter 2.6, “Ground Effect”, must be taken into consideration.

Below are the various standard airfoils I came across during my research.

2.8.1 NACA (National Advisory Committee for Aeronautics) Airfoil Series

A considerable amount of research has been dedicated to the advancement of airfoil design. Much of this groundbreaking work was carried out by the National Advisory Committee for Aeronautics (NACA), the predecessor to the renowned National Aeronautics and Space Administration (NASA).

Throughout the years, NACA has demonstrated remarkable expertise in creating airfoils endowed with distinctive characteristics, leading to the systematic categorization of these airfoils into specific ‘families.’ Notable examples encompass the NACA Five-Digit Series, NACA 1-Series (Series 16), NACA 6-Series, and NACA 7-Series, among others. However, in the context of Formula SAE (FSAE) competitions, airfoils from the NACA Four-Digit Series Family are the most widely used.

More specifically, let us delve deeper into the NACA Four-Digit Series. As implied by its nomenclature, the four-digit airfoil geometry is defined by a quartet of digits. Each digit holds significance, reflecting camber and thickness distribution characteristics. The first digit denotes the maximum camber as a percentage of the chord length, the second specifies the location of the maximum camber as a fraction of the chord (in tenths) measured from the leading edge, and the final two digits indicate the maximum thickness as a percentage of the chord length (Barnes W. McCormick,1995).

To illustrate, consider the NACA 4412 airfoil: the initial digit ‘4’ signifies a maximum camber of 4% of the chord length, and the second digit ‘4’ denotes the position of maximum camber at 40% or 0.4c (where ‘c’ represents the chord length) from the leading edge, and the concluding ‘12’ designates the airfoil as a 12% thick profile. It is noteworthy that these individual digits hold distinctive aerodynamic implications.

Specifically, the first digit, representing maximum camber, significantly influences lift characteristics, with larger values typically correlating with heightened lift. The second digit, indicating camber

position, dictates the location along the chord where the maximum camber is situated, thereby influencing stability. The final two digits, reflecting maximum thickness, wield considerable influence over drag properties, with thinner airfoils generally exhibiting reduced drag.

This standardized system of NACA airfoils provides remarkable versatility, as the array of 4-digit airfoils allows engineers to select airfoil shapes that align with their specific design objectives. This flexibility facilitates the optimization of performance parameters such as lift, drag, stability, and more. Below, is presented a comprehensive listing of the selected airfoils within this family.

NACA 4412 – Max. Camber (4%) & Max. Thickness (12%)

Characteristics

- Maximum camber is 4% located at 40% of the chord from the airfoil's leading edge
- Maximum thickness is 12% located at 30% of the chord from the airfoil's leading edge

The NACA 4412 airfoil profile *(Figure 2.29)* is a prevalent choice for constructing the front wing. Featuring a low to moderate camber and a moderate thickness, it can efficiently generate higher downforce at specific speeds. This airfoil is a suitable choice for a variety of track conditions because it offers a balanced compromise between downforce production, drag performance, and stalling behavior. In comparison to airfoils with either greater camber or thinner profiles, the NACA 4412 exhibits moderate levels of drag and stalling tendencies (Raymer, 1992).

Specifically, this airfoil is less prone to stalling at low angles of attack and experiences stalling conditions at relatively higher angles. It also has moderate drag characteristics. Compared to airfoils with greater camber or less thickness, this airfoil exhibits gradual and predictable stalling behavior.

This characteristic contributes to its robust performance, as it is less sensitive to changes in the angle of attack, ensuring attached airflow over a broader range of angles. This broad operating range minimizes the risk of encountering stall conditions and provides engineers with greater operational flexibility. Moreover, it demonstrates reduced boundary layer separation at high angles of attack, mitigating turbulence and separation effects on the wing (Anderson, 2017).

The moderate thickness of this airfoil enhances its structural resilience, rendering it suitable for the front wing, which operates under relatively high-loading conditions. Considering the influence of the ground effect, as discussed in previous chapters, a wing profile characterized by lower camber and thickness stands to benefit the most from this phenomenon, making NACA 4412 an ideal candidate for the front wing. Conversely, the NACA 4412 profile may not be an optimal choice for the

formation of the rear wing. In contrast, the NACA 4412 profile may not offer the optimal characteristics for shaping the rear wing. As previously elucidated, rear wings typically necessitate elevated levels of downforce compared to their front counterparts, thus favoring more assertive camber and thickness distributions to attain the desired downforce levels.

NACA 6412 – Max. Camber (6%) & Max. Thickness (12%)

Characteristics

- Maximum camber is 6% located at 39.6% of the chord from the airfoil's leading edge
- Maximum thickness is 12% located at 30% of the chord from the airfoil's leading edge

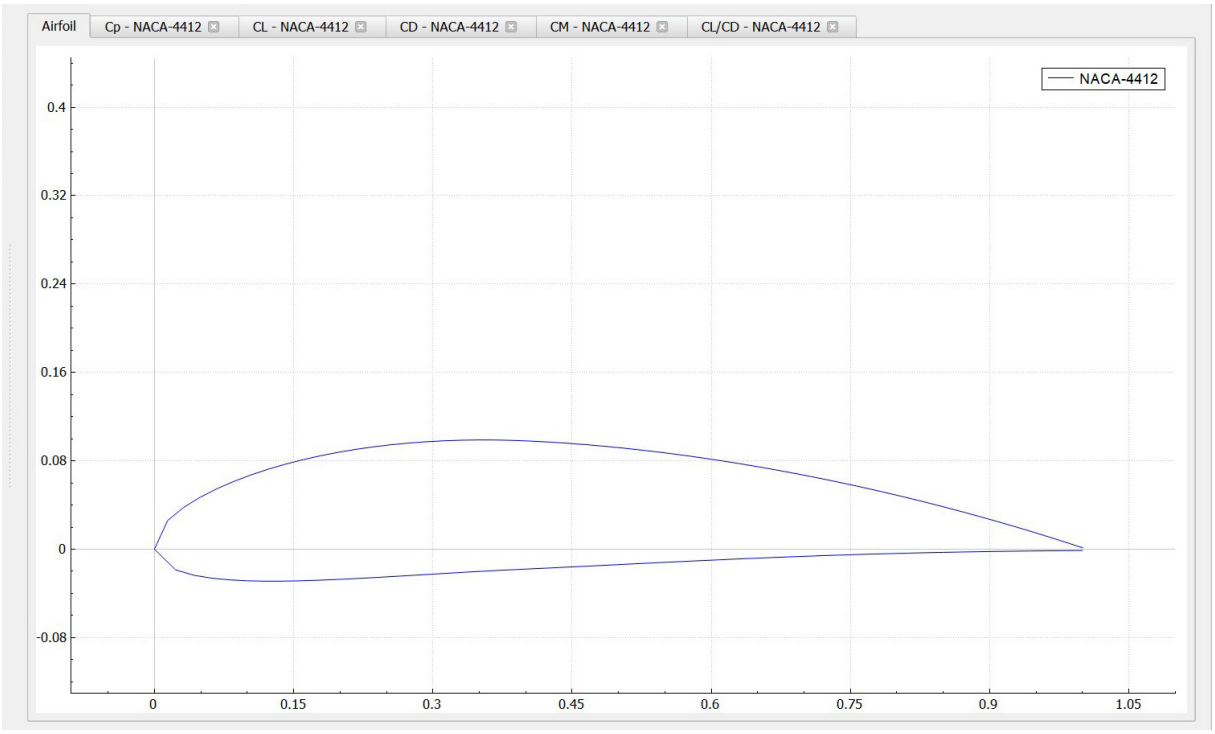

Figure 2.29 A two-dimensional illustration of the NACA 4412 airfoil profile, plotted using the Daedalus v3.1 software.various VG shapes.

The NACA 6412 airfoil (Figure 2.30) exhibits a slightly higher camber compared to the NACA 4412, although it still falls within the category of moderate camber airfoils. Notably, it shares remarkably similar aerodynamic characteristics with the NACA 4412, not only in terms of its very close camber but also its identical thickness.

This airfoil stands out as a versatile option as it can be used to integrate both the front and rear wings. Its camber facilitates efficient downforce production, which can be tailored to provide adequate downforce on the front axle. Additionally, its moderate thickness makes it suitable for handling relatively high loading conditions on the front wing, as in the case of the NACA 4412 (Oxyzoglou, 2017).

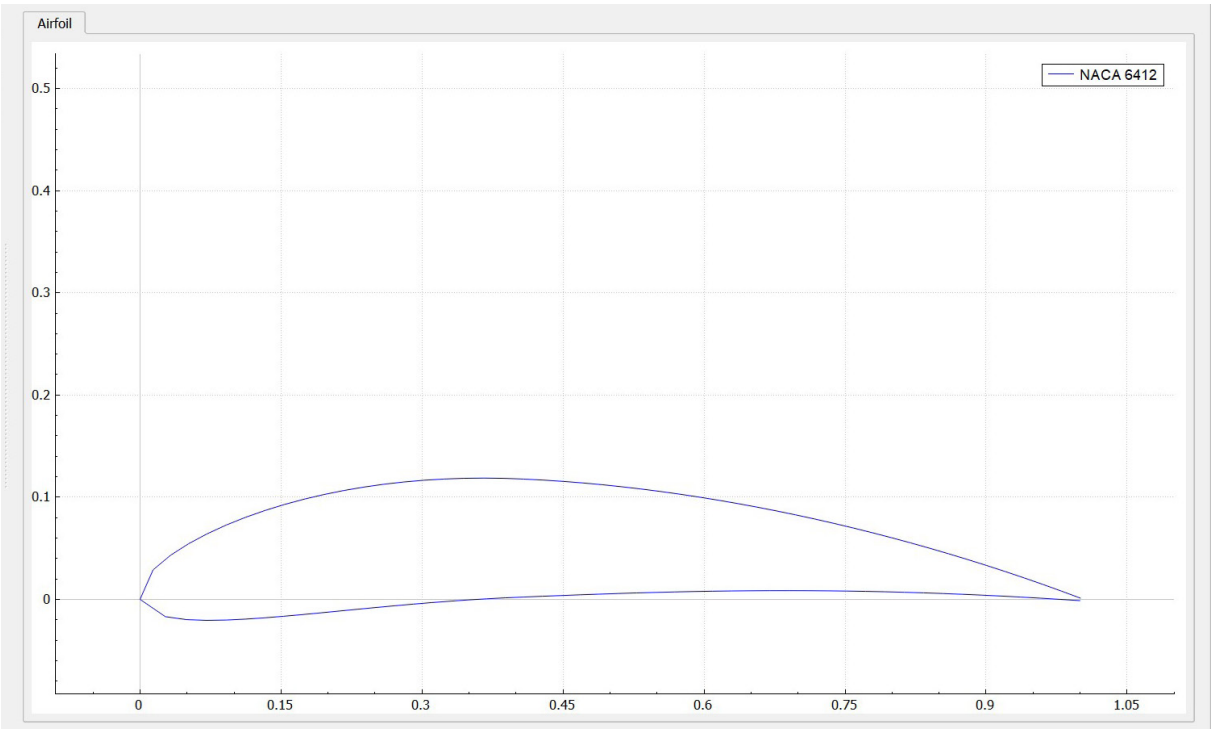

Figure 2.30 A two-dimensional illustration of the NACA 6412 airfoil profile, plotted using the Daedalus v3.1 software.

At the rear end of the car, more downforce is generated. Hence, when used as the rear wing, the NACA 6412 airfoil is typically employed to achieve moderate levels of downforce. This helps to compensate for the minimization of the downforce generated by the rear end, allowing the wing to contribute to the overall aerodynamic balance and stability of the car. Additionally, it aids in maintaining the continuity of the flow without separation.

Generally, the NACA 6412 airfoil is favored for its consistent and predictable aerodynamic performance, coupled with its adaptability for various wing positions, rendering it a highly popular choice among engineers and designers (Upadhye, 2021).

NACA 2408 – Max. Camber (2%) & Max. Thickness (8%)

Characteristics

- Maximum camber is 2% located at 40% of the chord from the airfoil's leading edge
- Maximum thickness is 8% located at 29.9% of the chord from the airfoil's leading edge

The NACA 2408 airfoil *(Figure 2.31)* is typically more effective and efficient when utilized as a rear wing. Falling within the low camber and thickness spectrum, it embodies a low-drag airfoil profile. Its reduced cross-sectional area, in contrast to thicker and more cambered counterparts, results in lower skin friction and pressure drag as well as limited downforce generation. The reduced camber

of the upper and lower surface of the airfoil leads to less pressure differential and consequently diminished downforce production. Nevertheless, being an airfoil with a positive camber, the NACA 2408 generates downforce especially when the Angle of Attack increases up to a certain point where the airfoil becomes stalled.

Thinner airfoils, such as the NACA 2408, are known for being highly sensitive to changes in the Angle of Attack. This sensitivity affects the lift and drag characteristics, which can vary significantly with small changes in the Angle of Attack. On the other hand, low-cambered airfoils, like the NACA 2408, demonstrate efficiency at higher Reynolds numbers (Re), which often correspond to turbulent airflow, higher speeds, and larger sizes. Furthermore, these airfoils tend to have a neutral or near-neutral pitching moment. This means they do not create significant moments around the aerodynamic center, resulting in stable and predictable handling characteristics. These reduced drag and downforce properties of NACA 2408 make it highly suitable for scenarios where maintaining high speeds is essential.

More specifically, the airfoil's reduced drag and enhanced streamlining make it particularly advantageous in high-speed driving conditions. When downforce requirements are moderate and stability and efficiency are of utmost importance, low-cambered airfoils are preferred. As a result, NACA 2408 is beneficial at high speeds where minimizing drag is a priority, excessive downforce is not necessary, and stability and efficiency are key considerations (Abbott and Doenhoff, 1959).

Another notable advantage of this airfoil profile lies in its stall behavior. Due to its low camber, it tends to exhibit a more gradual and stable stall behavior compared to airfoils with higher camber. This characteristic contributes to a reduced likelihood of abrupt loss of lift and control at high Angles of Attack. Additionally, due to its thickness, NACA 2408 achieves potentially higher critical Mach numbers. This characteristic delays the onset of transonic effects, allowing the airfoil to operate at higher speeds before encountering the speed of sound (Pakkam, 2011).

The Mach Number represents the speed of an object, relative to the speed of sound. When the airflow over a specific part of the vehicle reaches the speed of sound, it is referred to as the ***Critical Mach Number.***

Finally, the thin airfoil profile helps maintain flow continuity without separation, contributing to its overall aerodynamic performance. In other words, it prevents flow separation.

In conclusion, the NACA 2408 airfoil, characterized by its low camber and thickness, offers a unique blend of advantages, including reduced drag, limited lift production, and stability across

various aerodynamic conditions. Its aerodynamic efficiency is particularly beneficial for rear-wing applications, enabling improved straight-line speed without compromising the downforce and stability it delivers. However, if eventually chosen for the formation of the front wing, it could take better advantage of the ground effect due to its low thickness and camber (Roy et al., 2021).

NACA 4422 – Max. Camber (4%) & Max. Thickness (22%)

Characteristics

- Maximum camber is 4% located at 30% of the chord from the airfoil's leading edge
- Maximum thickness is 4%

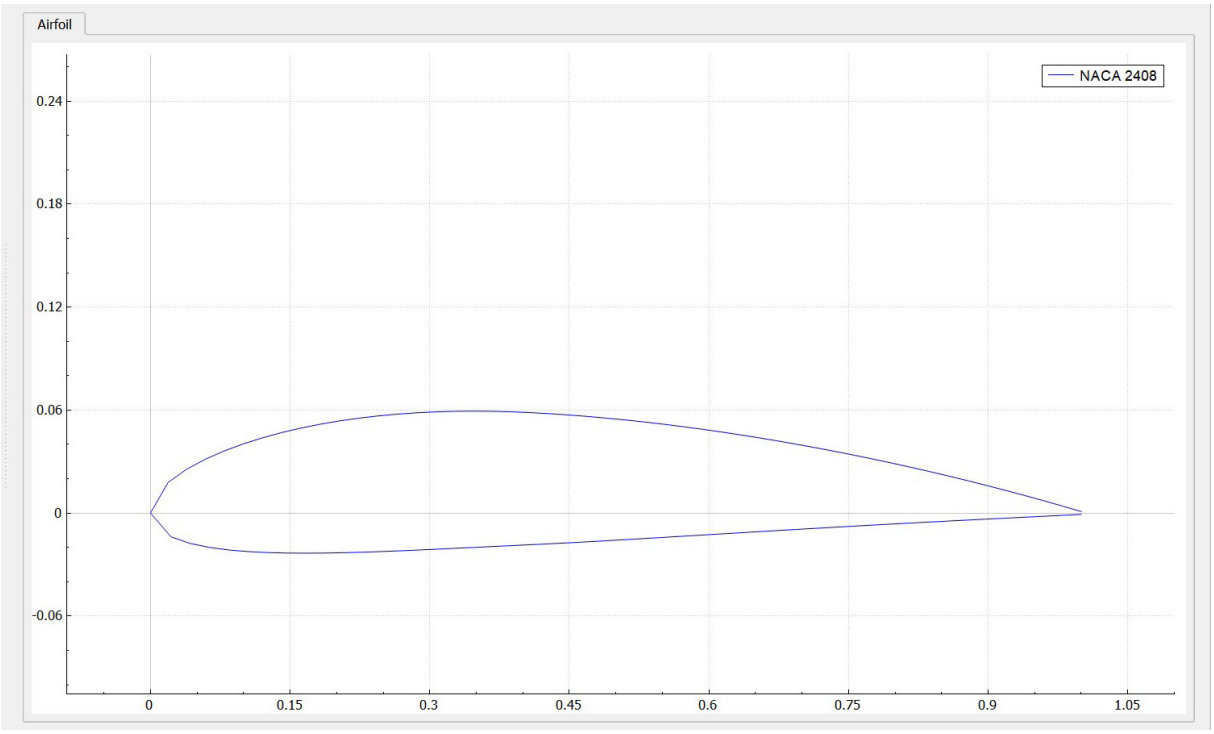

Figure 2.31 A two-dimensional illustration of the NACA 2408 airfoil profile, plotted using the Daedalus v3.1 software.

The NACA 4422 *(Figure 2.32)* is an airfoil with a relatively high thickness compared to the other options but of moderate curvature like most used. Because of the large pressure differential between its top and bottom surfaces, it has a higher maximum lift coefficient value, producing enhanced downforce levels and is a popular choice for low-speed driving conditions. The increased drag associated with its large cross-sectional area can limit its performance at high speeds. Combined with its moderate curvature, the NACA 4422 provides an airfoil profile with predictable and controllable aerodynamic characteristics, as well as a gradual and stable stall behavior, compared to thinner or higher cambered airfoils. Finally, in terms of thickness, it enhances the structural integrity of the airfoil by increasing its stiffness and resistance to higher aerodynamic loads. Consequently,

it constitutes an airfoil profile that is capable of maintaining lower speeds as well as enhancing maneuverability (Pehan and Kegl, 2002).

Due to its increased thickness, it is not usually preferred for the front wing configuration. However, NACA 4422 can be used effectively on both the front and rear wings of a car, depending on the downforce requirements, the need to minimize drag as well as the overall vehicle dynamics and the overall required track needs (Pehan and Kegl, 2002).

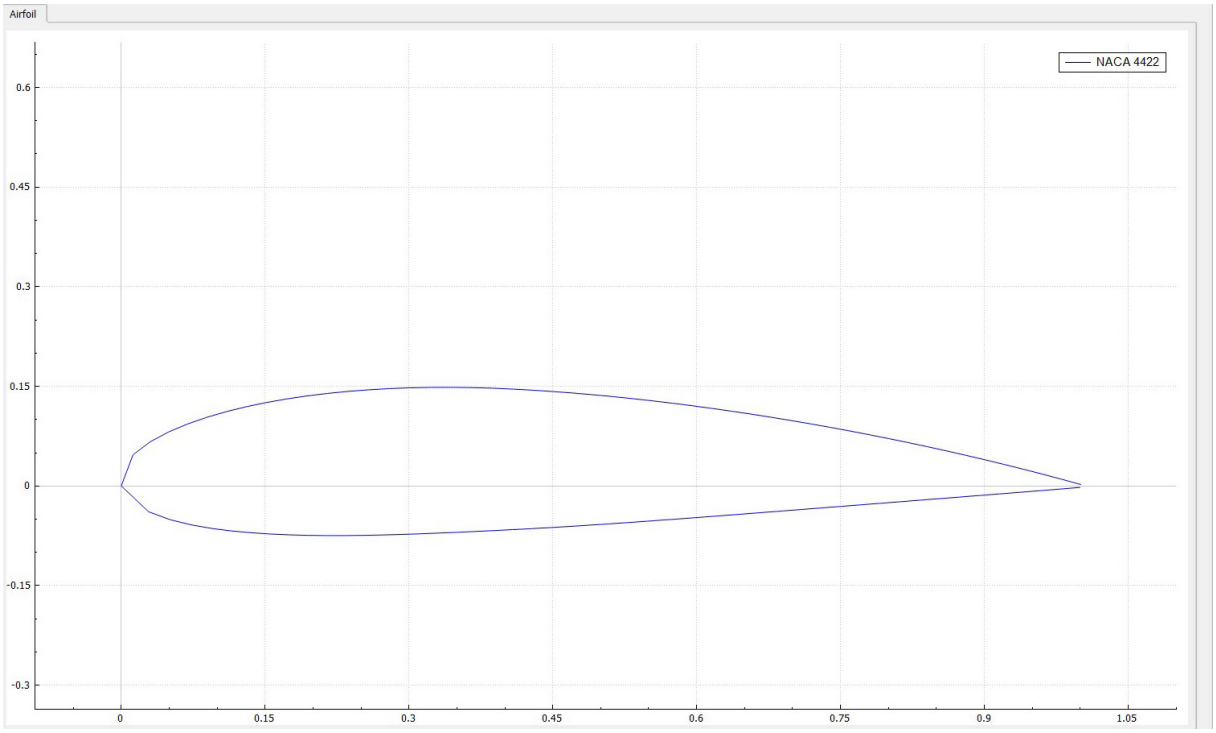

Figure 2.32 A two-dimensional illustration of the NACA 4422 airfoil profile, plotted using the Daedalus v3.1 software.

Additional airfoils from the 4-digit NACA family are employed for their akin aerodynamic characteristics to the previously discussed profiles. Notable examples include the **NACA 6409** airfoil*, (Figure 2.33)*, characterized by a maximum camber of 6% located at 39.6% of the chord from the airfoil's leading edge and maximum thickness of 9% located at 29.3% of the chord from the airfoil's leading edge, and the **NACA 7412** airfoil *(Figure 2.34),* featuring a maximum camber of 7% located at 40% of the chord from the airfoil's leading edge and maximum thickness of 12% located at 30% of the chord from the airfoil's leading edge (Promtong et al., 2020).

It is noteworthy that all the aforementioned airfoils share a common location of maximum camber, positioned at 40% of the chord (2nd digit) from the airfoil leading edge. This consistent placement is observed as it contributes to enhanced downforce, which occurs when the camber is positioned more aft along the chord.

2.8.2 Eppler E-Series Airfoils

Eppler Airfoils, a series of airfoil profiles, is the result of Dr. Richard Eppler's groundbreaking work in computational aerodynamics. Dr. Eppler's career is marked by his pioneering contributions to the design of multiple airfoil profiles. During his tenure at the University of Stuttgart, he furthered the field with the development of the Eppler airfoil design and analysis code. This innovative computational approach integrates a conformal mapping method for precise airfoil design, incorporating predetermined velocity-distribution characteristics. It is augmented by a panel method meticulously analyzing the potential flow around given airfoils and an integral boundary-layer method. Its remarkable efficiency has led to successful applications within a broad Reynolds number (Re) range, spanning from 3 x 10^4 to 5 x 10^7 (Eppler, 1990).

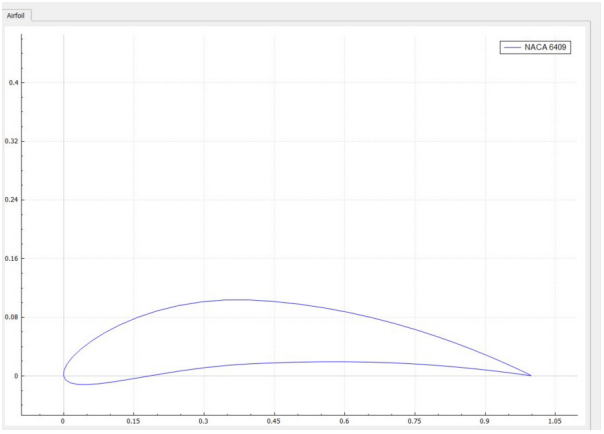

Figure 2.33 A two-dimensional illustration of the NACA 6409 airfoil profile, plotted using the Daedalus v3.1 software.

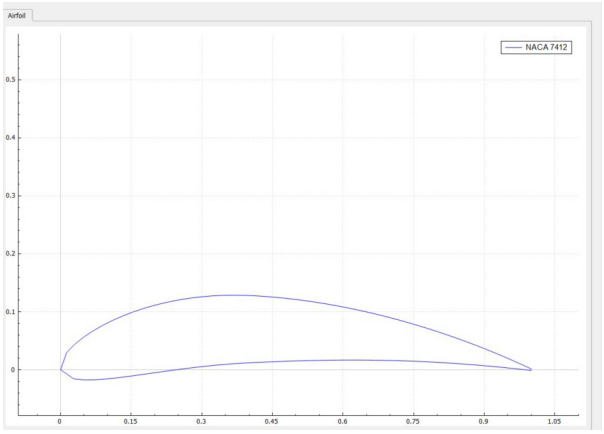

Figure 2.34 A two-dimensional illustration of the NACA 7412 airfoil profile, plotted using the Daedalus v3.1 software.

Eppler E423 – Max. Camber (9.5%) & Max. Thickness (12.5%)

Characteristics

- Maximum camber is 9.5% located at 41.4% of the chord from the airfoil's leading edge
- Maximum thickness is 12.5% located at 23.7% of the chord from the airfoil's leading edge

Considering its attributes, E423 *(Figure 2.35)* emerges as a promising candidate for deployment in the rear wing, particularly in scenarios where the imperative is to generate substantial downforce. This airfoil's well-balanced characteristics, featuring moderate camber and thickness contribute to significant downforce generation while ensuring the preservation of a commendable top speed by maintaining moderate drag levels. E423 distinguishes itself with impressive resistance to stalling, particularly at lower angles of attack, and it encompasses an extended range of angles of attack

where it sustains attached airflow prior to encountering stall conditions (Chavda and Ajudia, 2018).

In simpler terms, this airfoil is less susceptible to variations in angle of attack, resulting in a stall behavior characterized by a gradual and predictable nature across a wide range of angles. Due to its specific geometric configuration, E423 is capable of generating substantial downforce even at low angles of attack, rendering it versatile for diverse applications. An additional advantage conferred by its thickness is its diminished susceptibility to boundary layer separation when compared to thicker airfoils, especially at higher angles of attack. Consequently, it is frequently employed when the mitigation of turbulence and separation effects is of paramount importance (Reza et al., 2016).

While the predictable and versatile nature of E423 renders it eminently suitable for the rear wing, this airfoil's utility extends to specific elements of the front wing, particularly in scenarios where achieving the delicate equilibrium between downforce and drag performance is imperative.

Eppler E426 – Max. Camber (0.6%) & Max. Thickness (10.8%)

Characteristics

- Maximum camber is 0.6% located at 50.6% of the chord from the airfoil's leading edge
- Maximum thickness is 10.8% located at 25.5% of the chord from the airfoil's leading edge

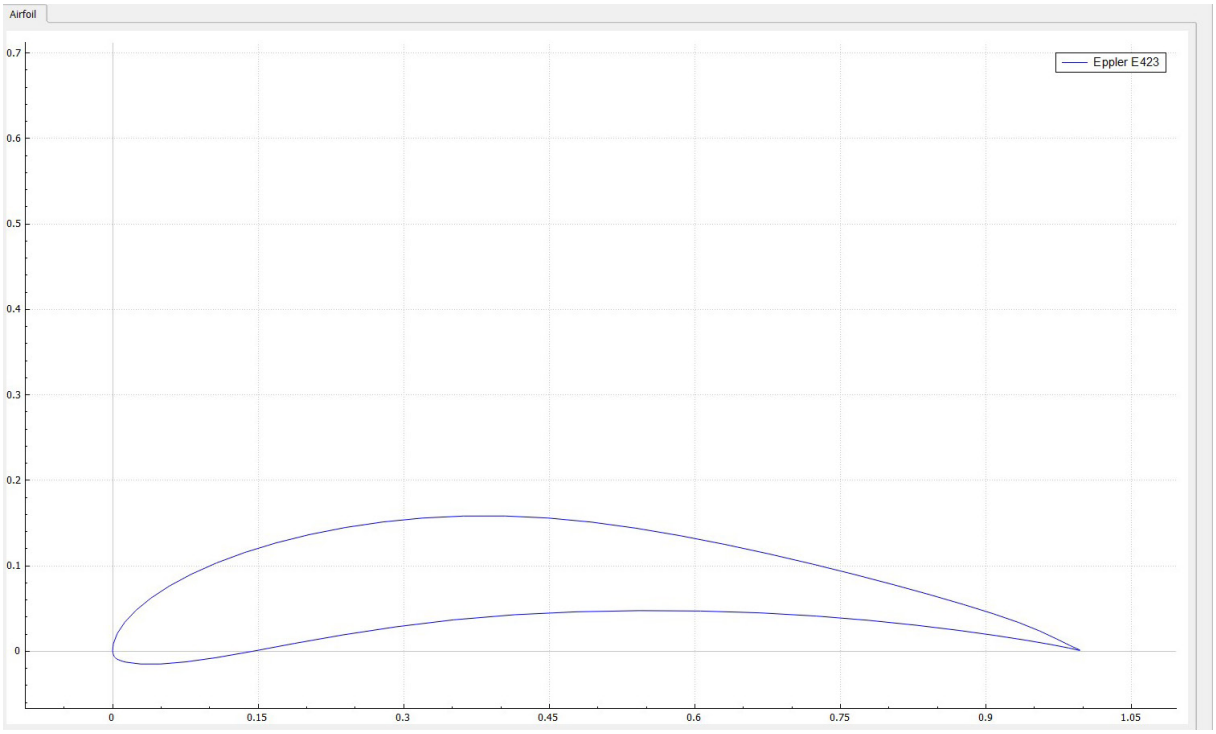

Figure 2.35 A two-dimensional illustration of the Eppler E423 airfoil profile, plotted using the Daedalus v3.1 software.

As an airfoil featuring a very low camber and a low to moderate thickness, the E426 *(Figure 2.36)* proves to be a fitting choice for constructing the front wing. This combination allows for the optimal exploitation of ground effect along the wing's ventral extension, a particularly advantageous feature for the main forewing profile. While the reduced camber and thickness lead to decreased drag, there is a trade-off concerning downforce generation. While downforce is present, it is not as pronounced as observed in airfoils characterized by higher camber (Roy et al., 2021).

This airfoil finds its preference in high-speed applications due to its diminished drag levels and its higher critical Mach number, which enables it to operate at higher speeds before encountering the onset of the transonic effect. Additionally, it is distinguished for its stable stall condition, especially at high angles of attack, owing to its low camber. What's more, it exhibits a decreased likelihood of experiencing an abrupt loss of lift and control at high AoA. Furthermore, it encompasses a relatively extensive range of angles before stalling takes place. Nonetheless, at higher angles of attack, it does experience more pronounced boundary layer separation due to its thickness (Roy et al., 2021).

In summation, the E426 presents itself as an optimal choice for the front wing, manifesting a well-balanced aerodynamic profile that excels in both drag reduction and downforce generation. Furthermore, its remarkable effectiveness in ground effect enhances its overall aerodynamic performance when employed as a front wing, and generally, it renders an ideal wing profile for high-speed applications (Promtong et al., 2020).

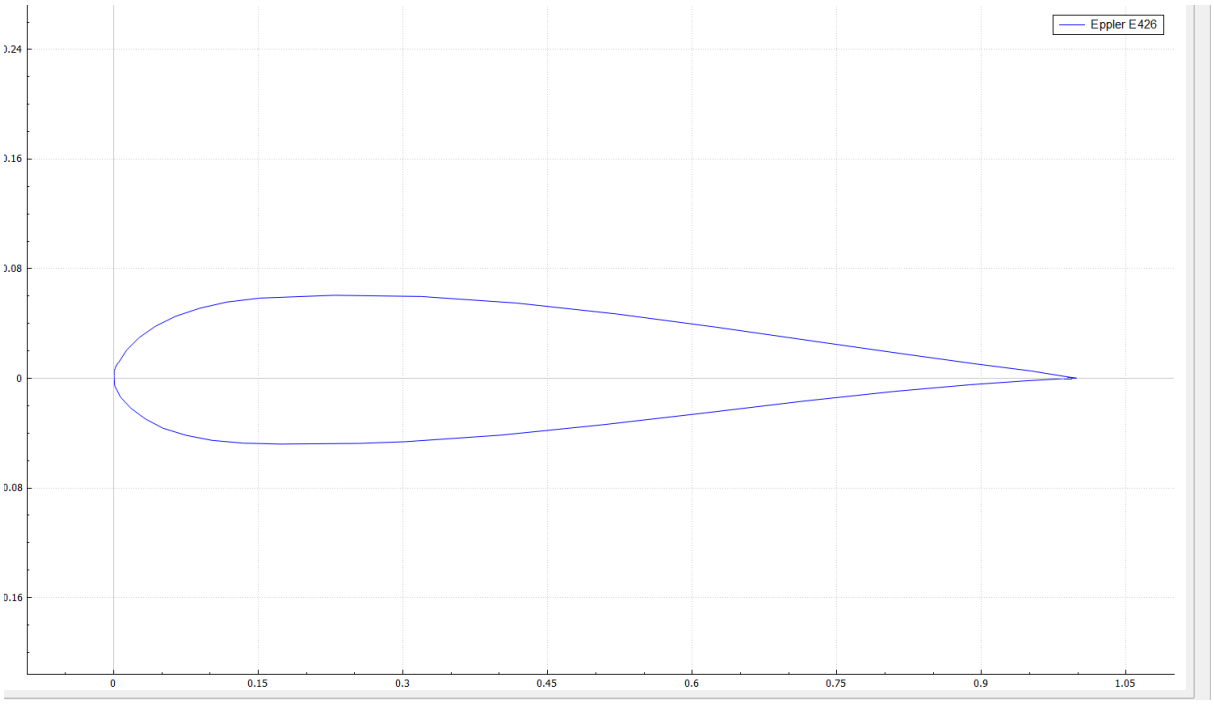

Figure 2.36 A two-dimensional illustration of the Eppler E426 airfoil profile, plotted using the Daedalus v3.1 software.

Eppler E421 – Max. Camber (8.6%) & Max. Thickness (14.5%)

Characteristics

- Maximum camber is 8.6% located at 37.9% of the chord from the airfoil's leading edge
- Maximum thickness is 14.5% located at 26% of the chord from the airfoil's leading edge

The Eppler E421, *(Figure 2.37)*, distinguished by its higher thickness and moderate camber, proves highly effective when employed in the main components of the rear wing. Its attributes suggest a capacity for generating efficient downforce, thereby enhancing the car's traction and stability. With its high thickness, E421 is recognized as a high downforce airfoil. However, careful attention needs to be given to managing the associated drag. It performs optimally at lower speeds, as the drag resulting from its large cross-sectional area can limit its effectiveness at high speeds (Reza et al., 2016).

Concerning stall behavior, the E421 demonstrates a relatively stable response compared to thinner airfoils. Complemented by its moderate camber, stalling at low angles is virtually non-existent. Additionally, it exhibits a decreased sensitivity to variations in angle of attack when compared to airfoils characterized by greater camber, which makes it advantageous for achieving stability and controllability. Overall, it is a fairly predictable airfoil in terms of its aerodynamic characteristics. While its primary application is recommended for the rear wing, the E421 can also be strategically harnessed for specific elements of the front wing (Raymer, 1992).

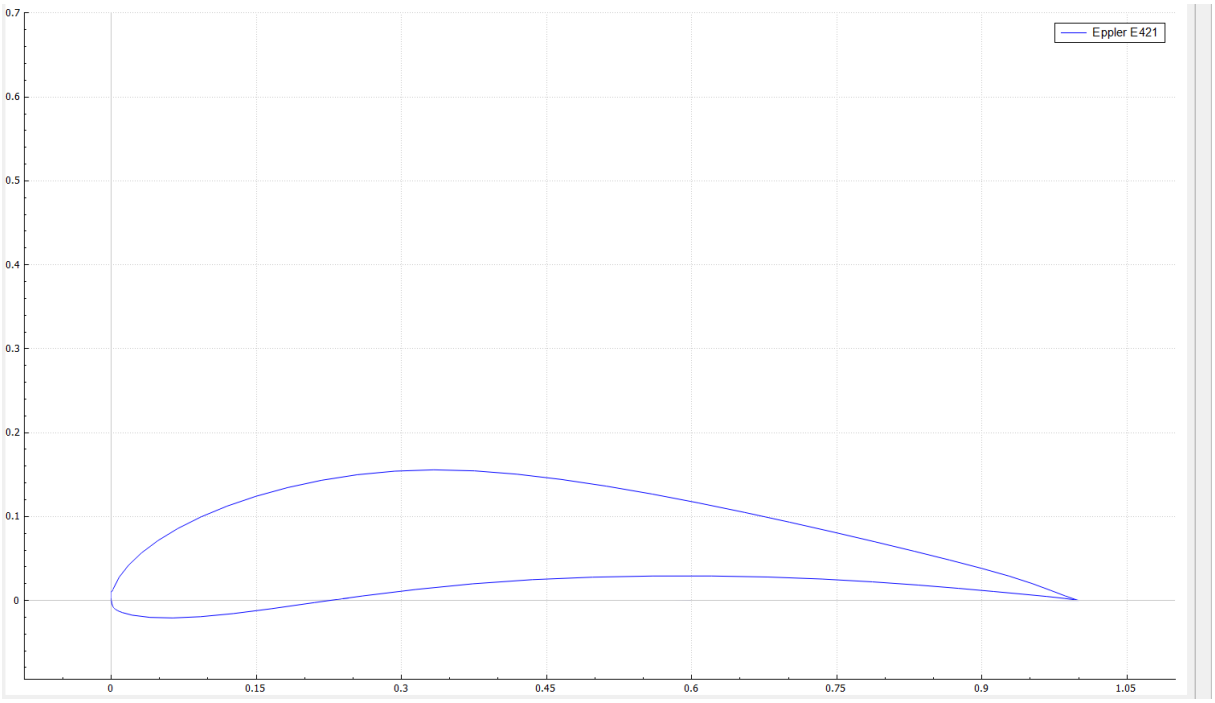

Figure 2.37 A two-dimensional illustration of the Eppler E421 airfoil profile, plotted using the Daedalus v3.1 software.

Note: Both E241 and E426 are acknowledged as high-lift airfoils well-suited for the low Reynolds number (Re) regime, hence for low speeds.

2.8.3 Selig S-Series Airfoils

Another widely employed choice in the context of FSAE aerodynamics is the Selig airfoils, a distinguished family of airfoil profiles meticulously crafted by Dr. Michael S. Selig, a seasoned expert in applied aerodynamics and airfoil design (Selig, 2023). The development process for most Selig airfoils employs a suite of low-speed airfoil design and analysis tools, including the PROFOIL code, the Eppler code, and one of the ISES or XFOIL codes.

The sequence of airfoil design and evaluation typically begins with the rapid interactive design offered by the PROFOIL code. Subsequently, candidate airfoils, meeting predefined performance criteria, undergo a comprehensive assessment. This analysis commences with the Eppler Code and finishes with the application of either the ISES Code or XFOIL Code.

PROFOIL Code: PROFOIL is a specialized tool for crafting low-speed airfoils using an innovative inverse design technique, closely linked to the Eppler Code. Like the Eppler Code, it employs inverse airfoil design principles and incorporates an integral boundary-layer methodology, enabling rapid analysis at designated design points. What sets PROFOIL apart from the Eppler Code is its ability to prescribe the development of both laminar and turbulent boundary layers. In simpler terms, airfoil designers define their desired velocity distribution using a set of specific parameters, and the tool generates the corresponding airfoil shape. However, it's important to note that PROFOIL is a part of a broader toolkit for airfoil design, and additional analysis software is often required to fulfill comprehensive design needs (Selig, 2023).

XFOIL Code: XFOIL is an interactive software package engineered to facilitate the design and analysis of subsonic, isolated airfoils. It encompasses a user-friendly interface featuring a diverse array of menu-driven functions. Among these functions, XFOIL can conduct a comprehensive analysis, both viscous and inviscid, of existing airfoil profiles. The software offers an interactive platform for iteratively designing or modifying airfoils by adjusting surface speed distributions and geometric parameters. Additionally, it excels in airfoil blending, file management with the ability to read and write airfoil coordinates and polar data, and graphical representation of airfoil geometry, pressure distributions, and multiple polar diagrams (Drela, 2013).

ISES Code: The ISES Code, is a two-dimensional viscous aerodynamic design and analysis code.

It addresses the complexities of aerodynamics by solving the two-dimensional Euler equations coupled with an integral boundary-layer model, all facilitated through the global Newton iteration method. This computational requires substantial computational resources, making it a preferred choice in advanced design stages when intricate aerodynamic analyses are necessary (Drela and Giles, 1987).

Selig S1223 – Max. Camber (8.1%) & Max. Thickness (12.1%)

Characteristics

- Maximum camber is 8.1% located at 49% of the chord from the airfoil's leading edge
- Maximum thickness is 12.1% located at 19.8% of the chord from the airfoil's leading edge

The Selig S1223 airfoil *(Figure 2.38)* stands as a versatile choice, effectively deployed in both the front and rear wings of the car, due to its moderate camber and thickness. In the realm of low Reynolds number (Re) airfoils, it distinguishes itself by delivering substantial downforce while having a favorable aerodynamic resistance ratio (Soliman et al., 2015).

Notably, the S1223 exhibits a moderate stall profile, positioning it as the optimal choice among other airfoils with positive camber or symmetric profiles. Its wide range of angles of attack (AoA) before stall onset and reduced sensitivity to AoA changes, especially when compared to thicker airfoils, underscore its adaptability.

Moreover, it showcases superior behavior concerning boundary layer separation at higher AoAs, particularly when contrasted with thicker counterparts. Among the airfoils studied, the Selig S1223 boasts one of the highest lift coefficients, yielding consistent and predictable performance, all while ensuring low drag production (Rab et al., 2018).

In essence, the S1223 strikes an impressive balance between lift generation, drag efficiency, and stall resistance, making it an unwavering choice prized for its adaptability and predictability.

Note: in cases of steep angles of attack it is preferable to use a higher lift version called **S1223 RTL**, which performs *(Figure 2.39)* extremely well at these angles while offering less lift in general. The RTL version is slightly thicker, which means that with the increase in lift there is a relative increase in drag. It has a maximum thickness of 13.5% located at 19.9% of the chord from the airfoil's leading edge, and a maximum camber of 8.3% located at 55.2% of the chord from the airfoils leading edge (Selig, 2023).

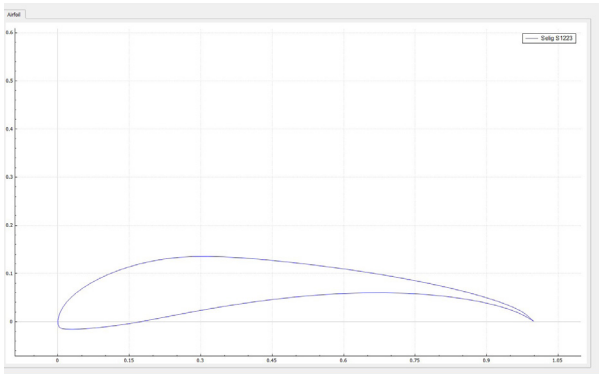

Figure 2.38 A two-dimensional illustration of the Selig S1223 airfoil profile, plotted using the Daedalus v3.1 software.

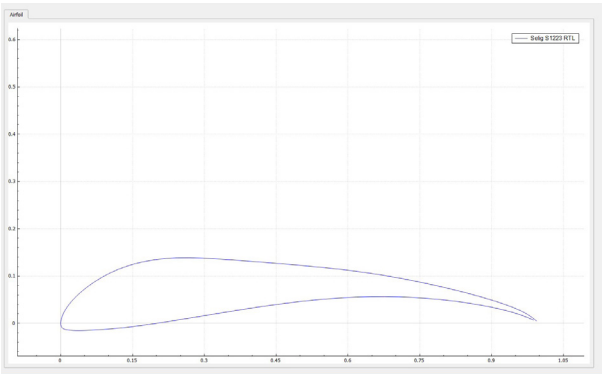

Figure 2.39 A two-dimensional illustration of the Selig S1223 RTL airfoil profile, plotted using the Daedalus v3.1 software.

2.8.4 FX (Wortmann) Airfoils

The Wortmann airfoils, conceptualized in the early 1960s by Dr. F. X. Wortmann from Technischen Hochschule in Stuttgart, exhibit a unique nomenclature system. In this system, 'FX' denotes Franz Xaver, representing Professor Wortmann's initials, while the subsequent two digits signify the airfoil's design year. One or two optional letters may be following, that denote a specialized use, but they can be omitted for general-purpose airfoils. The ensuing three digits indicate the relative maximum thickness multiplied by one thousand. The final digits are also optimal, indicating the relative flap chord percentage, in the case of control surface. For example, the airfoil profile FX 71-L150/30 was designed in 1971. The 'L' designates "Leitwerk", denoting the combined horizontal and vertical tail surfaces in German. The following three digits '150' denote a 15% maximum thickness. The last two digits '30' indicate that the FX 71-L150/30 is optimized for a 30% chord control surface. (Riblett, 1988).

These airfoils are designed primarily for low Reynolds number (Re) applications, which are characterized by laminar flow sections. They typically have a significant amount of camber in the nose, making them highly efficient at low Reynolds numbers (Re). However, it is important to note that these airfoils exhibit significant pitching moments, which should be carefully considered in their application (Riblett, 1988).

FX 74-CL5-140 – Max. Camber (9.9%) & Max. Thickness (14%)

Characteristics

- Maximum camber is 9.9% located at 37.1% of the chord from the airfoil's leading edge
- Maximum thickness is 14% located at 30.9% of the chord from the airfoil's leading edge

The Wortmann FX 74-CL5-140 airfoil profile *(Figure 2.40)* shares notable aerodynamic characteristics with the Selig S1223 profile. Both having moderate camber and thickness are classified as low-speed, high-lift airfoils with moderate stall behavior. However, a distinctive trait of the FX 74-CL5-140 is its tendency to experience an early stall. This implies that, while the loss of lift unfolds gradually, it initiates at relatively modest angles of attack. Despite this, the airfoil maintains efficiency, boasting a favorable ratio. This indicates its capacity to generate substantial downforce with minimal drag. Nevertheless, it exhibits sensitivity to changes in angle of attack (AoA), resulting in potential variations in lift and drag characteristics with even minor AoA adjustments (Pakkam, 2011).

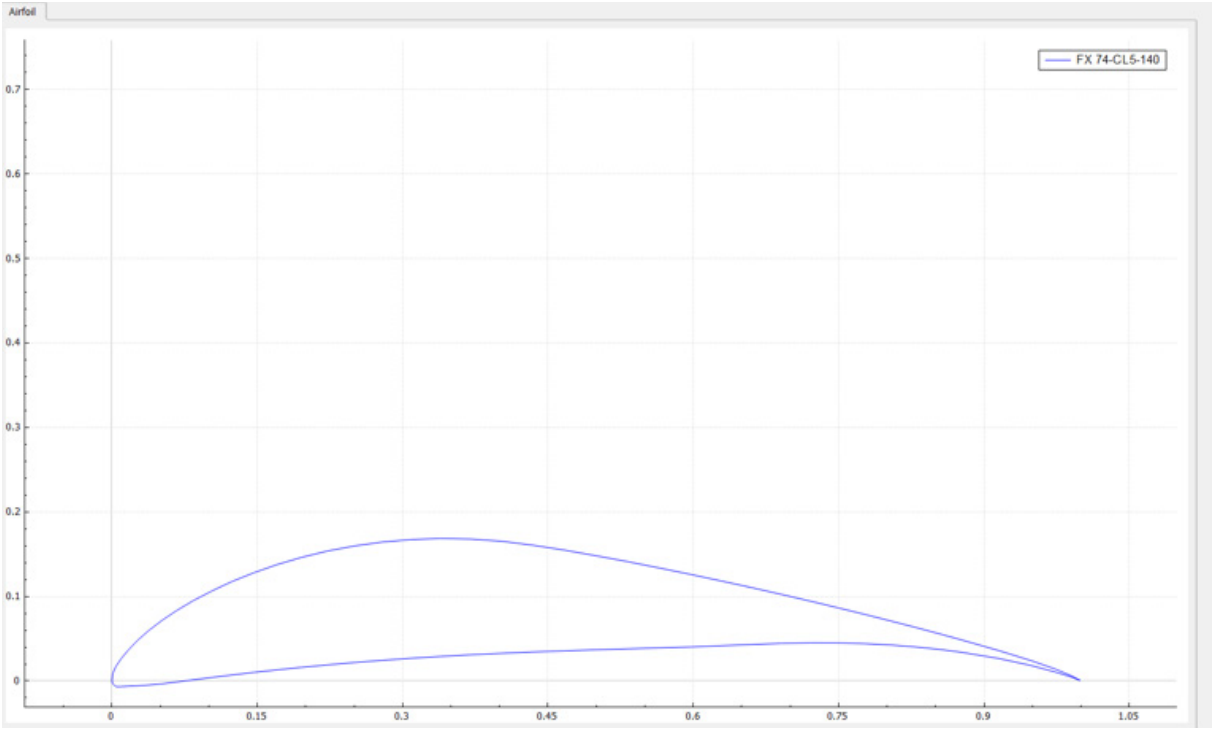

Figure 2.40 A two-dimensional illustration of the FX 74-CL5-140 airfoil profile, plotted using the Daedalus v3.1 software.

FX 63-137 – Max. Camber (6%) & Max. Thickness (13.7%)

Characteristics

- Maximum camber is 6% located at 53.3% of the chord from the airfoil's leading edge
- Maximum thickness is 13.7% located at 30.9% of the chord from the airfoil's leading edge

The Wortmann FX 63-137 airfoil *(Figure 2.41)* is known for its superior aerodynamic characteristics at low Reynolds numbers (Re) and low speeds. According to Magedi Moh. M. Saad (2015), this airfoil has a high lift coefficient, which sets it apart from other airfoils. Additionally, its moderate camber and thickness contribute to a soft stall with minimal unsteadiness, as noted by Selig.

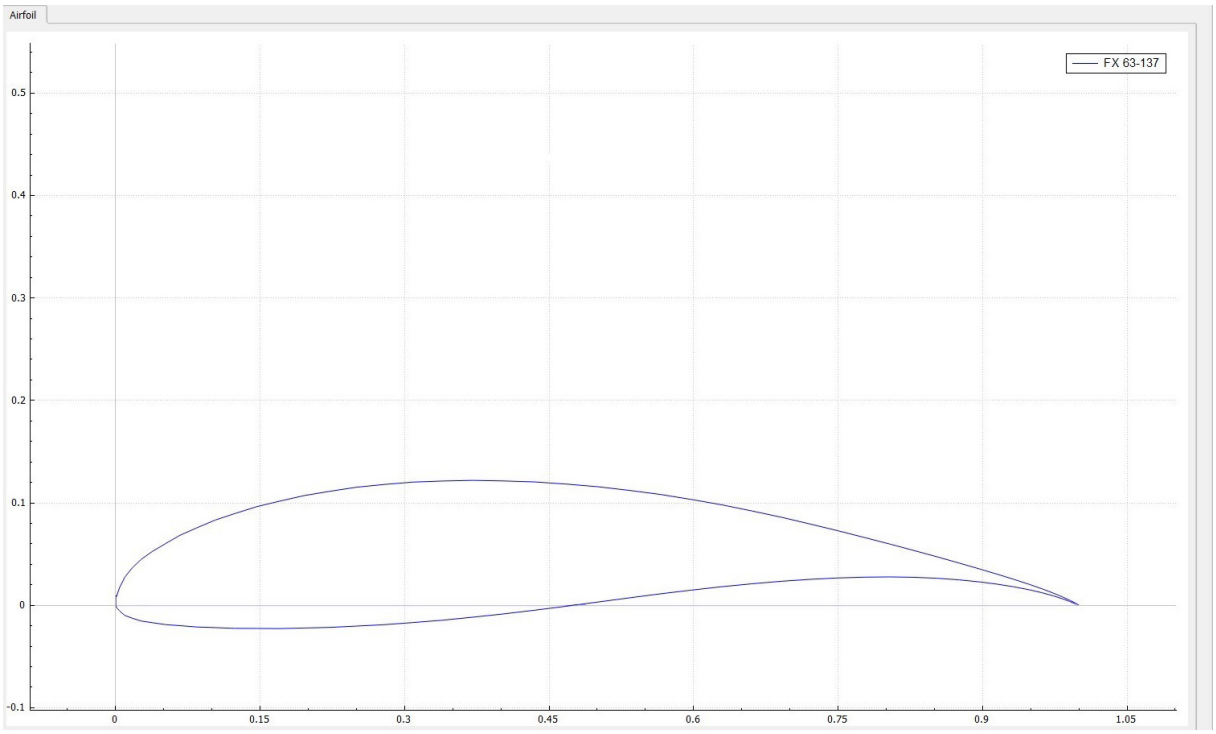

Figure 2.41 A two-dimensional illustration of the FX 63-137 airfoil profile, plotted using the Daedalus v3.1 software.

2.8.5 RG Airfoil Series

The RG Airfoil Series is a family of low Reynolds number (Re) airfoils, named after their designer Rolf Gisberger, a Swiss engineer. These airfoils were initially developed for radio-controlled sailplanes, model gliders, and wind turbine blades. It is important to note that the designation of the RG profiles does not indicate the geometrical characteristics of the profiles (Selig et al., 1989).

RG15 – Max. Camber (1.8%) & Max. Thickness (8.9%)

Characteristics

- Maximum camber is 1.8% located at 39.7% of the chord from the airfoil's leading edge
- Maximum thickness is 8.9% located at 30.2% of the chord from the airfoil's leading edge

The RG15 airfoil (Figure 2.42) (Selig et al., 1989). boasts a maximum thickness of 8.92% and a maximum camber of 1.8%. It is particularly well-suited for low Reynolds number applications due to its excellent aerodynamic performance and behavior under such conditions. Originating in an attempt to provide a superior alternative to the Eppler E180 airfoil, the RG15 stands out for its superior maximum coefficient of lift. While initially intended for use in radio-controlled sailplanes, model gliders, and wind turbine blades as mentioned above, the RG15's versatility extends to a wide range of applications, including race car aerodynamics.

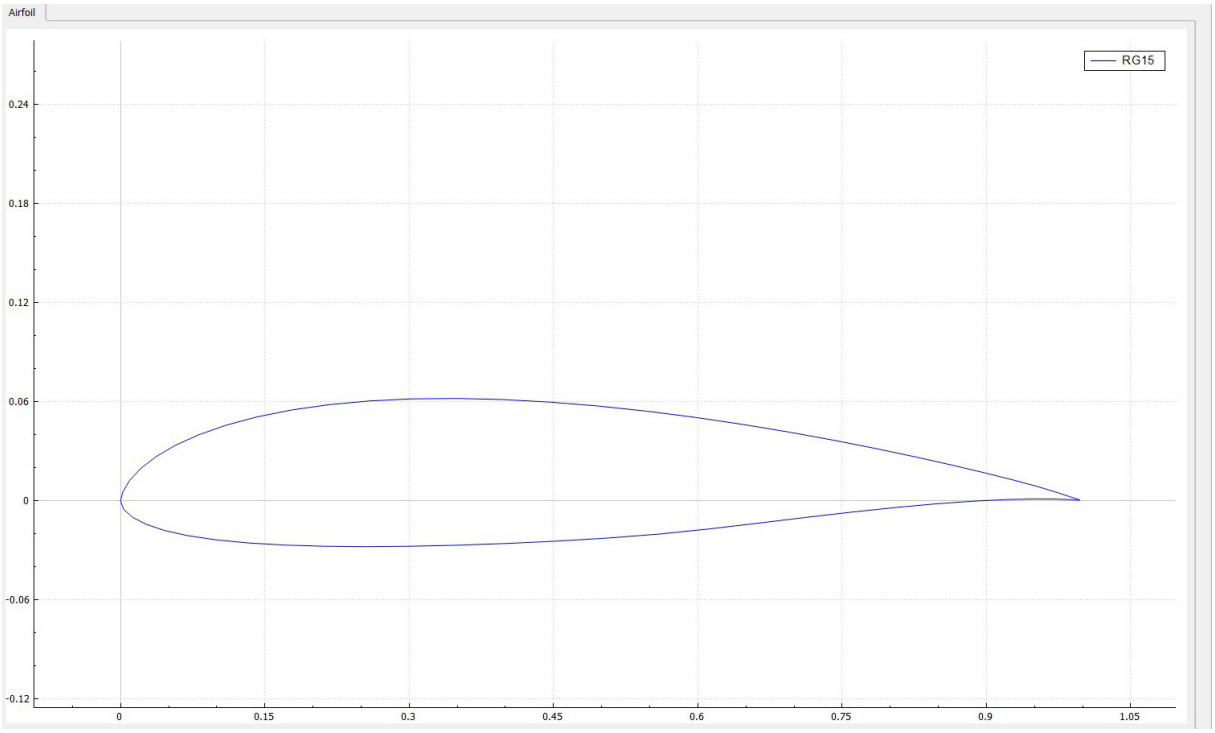

Figure 2.42 A two-dimensional illustration of the RG15 airfoil profile, plotted using the Daedalus v3.1 software.

The RG15's theoretical profile was meticulously designed using the Eppler airfoil code. Considered an "optimum" airfoil, it distinguishes itself by exhibiting lower drag throughout its entirety compared to alternative designs. As part of the RG series of airfoils, the RG15 finds widespread use, striking a balance between efficient lift generation and minimal drag at zero lift. Its exceptional lift-to-drag ratio further solidifies its reputation in aerodynamic applications. Additionally, its low camber and thickness render it advantageous for ground effects when used in the front wing. Its stable and gradual stall behavior, along with its ability to achieve higher critical Mach numbers, offer further benefits. The potential for a higher critical Mach number can delay the onset of transonic effects, contributing to the airfoil's stable and predictable handling characteristics (Leloudas et al., 2020).

DESIGN AND DEVELOPMENT

CHAPTER 3

3.1 Understanding the Requirements

Designing a Formula 1 car is a complex and iterative process that involves several stages of design, research, and development. It begins with understanding the requirements as well as establishing the design goals. In our case, the primary focus is the aerodynamic improvement of the wings, that is, greater downforce generation at relatively low speeds, drag reduction and enhancing the vehicle's stability to minimize lap timing (Gupta and Saxena, 2017; Parmar et al., 2018).

To achieve these goals, the aerodynamicists collaborate and discuss with engineers and technicians the overall approach of the car, and also cooperate with the leaders in the team's other departments. The process includes the use of computer-aided design (CAD), computer-aided manufacture (CAM), computational fluid dynamics (CFD), computer numerical control (CNC), and wind tunnel and on-track testing, to optimize the car's performance. This chapter will explore these terms in more detail.

3.2 Conceptual Work

When Formula 1 engineers begin designing a car from scratch, they first outline the volumes and areas where they will place the car's main parts and bodywork elements.

Their starting point is the regulations, which establish boundaries but do not specify dimensions. Instead, they define areas where engineers can freely position parts. These areas are known as "legality boxes."

Note: Chapter 4 of this thesis will provide a detailed discussion of the regulations for the Formula SAE competition.

As mentioned earlier, aerodynamicists collaborate closely with other departments within the team to design the car. This process is a race against time, with tight deadlines and simultaneous tasks, highlighting the importance of production planning.

3.3 Production Schedule

During the design phase, the primary challenge lies in coordinating and managing numerous parallel processes, each dedicated to a specific aspect of the car. Adapting programs based on

progress in each area is essential.

Establishing the overall design and production schedule is a major undertaking. Throughout this process, challenges may arise, underscoring the importance of regularly updating the schedule to meet car production deadlines. While there are opportunities for adjustments at certain points, there are also instances where making modifications becomes impractical (Carpentiers, 2018).

3.4 Design Process

More specifically, the design of the non-mechanical parts of the car requires an understanding of two main aspects: producing volumes that result in effective aerodynamics, and creating a coherent, stiff structure to ensure rigidity. Depending on which component we are referring to, both of these aspects are more or less important (Carpentiers, 2018).

Compared to other racing series, Formula 1 cars are unique to each team, with a low percentage of standard parts used. Therefore, once the requirements are established and the volumes have been set, the next step is the creation of the conceptual design.

Engineers, detailed develop tens of thousands of individual parts that a Formula 1 car is consisting of, with the help of Computer-Aided Design (CAD) software (Dahlberg, 2014). Aerodynamicists, in particular, meticulously design the geometries for the car's aerodynamic package. This involves generating a range of potential designs that meet the requirements. CAD allows for easy visualization and modification of the design and is a more efficient and cost-effective design process since a digital 3D model of the car and its components are created and no physical prototypes are required (Oxyzoglou, 2017). Additionally, with CAD is possible to determine the dimensions of all the parts and how they are assembled. As previously mentioned, during this phase, engineers experiment with various wing shapes, sizes, and orientations while also considering the interaction between the wings and the rest of the car (Ansys, 2024).

3.5 Design Analysis and Optimization

Once the conceptual design is complete, the next step is to analyze and optimize it. The two main tools used by aerodynamicists for shaping a Formula 1 car are the wind tunnel and computational fluid dynamics (CFD).

3.5.1 Computational Fluid Dynamics (CFD)

Computational Fluid Dynamics (CFD) is a branch of fluid mechanics that, with the help of numerical methods and algorithms, produces quantitative predictions of fluid flow and heat transfer phenomena based on the conservation laws (conservation of mass, momentum, and energy) governing fluid motion (Hu, 2012). Is built upon the Navier-Stokes equations, which explain the behavior of fluid particles (Soliman et al., 2015). These equations establish the correlation between the velocity, pressure, temperature, and density of a moving fluid, as well as how they vary across time and space (Oxyzoglou, 2017). Viscous stresses and pressure forces are also considered in these equations. Nevertheless, due to their nonlinear nature, solving these equations analytically is an extremely challenging task.

CFD simulations employing the Navier-Stokes equations have a vast range of applications, including aerodynamics, hydrodynamics, combustion, and heat transfer. In the Formula 1 industry, CFD software is utilized to enable designers and engineers to simulate, visualize, and quantify airflow structures and the spatial distribution of aerodynamic pressure forces generated on a car's bodywork. This software generates a velocity contour, which visually represents the velocity distribution in the car's body (Senthilkumar et al., 2021). This allows teams to test, optimize, and fine-tune the car's design, study the effects of various design parameters, such as angle of attack, make adjustments, and determine its optimal shape and size before building a physical prototype (Jackson, 2018; Kurec et al., 2019; Senthilkumar et al., 2021). Insights gained from simulation values can be used to evaluate the effectiveness of design changes and provide a detailed prediction of the car's performance on the race track (Tzanakis, 2012). Specifically, this process provides valuable insights into how air flows around and through the car, producing results such as the coefficient of drag, coefficient of lift, downforce, velocity, and pressure counter. By using this process, areas of high drag, low downforce, turbulence, high or low velocity, and separation can be identified (Dharmawan et al., 2018; Nasir et al., 2012).

The spectrum of CFD capabilities ranges from the ability to produce accurate solutions of very simple flows to, handling highly complex geometries and industrial problems (Oxyzoglou, 2017).

Teams can assess a car's aerodynamics by simulating various driving scenarios and types of airflow around the vehicle's aerodynamic devices, including laminar and turbulent flow, quickly and cost-effectively, making CFD software a more accessible and efficient choiceKurec et al., 2019).

Remember: Laminar flow is smooth and steady with a predictable motion of fluid particles, with orderly sliding of the adjacent layers of fluid past each other. In contrast, turbulent flow is random and chaotic, with inherently volatile motion. This means that the velocity and pressure change continuously with time within substantial regions of the flow. The form of the flow depends on Reynold's number (Re). At high Reynolds numbers (Re), the flow becomes turbulent, while at low Reynolds numbers (Re), the flow remains laminar (Hetawal et al., 2014; Soliman et al., 2015; Versteeg and Malalasekera, 2007).

As a result, CFD enables the analysis of aerodynamic issues along complicated F1 bodies across a wide range of conditions. It is an essential technology for engineers working in fluid mechanics, as it allows them to solve complex problems and avoid the need for costly and time-consuming prototype testing. Someone can say it is sort of a virtual wind tunnel (Tremayne, 2006).

3.5.2 Wind Tunnel Testing

The CAD models created earlier are intended to represent the primary features of the car that affect the airflow around it. They are designed to be relatively simple, without excessive detail which would significantly increase the Reynolds number (Re) throughout the vehicle and potentially hinder the calculations from converging (Soliman, 2015). This saves the team a lot of time since the process of CFD analysis and design modification is iterative. Shapes and volumes are refined repeatedly until the desired optimization is achieved while ensuring that all technical specifications and performance requirements are met. Simple CFD evaluations provide a simple yet effective starting point for identifying the most promising designs, to be turned into scale models and then sent to the wind tunnel for further testing (Parmar, 2018; Soliman, 2015; Doddegowda et al., 2006). CFD simulations are essentially the initial step before wind tunnel validation, which ensures the accuracy of their results (Hetawal, 2014; Kurec, 2019). No aerodynamic design is complete without validating it in the wind tunnel (Doddegowda et al., 2006).

Wind tunnel testing is an evaluation process where a scale model of a car is placed on a moving road and air is blown through it at a controlled speed (*Figure 3.1)*. The model is attached to a support system that allows it to be positioned at different angles to the airflow, while sensors on the model measure the acting forces. Wind tunnels enable aerodynamicists to simulate the airflow around the car in a controlled environment, and by using them, they aim to generate consistent loads in a wide range of scenarios. Although it is more expensive as it requires the creation of a physical model and

specialized facilities, it produces more accurate results than CFD, by considering real-world factors.

Compared to wind tunnels, CFD is a less expensive and time-consuming method with faster design cycles, simulation parameters that are easily modified, and a wider range of conditions, such as changes in temperature, humidity, and altitude. Furthermore, CFD allows for a more detailed analysis of the airflow around the car, including areas that are difficult to measure in a wind tunnel (Pehan and Kegl, 2002). However, CFD simulations heavily rely on modeling assumptions, the accuracy of boundary conditions, and, the quality of the mesh, with small errors leading to significant discrepancies between the simulation results and the actual flow behavior. Additionally, it requires considerable computational resources and expertise to set up and operate. Due to its limitations and potential for numerical errors, CFD is not always sufficient. Therefore, wind tunnel testing is the perfect complement (Dahlberg, 2014).

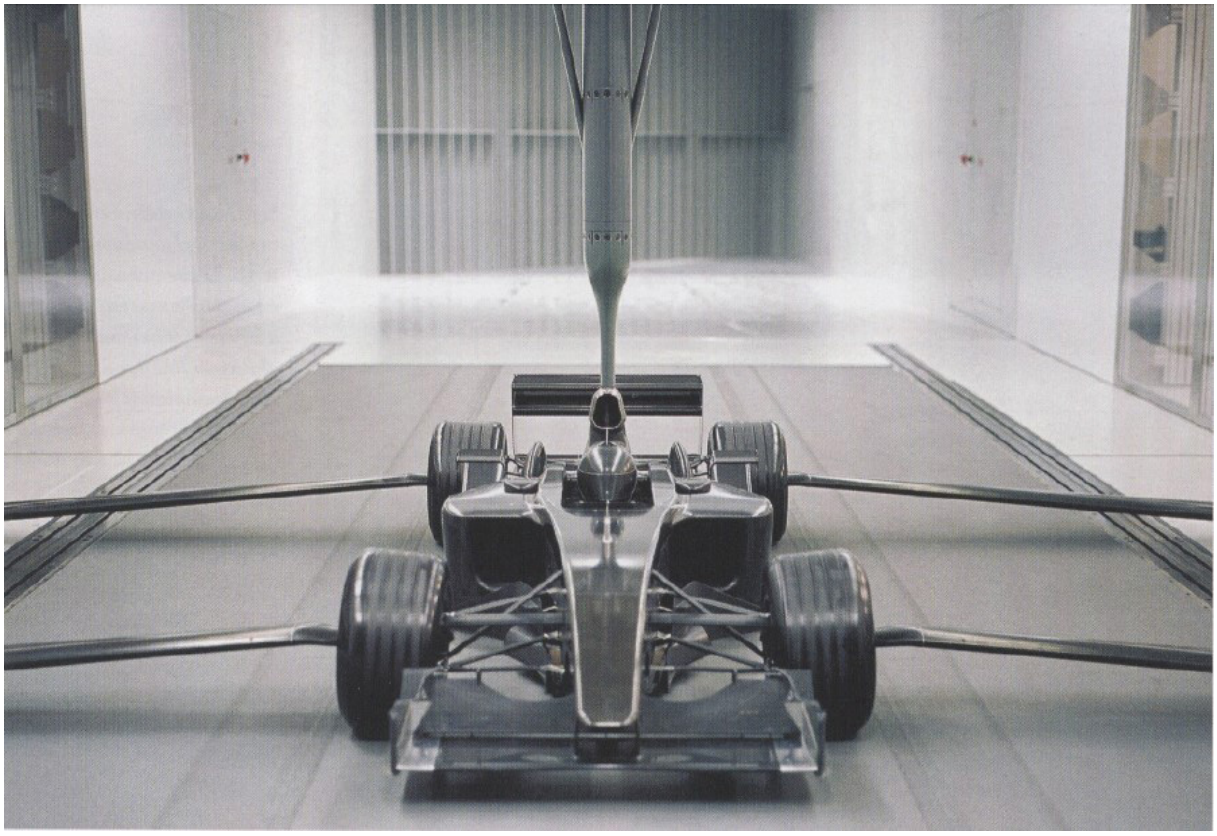

Figure 3.1 A Formula 1 car positioned in a wind tunnel (Tremayne, 2006)

3.6 Production Phase

Upon defining the geometries, teams proceed to transform their digital vision into solid parts. CAD enables the creation of detailed 3D electronic files specifying dimensions and assembly instruc-

tions for each part. When a design is complete in CAD, it can then be loaded into CAM (Computer Aided Manufacturing).

CAM takes charge, initiating the preparation of the model for machining. It generates a supplementary file containing the control program for a Computer Numerical Control (CNC) machine tool. Machining is the controlled process of transforming raw material into a defined shape through actions like cutting, drilling, or boring. Essentially, CNC programs the precise motions and movements required to materialize the digital design into a physical part (Ansys, 2024).

Specifically, Computer Aided Manufacturing (CAM) refers to the use of software and computer-controlled machinery to automate manufacturing processes. Utilizing tool paths, G-code, and CNC machines CAM transforms 3D CAD models into physical products. Note: G-code is the "language" used to convert machining instructions for import into a CNC machine.

CAM software further refines the model for machining, conducting essential tasks. These actions include checking for geometry errors that may affect the manufacturing process, creating tool paths for the model, setting coordinates for the machines to follow during machining, and defining necessary machine parameters like cutting speed, among others (Ansys, 2024).

To summarize, CAD and CAM serve distinct yet complementary roles. While CAD primarily focuses on the creation of a digital representation of a product or part, encompassing its functionality, CAD focuses on how to make it, by writing the code that controls CNC machines.

3.7 Final Stages

All of the manufactured parts must undergo inspection prior to integration into the car. Extensive testing is conducted to ensure optimal reliability before the assembly process commences. Once dimensions and required rigidity levels are validated, sub-assemblies and assemblies are meticulously put together and subjected to dynamic testing. This comprehensive evaluation replicates on-track conditions, ensuring components are primed for peak performance during operation (Hasanovic, 2018).

CHAPTER 4

FSAE REGULATIONS

The realm of Formula SAE (FSAE) competitions combines cutting-edge engineering, innovation, and competitive motorsport. As aspiring engineers come together on this global platform, they are challenged not only to design and construct high-performance race cars but also to navigate a meticulously crafted set of regulations that govern every aspect of their creations. Among the many disciplines that shape the FSAE experience, aerodynamic regulations stand as a linchpin, exerting a pivotal influence on the design, performance, and efficiency of the vehicles on the track.

This chapter explores the aerodynamic regulations within the Formula SAE framework, examining the guidelines and constraints imposed on participating teams.

In this section, the Formula SAE aerodynamic regulations will be explored, analyzing the key fundamental principles and their impact on the design and performance of the next generation of race cars.

FSAE is responsible for establishing and enforcing the rules and regulations that govern the sport, with the aim of promoting safety and fairness in Formula Student racing.

Throughout the years, changes are constantly being made in an effort to continuously improve the performance, efficiency, safety, and environmental impact of the sport, including new aerodynamic restrictions and car regulations.

As our understanding of aerodynamics has advanced, race cars with the same engine have been able to achieve higher cornering speeds. Consequently, additional regulations have been implemented over the years to ensure a level playing field for all competing teams.

In accordance with the standards set by the Formula SAE competition, the regulations outlined in the SAE International Rule Book 2024 version 1.0 serve as the authoritative guide for participants. These regulations are essential for ensuring safety, fair competition, and innovation within the Formula SAE community.

In the scope of this thesis, the focus is selectively directed towards regulations pertinent to the front and rear wings of Formula SAE vehicles. The discussion centers specifically on rules that impact the design, dimensions, and performance of these aerodynamic components, to maintain a targeted and relevant exploration.

The primary emphasis is placed on key elements that govern vehicle requirements, technical aspects, and technical inspection.

4.1 Vehicle Requirements (V)

Ground Clearance (V.1.4)

In compliance with Formula SAE regulations regarding Ground Clearance, (SAE International, 2024, Chapter V - Vehicle Requirements, Section V.1 Configuration, Rule V.1.4), the design and execution of the vehicle's ground clearance play a pivotal role in ensuring optimal performance during dynamic events. Rule V.1.4.1 stipulates that ground clearance must be sufficient to prevent any portion of the vehicle, except the tires, from making contact with the ground throughout dynamic events. Moreover, according to Rule V.1.4.2, intentional or excessive ground contact of any part of the vehicle, other than the tires, will result in the forfeiture of a run or an entire dynamic event. This includes the prohibition of sliding skirts or any other devices that, by design, fabrication, or as a consequence of movement, come into contact with the track surface. Furthermore, any unintended contact with the ground that could lead to damage or, in the opinion of the Dynamic Event Officials, pose a risk of damage to the track, will result in the forfeiture of a run or an entire dynamic event.

4.2 Technical Aspects (T)

Aerodynamic Devices (T.7.1)

In accordance with Formula SAE regulations about Aerodynamic Devices, (SAE International, 2024, Chapter T - Technical Aspects, Section T.7 Bodywork and Aerodynamic Devices, Rule T.7.1), meticulous attention is directed toward the safety and design considerations of aerodynamic elements. According to Rule T.1.7.1.4, found within the Aerodynamic Devices subsection (T.1.7.1), specific requirements govern the design of forward-facing edges that could potentially come into contact with pedestrians. Notably, all such edges, including wings, end plates, and undertrays, are mandated to have a minimum radius of 5 mm for horizontal edges and 3 mm for vertical edges. This regulation extends to the edges themselves or additional permanently attached pieces designed to meet the stipulated radius requirements. Such meticulous guidelines underscore Formula SAE's commitment to both performance and safety in the design and implementation of aerodynamic features.

Length (T.7.5)

In the domain of Technical Aspects (T), a critical focus is placed on the intricacies of Bodywork and Aerodynamic Devices, specifically within the subsection dedicated to Length, (SAE International, 2024, Chapter T - Technical Aspects, Section T.7 Bodywork and Aerodynamic Devices, Rule T.7.5). Rule T.7.5 dictates the spatial parameters of Aerodynamic Devices in the plan view. According to this regulation, no part of any Aerodynamic Device should extend beyond 700 mm forward of the fronts of the front tires, and similarly, no part should exceed 250 mm rearward of the rear of the rear tires *(Figure 4.1).*

Width (T.7.6)

Continuing within the realm of Technical Aspects (T), a meticulous exploration of Bodywork and Aerodynamic Devices reveals the nuanced regulations surrounding the Width of these components, (SAE International, 2024, Chapter T - Technical Aspects, Section T.7 Bodywork and Aerodynamic Devices, Rule T.7.6). In the plan view, the positioning of any part of an Aerodynamic Device is subject to precise guidelines based on its location relative to the wheel axles. When positioned forward of the centerline of the front wheel axles (T.7.6.1), the device must be inboard of two vertical planes parallel to the centerline of the chassis, touching the outside of the front tires at the height of the hubs. Between the centerlines of the front and rear wheel axles (T.7.6.2), the device must be inboard of a line connecting the outer surfaces of the front and rear tires at the height of the wheel centers. Rearward of the centerline of the rear wheel axles (T.7.6.3), the device falls within the Rear Aerodynamic Zone *(Figure 4.1)*. These intricacies reflect Formula SAE's dedication to refining not only the aerodynamic efficiency but also the precise spatial placement of these devices, ensuring optimal performance within the defined safety and regulatory parameters.

Height (T.7.7)

As the exploration of Technical Aspects (T) delves deeper into the nuances of Bodywork and Aerodynamic Devices, Rule T.7.7 outlines precise regulations concerning the Height of these components, (SAE International, 2024, Chapter T - Technical Aspects, Section T.7 Bodywork and Aerodynamic Devices, Rule T.7.7). The stipulations for the Height (T.7.7) are detailed to ensure an optimal balance between aerodynamic functionality and safety considerations. According to Rule T.7.7.1, the height restrictions are contingent on the location of any part of an Aerodynamic Device. Specifically, in the Rear Aerodynamic Zone, the device must not exceed 1200 mm above

the ground, while outside of this zone, the height limit is set at 500 mm above the ground. Moreover, for components positioned forward of the centerline of the front wheel axles and outboard of two vertical planes touching the inside of the front tires at the height of the hubs, the height is restricted to 250 mm above the ground. Rule T.7.7.2 provides exceptions for Bodywork height when located between the transverse vertical planes positioned at the front and rear axle centerlines, and inside two vertical fore and aft planes positioned 400 mm outboard from the centerline on each side of the vehicle.

Note: The Rear Aerodynamic Zone encompasses the volume situated rearward of the Head Restraint Plane and inboard of two vertical planes parallel to the centerline of the chassis, which touch the inside of the rear tires at the height of the hub centerline. This prescribed space establishes a critical framework for the design and placement of rear aerodynamic components, ensuring a standardized and regulated approach in Formula SAE vehicles.

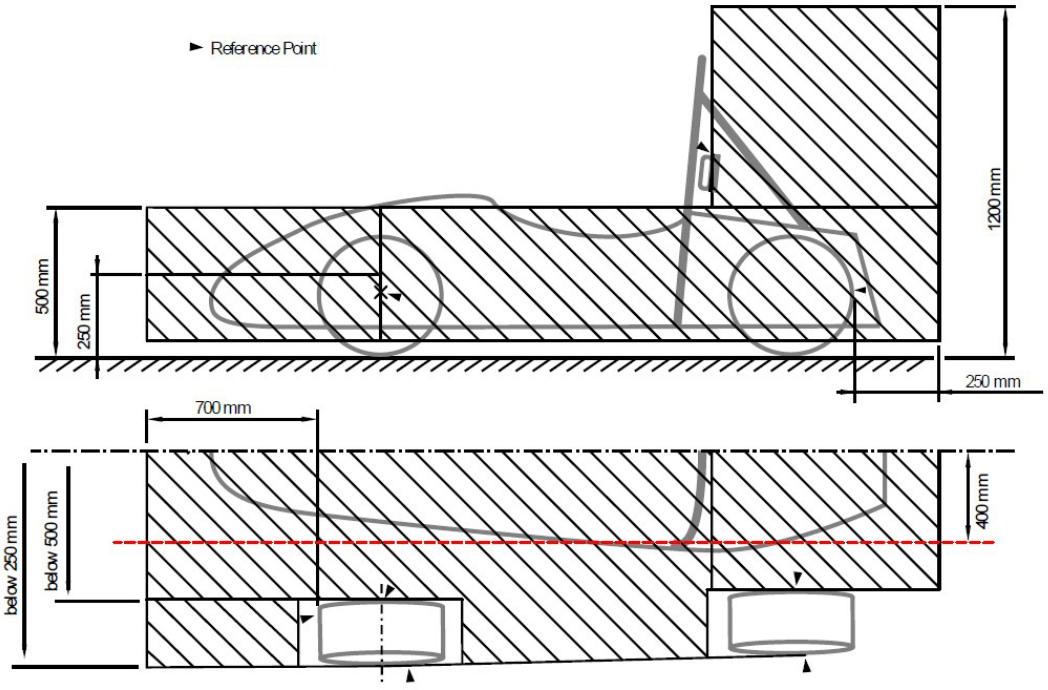

Figure 4.1 An overview of the key technical dimensions of a Formula SAE car (SAE International, 2023)

4.3 Technical Inspection (IN)

Aerodynamic Devices Stability and Strength (IN.8.2)

Continuing based on Formula SAE Regulations we will discuss about Aerodynamic Devices

Stability and Strength (SAE International, 2024, Chapter IN - Technical Inspection, Section IN.8 Mechanical Technical Inspection, Rule IN.8.2). This regulation introduces a comprehensive assessment to ensure the robustness and reliability of these crucial components. Rule IN.8.2.1 permits technical inspectors to assess Aerodynamic Devices by applying force in any direction and at any point, with the primary goal of minimizing the risk of wing detachment. In cases where significant deflection is observed, Rule IN.8.2.2 allows for the application of approximately 200 N force. Loaded deflection should not exceed 25 mm, and any permanent deflection should be less than 5 mm. Furthermore, Rule IN.8.2.3 establishes a protocol for addressing large, uncontrolled movements of Aerodynamic Devices during on-track observations. In such instances, officials may Black Flag the vehicle, initiating the process for Reinspection (IN.15), a topic to be further discussed below. These evaluations ensure the safety and stability of Aerodynamic Devices throughout the dynamic events.

Inspection Approval (IN.13.1)

As the final stage of the Technical Inspection (IN) process approaches, Inspection Approval, (SAE International, 2024, Chapter IN - Technical Inspection, Section IN.13 Inspection Approval, Rule IN.13.1), becomes a crucial milestone for Formula SAE vehicles. Following the successful completion of all aspects documented on the Technical Inspection sheet, the vehicle attains Inspection Approval, marking a significant milestone (Rule IN.13.1.1). This approval is denoted by the affixing of the completed Inspection Sticker (Rule IN.13.1.2). However, the attainment of Inspection Approval signals the vehicle's readiness for competition, contingent upon its sustained adherence to the required condition throughout the entirety of the event (Rule IN.13.1.3). It is crucial to note that the authority vested in the Organizer, Chief Technical Inspector, or a designated representative empowers them to void Inspection Approval at any time and for any reason (Rule IN.13.1.4), underscoring the ongoing vigilance and dynamic nature of the inspection process to ensure continued compliance and safety.

Reinspection (IN.15)

As an integral component of the post-approval process, Reinspection (IN.15) stands as a pivotal mechanism outlined in the Formula SAE regulations. Concerning the requirements of the Reinspection (SAE International, 2024, Chapter IN - Technical Inspection, Section IN.15 Reinspection, Rule IN.15.1) it is noted that any vehicle may be subject to Reinspection at any time and for any reason (Rule IN.15.1.1), underlining the flexibility of this process. In the event that Inspection

Approval is voided, Reinspection becomes mandatory to restore this approval (Rule IN.15.1.2). The conduct of Reinspection, (SAE International, 2024, Chapter IN - Technical Inspection, Section IN.15 Reinspection, Rule IN.15.2), is comprehensive, with the Technical Inspection process subject to repetition either in entirety or in part (Rule IN.15.2.1). Specific areas or items to be inspected are determined by the discretion of the Chief Technical Inspector (IN.15.2.2). The result of Reinspection, (SAE International, 2024, Chapter IN - Technical Inspection, Section IN.15 Reinspection, Rule IN.15.3), are two-fold. If Inspection Approval is voided, successful completion of Reinspection reinstates Inspection Approval (Rule IN.15.3.1). However, if issues are identified during Reinspection, leading to voided Inspection Approval, consequences during Dynamic Events may ensue (Rule IN.15.3.2). These consequences range from penalties, including additional time added to event(s), loss of one or more fastest runs, and, in extreme cases, disqualification, all subject to official discretion.

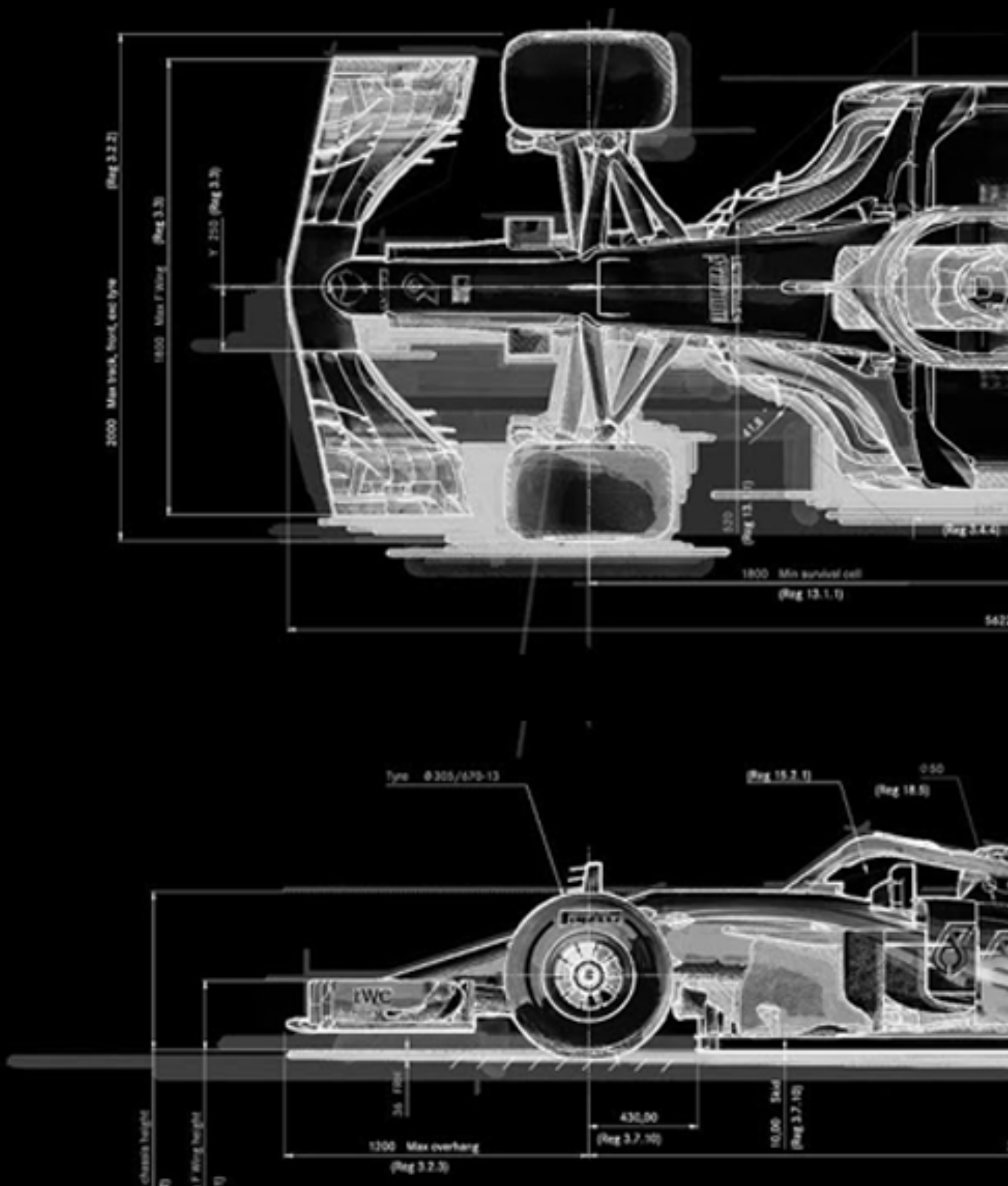

DESIGN PROCESS

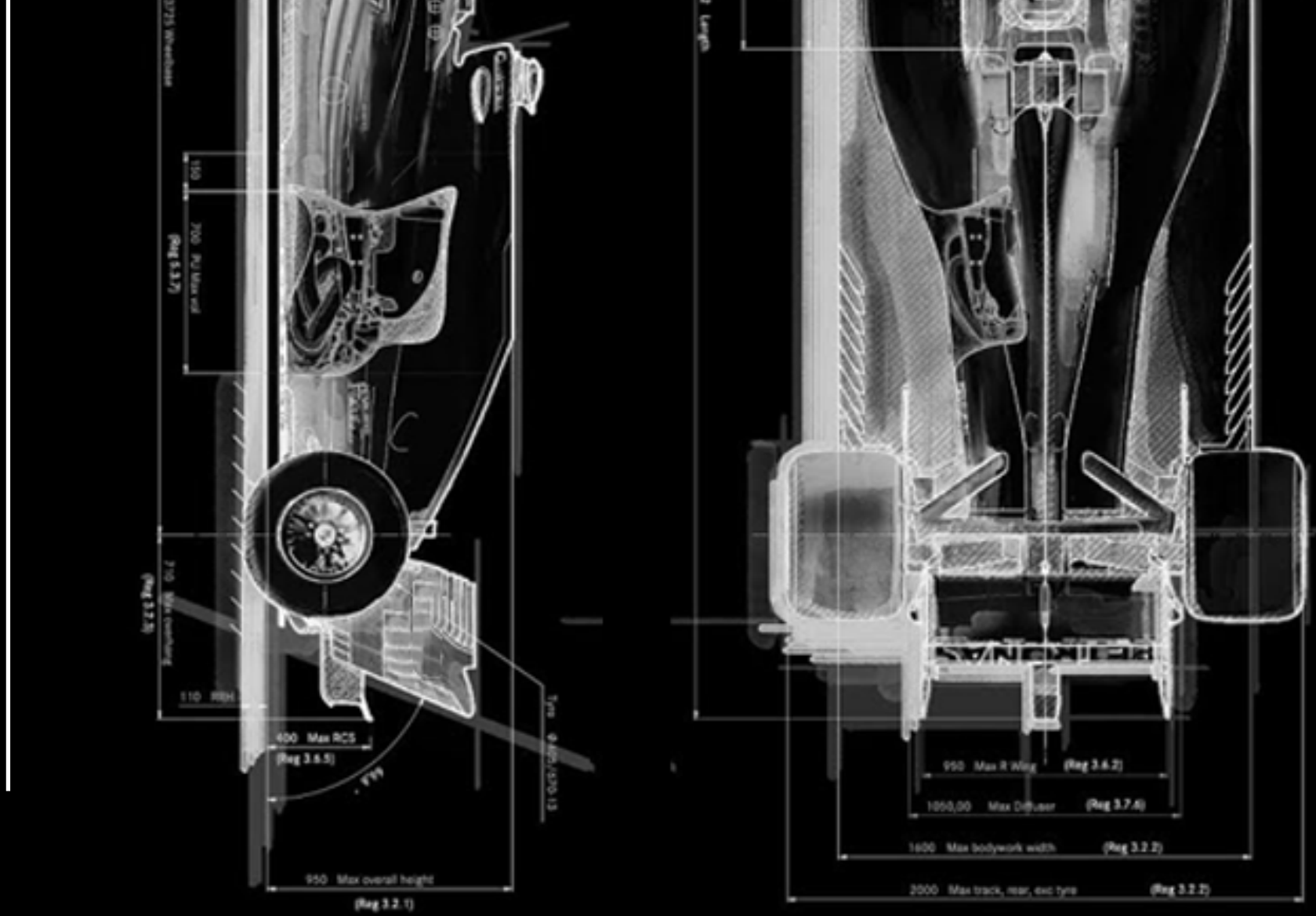
400 Max RCS
(Reg 3.6.5)
950 Max overall height
(Reg 3.2.1)
950 Max R Wing (Reg 3.6.2)
1600 Max bodywork width (Reg 3.2.2)
2000 Max track, rear, exc tyre (Reg 3.2.2)

CHAPTER 5

According to the competition rules, regulations, and technical specifications of the 2024 car from the Technical University of Crete, the front wing was designed parametrically using CATIA V5 R20 software.

5.1 Parametric Modeling

The process of parameterization in CAD models can be achieved in order to facilitate easy and rapid geometrical transformations within the model.

More specifically, parametric design involves using parameters to define and control dimensions within the model. In essence, this means that the geometry of a model is not fixed, but instead guided by a set of parameters. This flexibility and adaptability allow for efficient automation of mundane and repetitive operations, ultimately reducing lead time.

Parameters can take various forms such as Real, Integer, String, Length, Mass, etc. User-defined parameters provide immediate access to controlling the shape, size, and other characteristics of the model (Luu, 2015). This approach not only enhances the precision and customization of the design but also streamlines the design process by allowing for swift adjustments based on changing requirements or specifications.

5.1.1 Reference System

The reference system is a wireframe model that contains basic geometrical information and elements such as points, lines, and planes. Its purpose is to define and capture the core architecture of the parametric model. Within the wireframe model, 3D control points are connected by 3D curves, collectively representing the foundational structure of a model.

Both user-defined parameters and the reference system, also termed a skeleton model, serve as the pivotal modification interface between the user and the parametric model. Beyond this, the reference system embodies the various interfaces established by components with other connecting elements. Therefore, the absence of a reference system would render a substantial portion of the model's control inaccessible to the user (Luu, 2015). It is through the reference system that the user gains not only a structural understanding but also the means to efficiently manipulate and refine the parametric model in alignment with design specifications and objectives.

5.2 CATIA V5 R20

CATIA stands as a multi-platform commercial software suite encompassing CAD, CAM, CAE (Computer-aided engineering), and PLM (Product Lifecycle Management). Developed by the French company Dassault Systèmes (DS), CATIA emerged in 1977 as an in-house initiative, quickly evolving into a pivotal player in the realm of product development (Novo, 2018).

With a holistic approach, CATIA offers support throughout the entire product development life-cycle, from the initial design stage (CAD) to production (CAM) and subsequent product analysis (CAE) (Sánchez Alacid, 2009). Its widespread adoption spans diverse industries, reaching into aerospace, automotive, and beyond, making it an indispensable tool.

In 1981, CATIA took a significant step forward when it was first sold and distributed by IBM. Shortly afterward, the Boeing Company recognized its potential and chose CATIA as its main design program in 1984 (Igglezakis, 2016).

Today, with more than forty years of experience, CATIA is the world's leading solution for product design and experience. Currently used by many leading organizations in multiple industries, such as BMW, Volkswagen Group, Tesla Motors, and Airbus.

Renowned for its versatility, CATIA boasts a user-friendly interface meticulously organized into specialized workbenches, each tailored to address specific design and engineering tasks. CATIA's prowess extends across both parametric solid and surface modeling, providing users with the capability to create intricate 3D models while allowing for flexibility in design modifications. Its comprehensive capabilities span assembly design, kinematics simulation, and integrated analysis tools, positioning it as a pivotal tool in the holistic product development process.

It is essential to note that, for the purposes of this thesis, CATIA was exclusively utilized for design. Despite its consistent evolution with various versions released over the years, CATIA V5 R20 was specifically chosen for the development of this thesis.

Each task type within CATIA corresponds to a specific Workbench, signifying a designated work environment for different tasks. Each Workbench contains a tailored toolbar collection and drop-down menu specific to the tasks realized within it (Sánchez Alacid, 2009).

5.2.1 Generative Shape Design Workbench

For creating the front wing it was used one of the main CATIA modules: Generative Shape Design.

This image above illustrates the step-by-step process of accessing the Generative Shape Design workbench in CATIA V5. Starting from the CATIA V5 main menu, the user navigates to the 'Shape' category. Within this category, they locate and select the 'Generative Shape Design' option.

The CATIA-V5 Generative Shape Design Workbench is used to create advanced shapes derived from complex surfaces. This Workbench provides a plethora of possibilities to achieve the desired final model, utilizing a combination of wireframe and surface features (Jabalera López, 2010).

Listed below are some of the main toolbars used in Generative Shape Design.

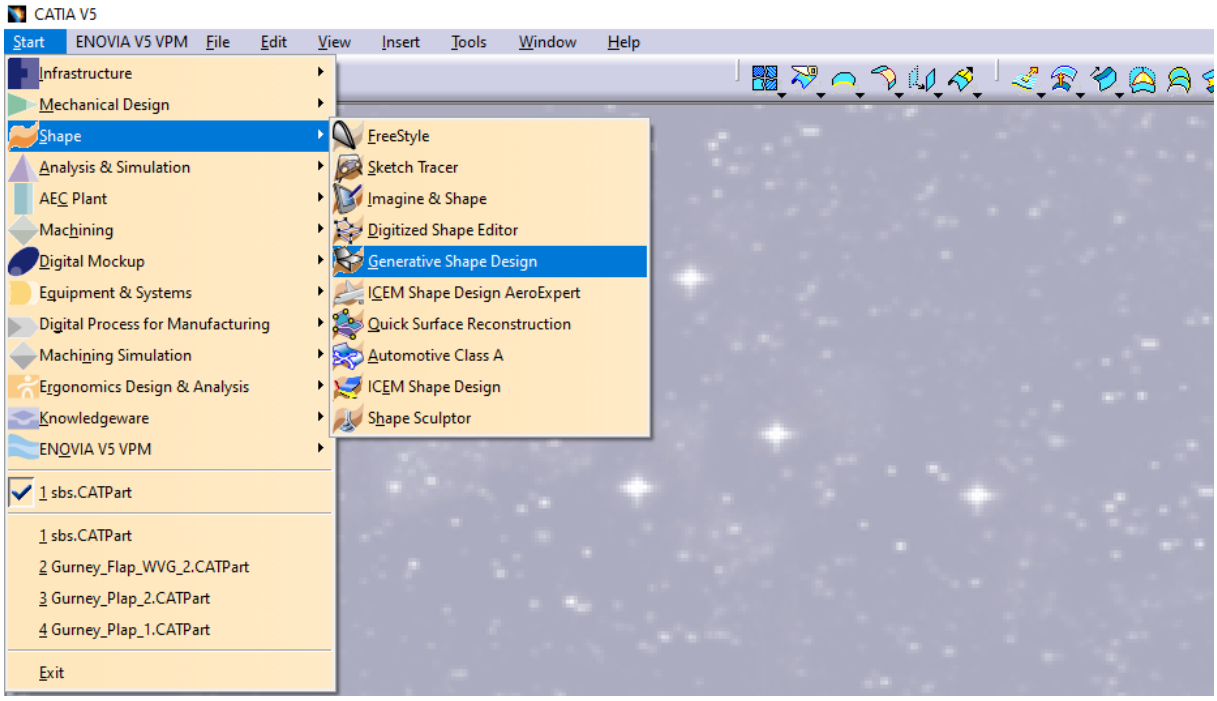

Figure 5.1 CATIA V5 R20 Start Menu.

5.2.1.1 Wireframe Toolbar

Functionality: Enables the creation of wireframe geometry, encompassing points, lines, and curves.

Features: Includes tools like point, line, plane, circle, spine, intersection, projection, and parallel curve.

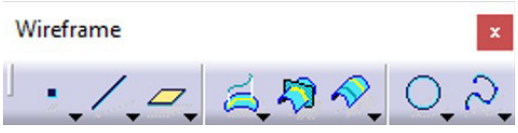

Figure 5.2 Wireframe Toolbar.

5.2.1.2 Surfaces Toolbar

Functionality: Enables users to model both simple and complex surfaces.

Features: Encompasses tools such as extrude, offset, swept, fill, multisections, and blend, providing a diverse array of surface modeling options.

Figure 5.3 Surface Toolbar.

5.2.1.3 Operations Toolbar

Functionality: Enables users to modify existing wireframes or surfaces.

Features: Encompasses tools like join, split, trim, boundaries, edge fillet, translate, or extrapolate.

Figure 5.4 Operations Toolbar.

5.2.1.4 Volumes Toolbar

Functionality: Enables users to create and manipulate 3D volumes.

Features: Includes functions such as volume extrude, thick surface, and close surface, as well as, adding, removing, and intersecting volumes.

Figure 5.5 Volumes Toolbar.

5.2.1.5 Knowledge Toolbar

To initiate the creation and modification of parameters, employ the Formula feature located in the Knowledge toolbar within CATIA's Generative Surface Design workbench.

Figure 5.6 Knowledge Toolbar.

Formulas in CATIA serve as relations employed to define or constrain parameters. A formula is established in CATIA by linking a user-defined parameter to a specific feature, establishing a connection between the parameter and the feature for enhanced control and adaptability in the design process.

5.3 Creating the CAD Model

The CAD model goes through four stages during the modeling process, from start to finish. These stages include:

- Defining Parameters: This initial stage involves defining and configuring the parameters that govern various dimensions and characteristics of the model.
- Wireframe Model: This represents the reference system and the underlying skeleton in the geometry.
- Surface Model: This builds upon the wireframe model to create a more detailed representation of the object's surfaces.
- Solid Model: This is the final stage where the CAD model is fully solidified.

Each stage contributes to the overall development of the CAD model.

5.3.1 Defining Parameters

The parameters used to design the wing are displayed in the table below.

Parameter	Unit	Desrcription
Wing Span	Length (mm)	Width (opening) of the Wing
Section 1 Chord	Ratio (%)	Chord Length for Section 1
Section 2 Chord	Ratio (%)	Chord Length for Section 2
Section 3 Chord	Ratio (%)	Chord Length for Section 3
Section 4 Chord	Ratio (%)	Chord Length for Section 4
AoA 1	Angle (deg)	Angle of Attack for Section 1
AoA 2	Angle (deg)	Angle of Attack for Section 2
AoA 3	Angle (deg)	Angle of Attack for Section 3

AoA 4	Angle (deg)	Angle of Attack for Section 4
Section 2 Wing Span Ratio	Ratio (%)	The Span of the Wing where Section 2 is located
Section 3 Wing Span Ratio	Ratio (%)	The Span of the Wing where Section 3 is located
Airfoils Z-Axis Distance	Length (mm)	The vertical distance between the first and second wing
Airfoils X-Axis Distance	Length (mm)	The horizontal distance between the first and second wing
Section 5 Chord	Ratio (%)	Chord Length for Section 5
Section 6 Chord	Ratio (%)	Chord Length for Section 6
Section 7 Chord	Ratio (%)	Chord Length for Section 7
Section 8 Chord	Ratio (%)	Chord Length for Section 8
AoA 5	Angle (deg)	Angle of Attack for Section 5
AoA 6	Angle (deg)	Angle of Attack for Section 6
AoA 7	Angle (deg)	Angle of Attack for Section 7
AoA 8	Angle (deg)	Angle of Attack for Section 8
Endplate Corners	Length (mm)	The Radius of the Corners of the Endplate
Endplate Height	Length (mm)	The Height of the Endplate
Endplate Length	Length (mm)	The Length of the Endplate
Endplate Angle 1	Angle (deg)	The Angle Between the Upper and Lower Sides of the Endplate.
Endplate Angle 2	Angle (deg)	The Angle between the Lower Side and the Front Side of the Endplate.
Endplate Width	Length (mm)	The Width of the Endplate
Endplate Fillet	Length (mm)	The Radius of the Fillet on the Perimeter of the Endplate
FD Width	Length (mm)	The Flow Domain Width
FD Height	Length (mm)	The Flow Domain Height
FD Length	Length (mm)	The Flow Domain Length
FD X-Axis Distance	Length (mm)	The Point on the X-axis, inside the Flow Domain, where the Final Assembly is placed.
FD Z-Axis Distance	Length (mm)	The Point on the Z-axis, inside the Flow Domain, where the Final Assembly is placed.

The parameters can be defined using the Formula feature in the Knowledge toolbar, as mentioned before.

5.3.2 Wireframe Model

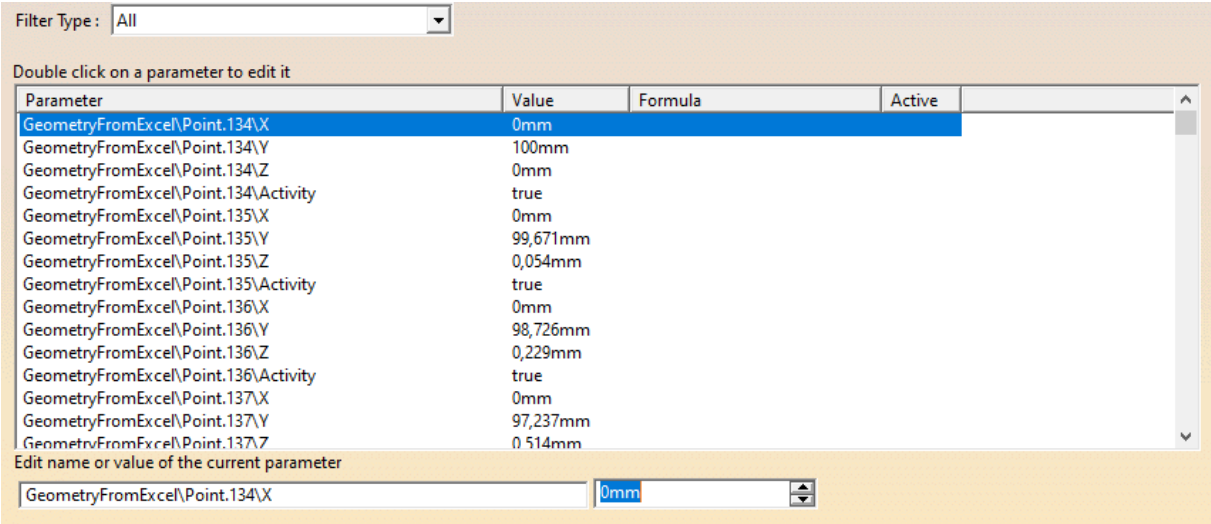

Figure 5.7 Parameters edit window.

First, a line representing the wing span was drawn, using the **Line** command*).* Then, four points were parametrically placed on it, using the **Point** command *(Figure 5.8)* The corresponding planes were then generated by executing the **Plane** command *(Figure 5.9).* Notably, all of these commands can be found within the Wireframe Toolbar.

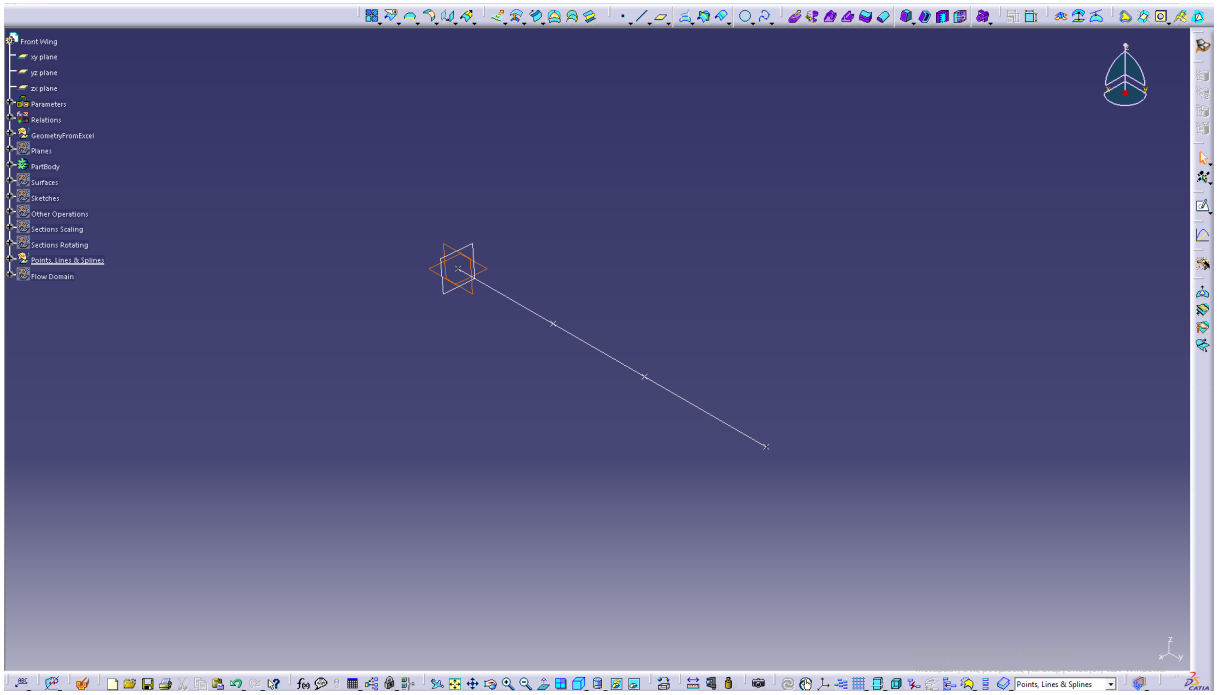

Figure 5.8 Line and Points creation.

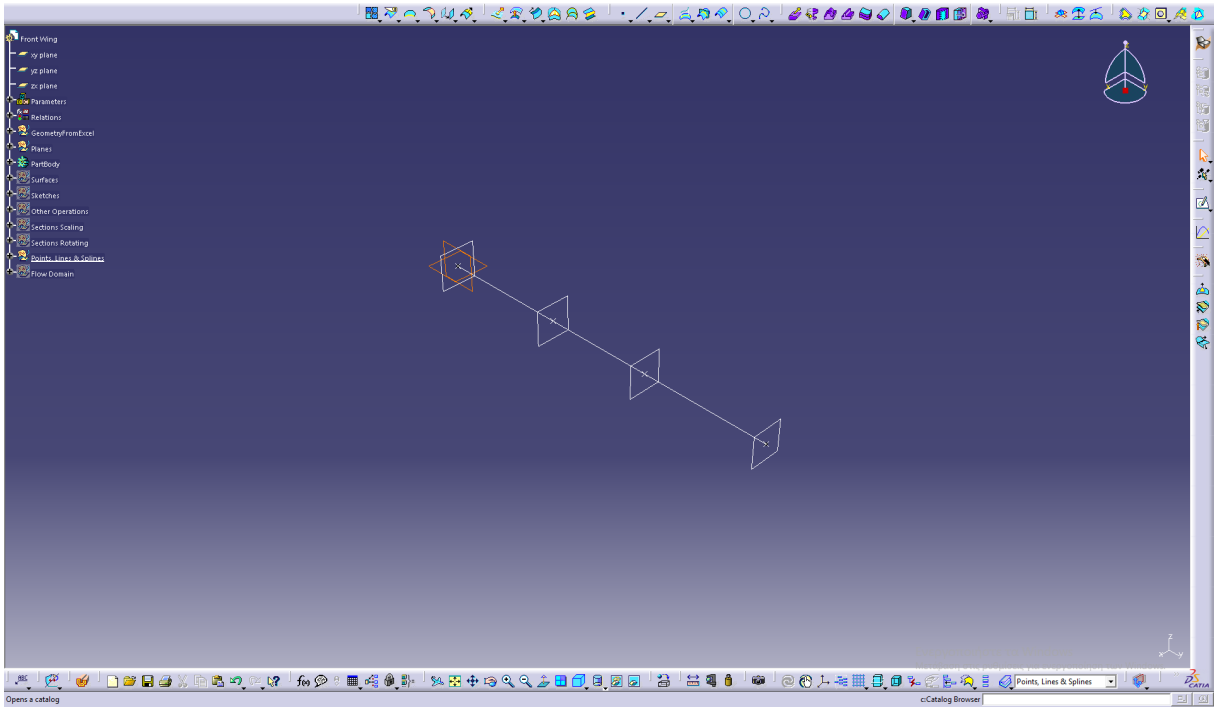

Figure 5.9 Planes creation.

A point was then placed on each plane using the **Point** command from the Wireframe Toolbar *(Figure 5.10).*

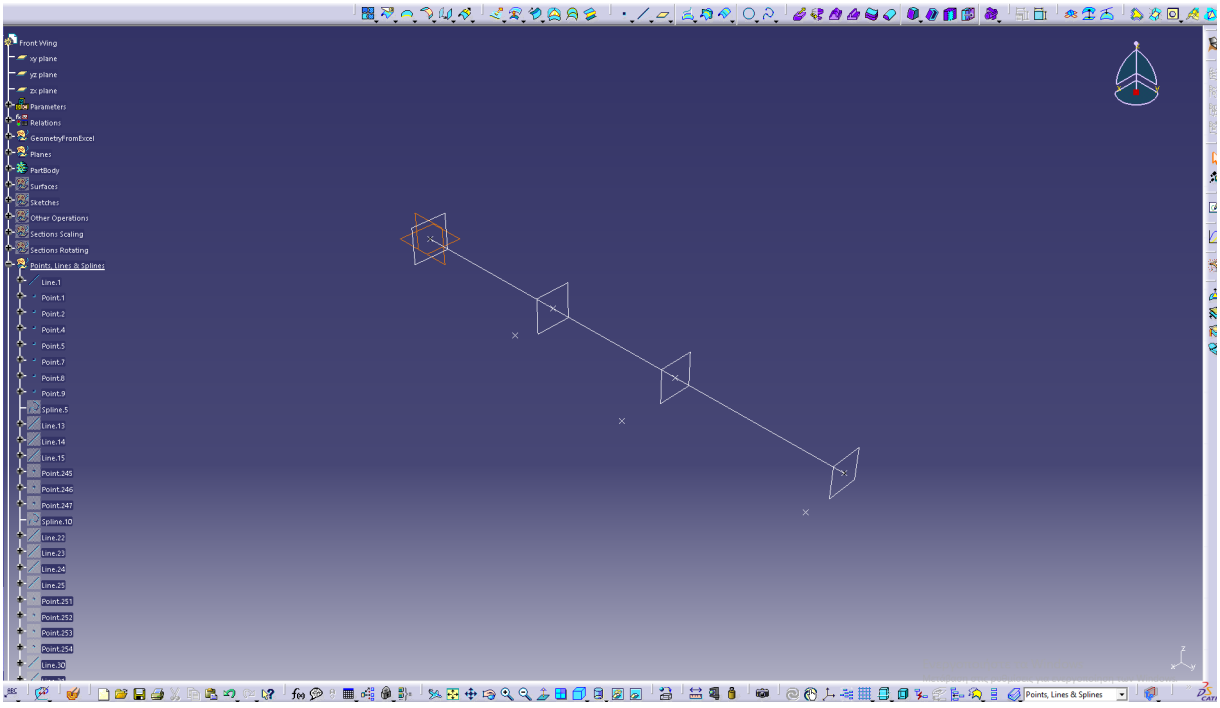

Figure 5.10 Point placement on the planes.

Then, a spline was created through these four points, using the **Spline** command in the Wireframe Toolbar *(Figure 5.11).* This complex structure set the groundwork for the subsequent placement of distinct airfoils on each designated point.

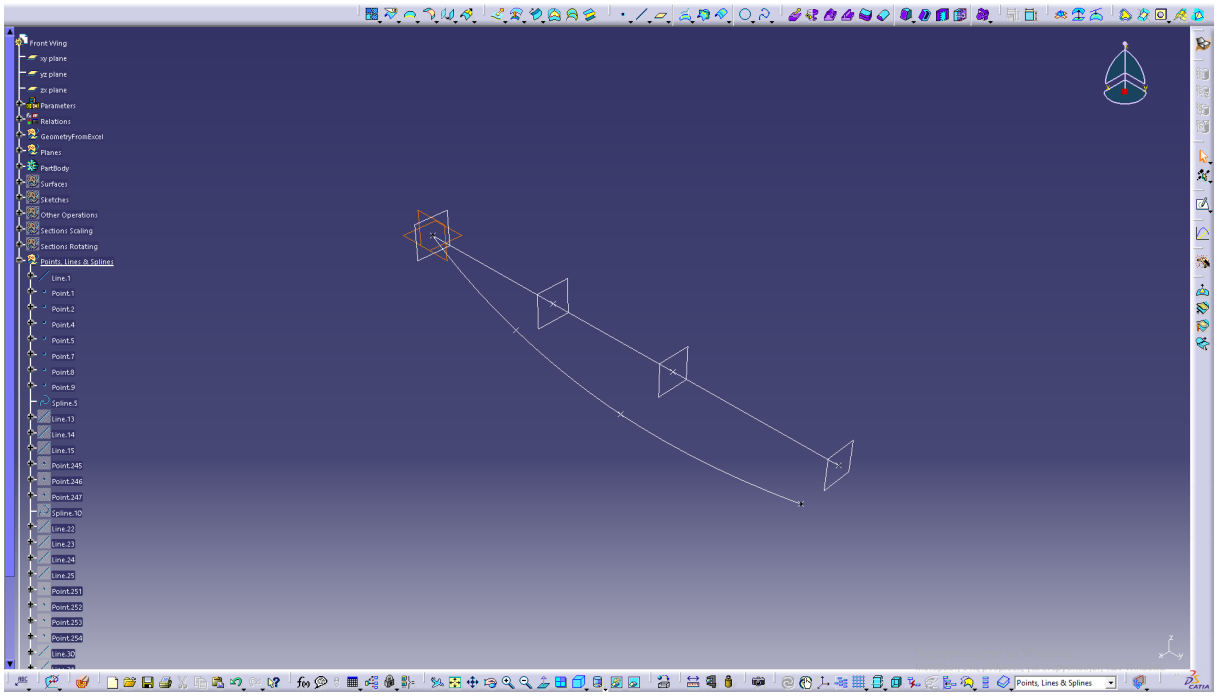

Figure 5.11 Spline creation.

In order to create the airfoil geometry in CATIA, Microsoft Excel played a crucial role. Specifically, the geometry of the RG15 airfoil was imported onto the initial plane utilizing the "GSD_PointSplineLoftFromExcel" file in Microsoft Excel *(Figure 5.12).* Through this file, both the points and the connecting spline are imported, effectively constructing the airfoil geometry within CATIA.

Embedded with active Macros, this file imports the coordinates of the entered points into CATIA, with the appropriate configuration. Users can input data in various formats, such as simple points, points interconnected by a spline, or points joined by multiple splines forming a surface *(Figure 5.13).*

Note: For the successful importation of points from a Microsoft Excel spreadsheet, the template

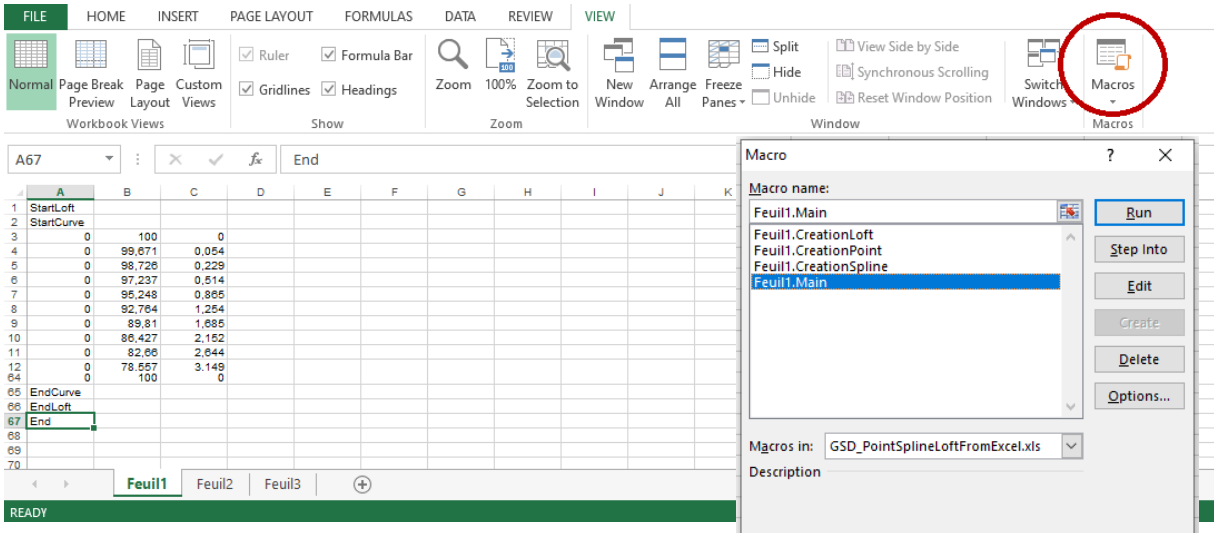

Figure 5.12 "GSD_PointSplineLoftFromExcel" file.

Figure 5.13 Macros window.

file “GSD_PointSplineLoftFromExcel” must be duplicated from the software installation folder on the computer and stored in an alternative location.

Returning to the CATIA environment we verify the successful import of the geometry *(Figure 5.14).*

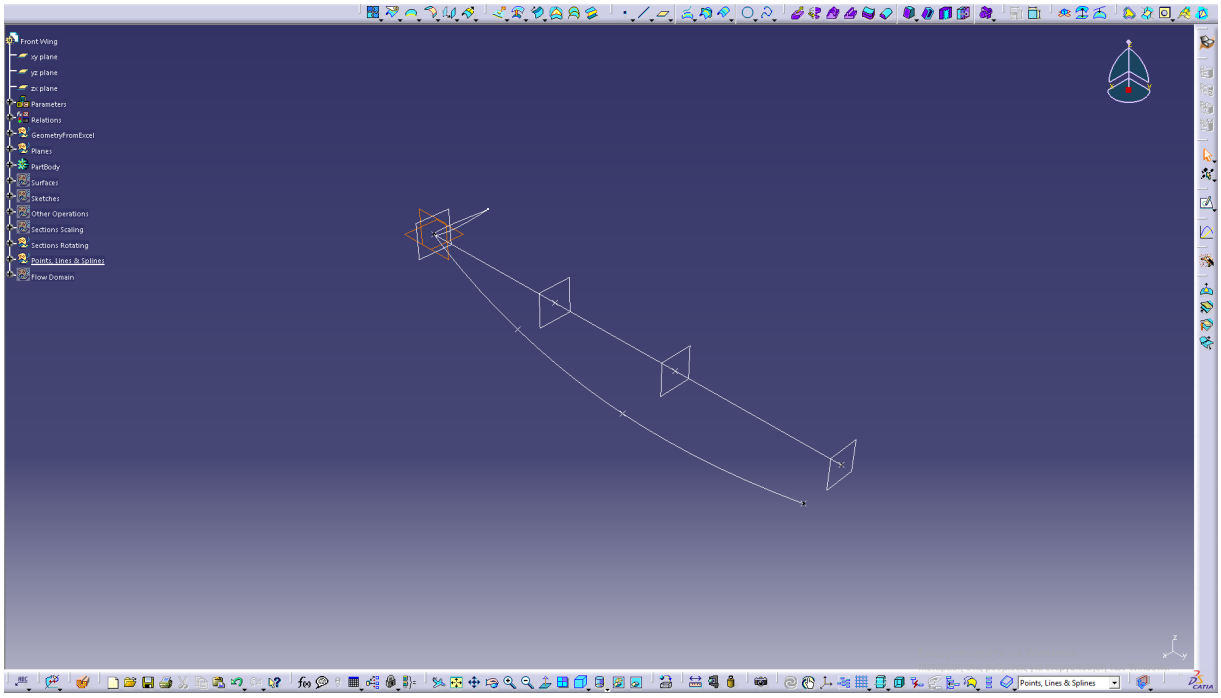

Figure 5.14 Successfully imported geometry on the first plane.

Subsequently, employing the **Translate** command from the Operations Toolbar, the airfoil was replicated onto the additional planes *(Figure 5.15).*

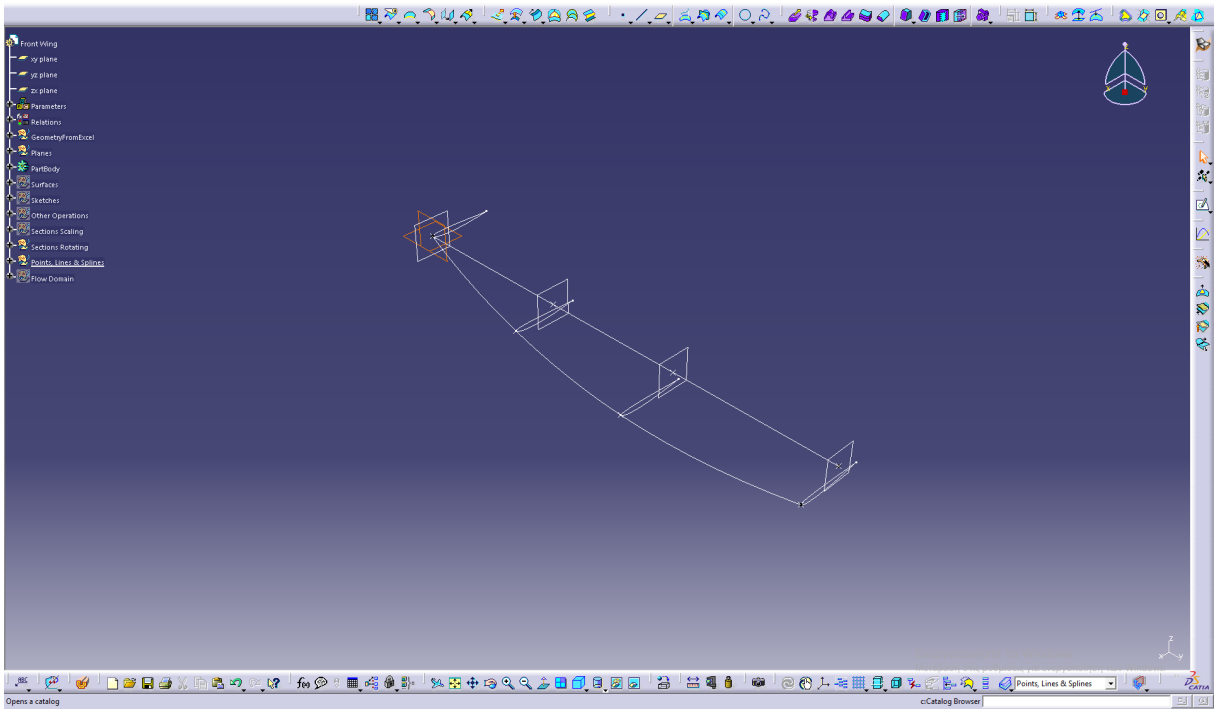

Figure 5.15 RG15 airfoil replicated onto the planes.

Afterwards, the chord size of each wing was parametrically regulated using the **Scaling** command found in the Operations Toolbar *(Figure 5.16).*

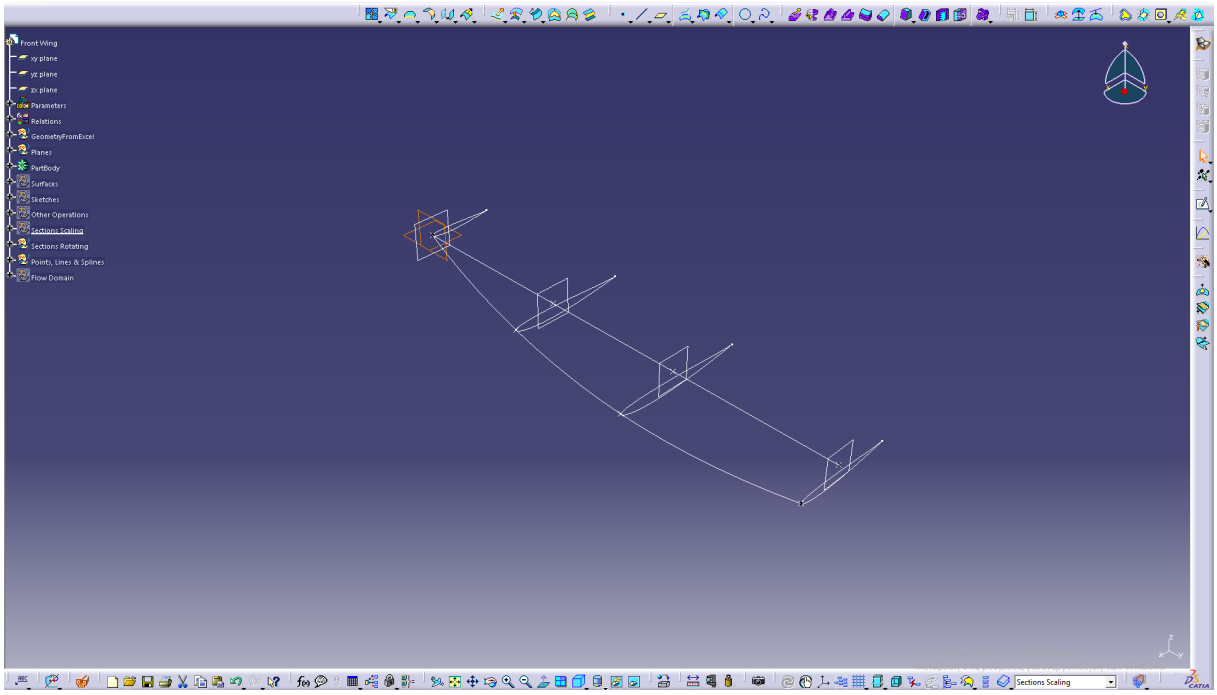

Figure 5.16 Airfoils on each plane scaled parametrically.

Continuing the process, the **Rotate** command, also accessible from the Operations Toolbar, was used for the parametric control of the angle of attack for each wing *(Fig.5.17)*.

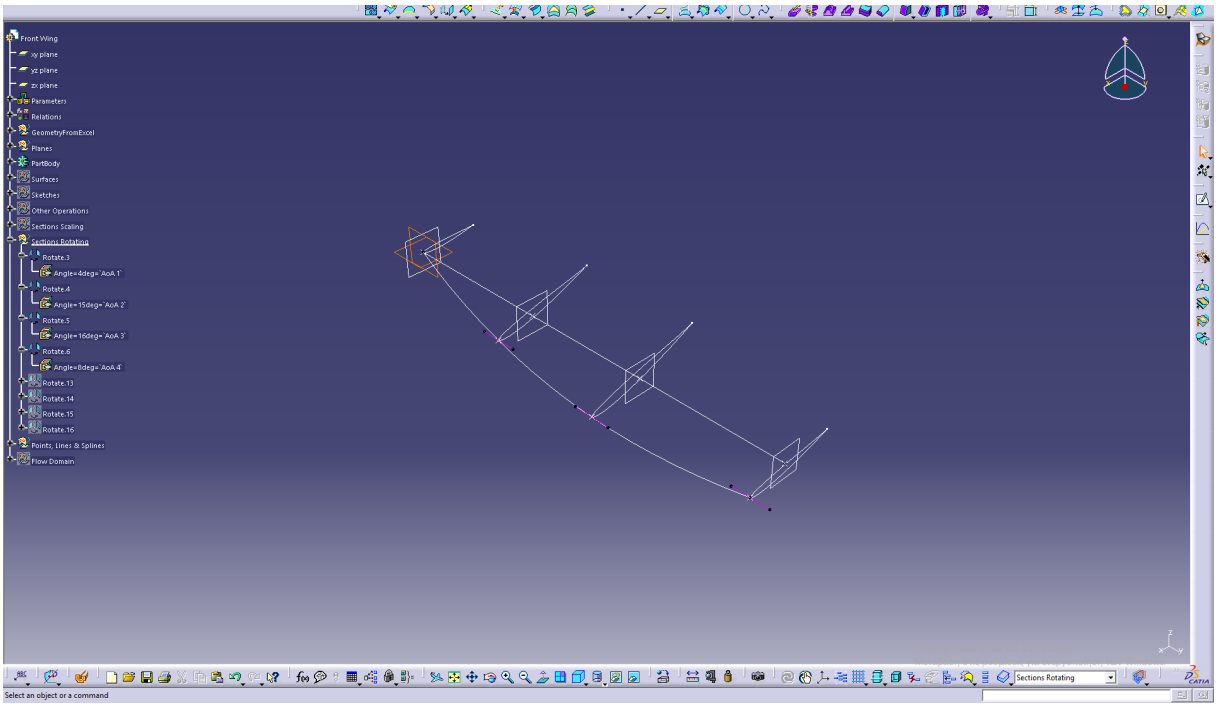

Figure 5.17 Airfoils on each plane rotated parametrically.

Following that, a new set of points and a spline were generated on the existing planes, utilizing the **Point** and **Spline** commands from the Wireframe Toolbar, thereby forming the representation of the second layer of airfoils *(Figure 5.18).*

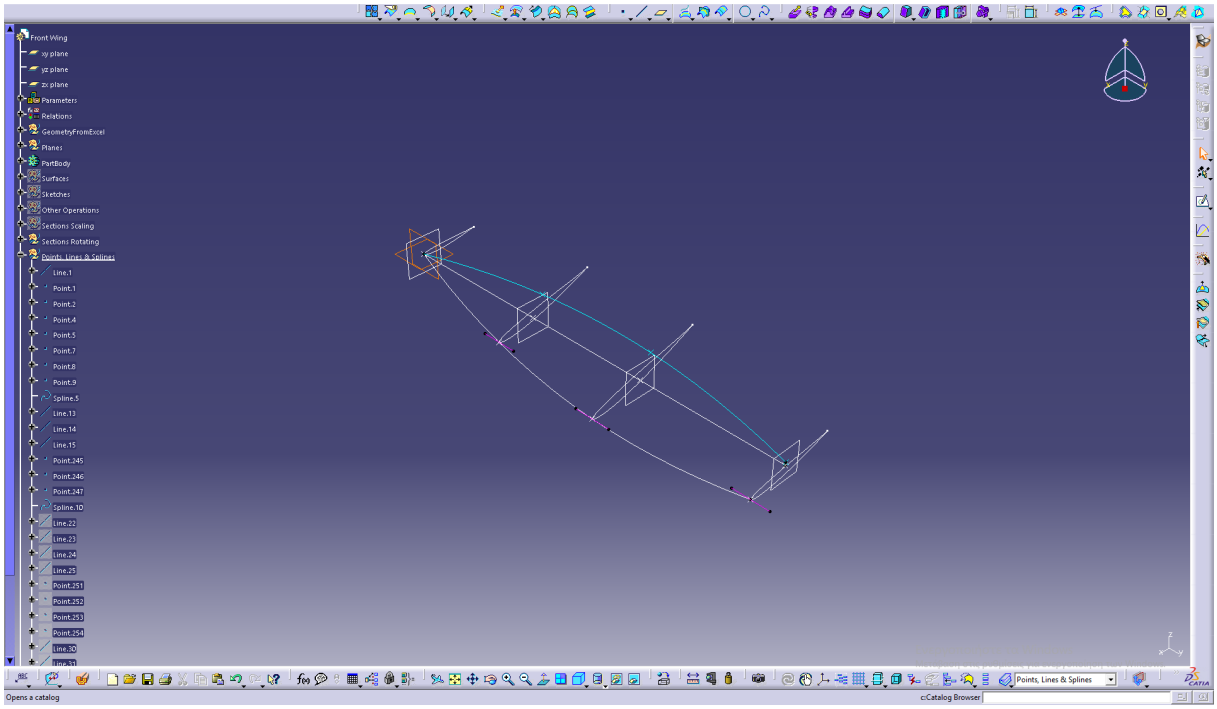

Figure 5.18 Generation of a new set of points on each plane followed by spline creation.

This second spline underwent parametric translation twice, adjusting positions on both the Z-axis and the X-axis, through the **Translate** operation in the Operations Toolbar *(Figure 5.19).*

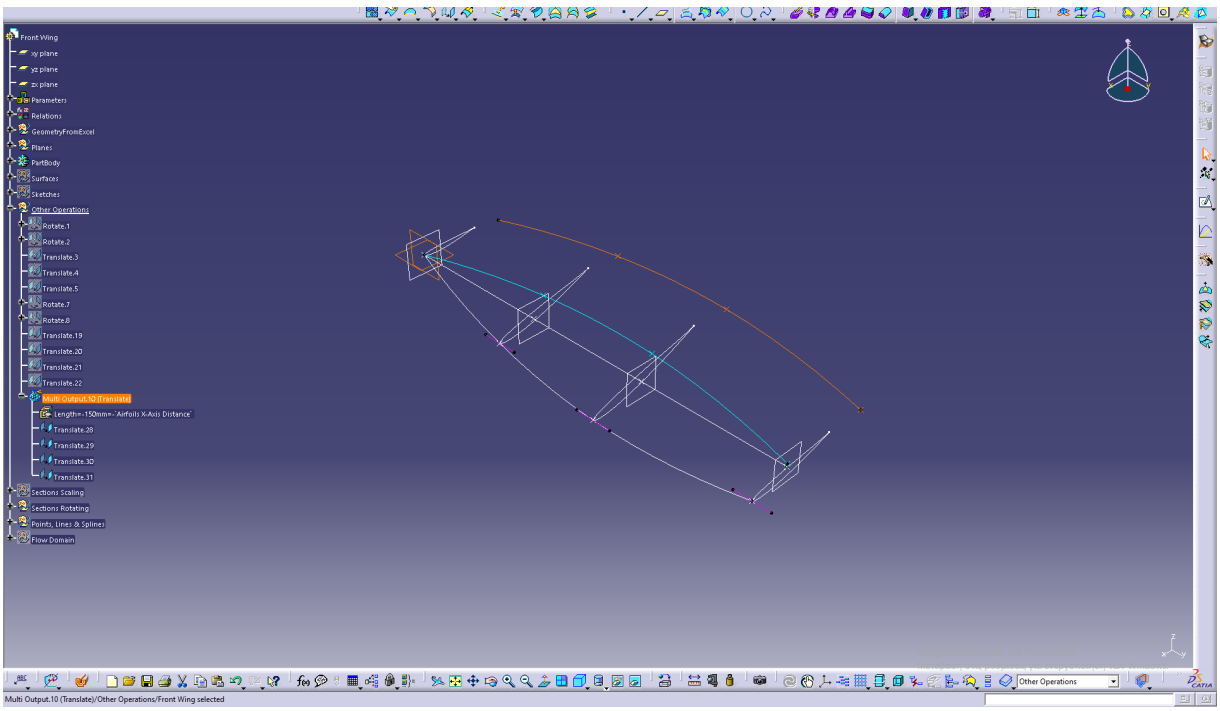

Figure 5.19 Spline translation along the X and Z axes.

On this second spline, mirroring the previous process, the NACA 4412 airfoil was imported using Microsoft Excel and replicated to all planes through the **Translate** operation from the Operations Toolbar. Likewise, the **Scaling** and **Rotate** commands, also from the Operations Toolbar, were employed to parametrically adjust their chord size and angle of attack, respectively *(Figure 5.20).*

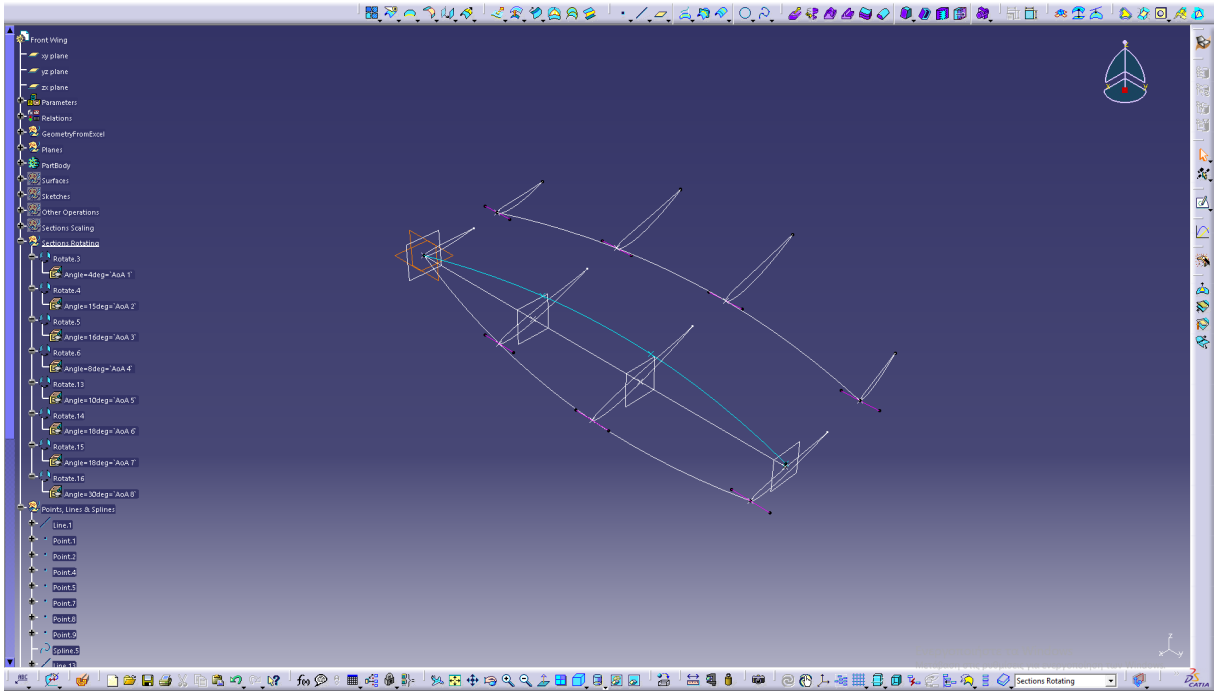

Figure 5.20 Generation of the second layer of airfoils.

Following that, the endplate of the wing was designed using the **Sketch** function, the dimensions of which are also set parametrically *(Figure 5.21).*

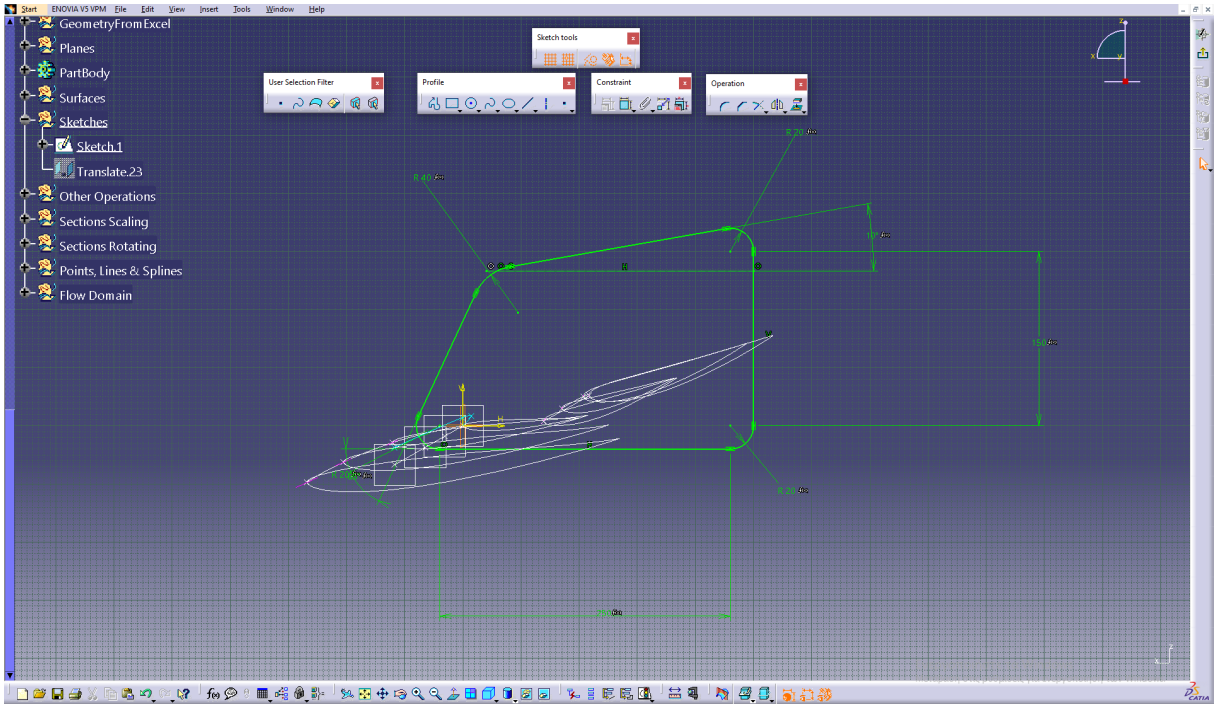

Figure 5.21 Endplate sketch.

Thus, the wireframe model is completed *(Figure 5.22)*.

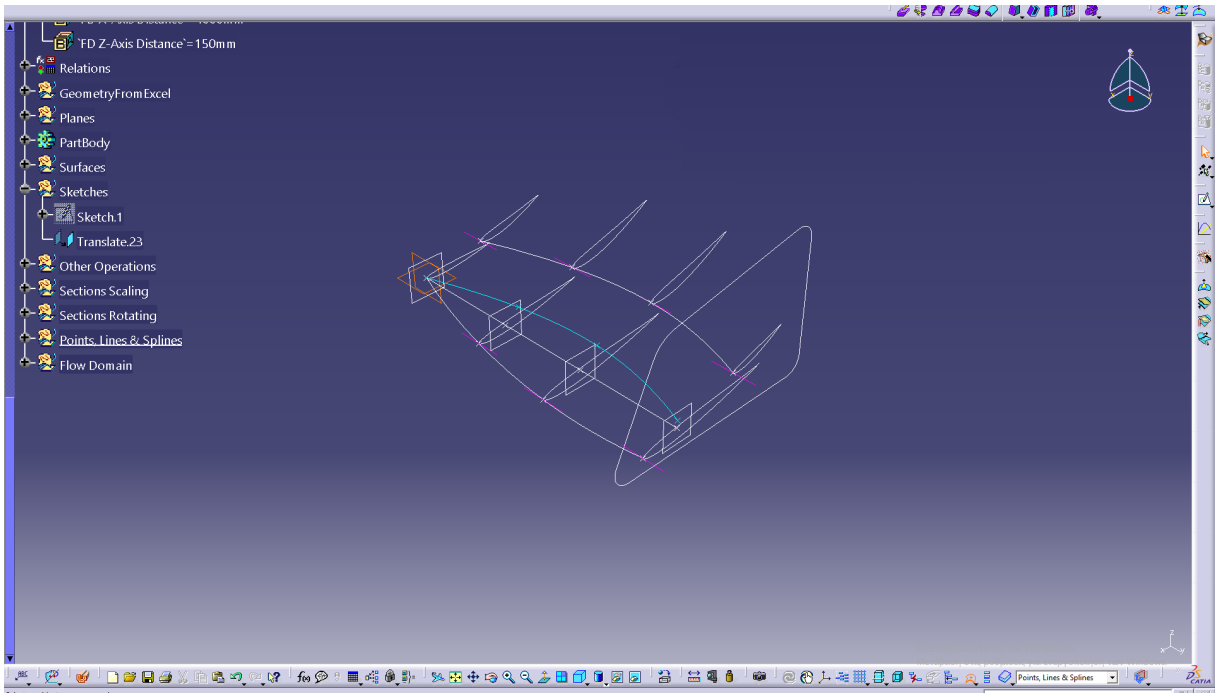

Figure 5.22 Wireframe model.

5.3.3 Surface Model

Next, the Surface model was developed *(Figure 5.23)*. Utilizing the Surfaces Toolbar and building upon the wireframe model, a detailed depiction of the model's surfaces was crafted. The **Multi-sections Surface** and **Fill** commands were employed to fashion the wing and endplate surfaces respectively.

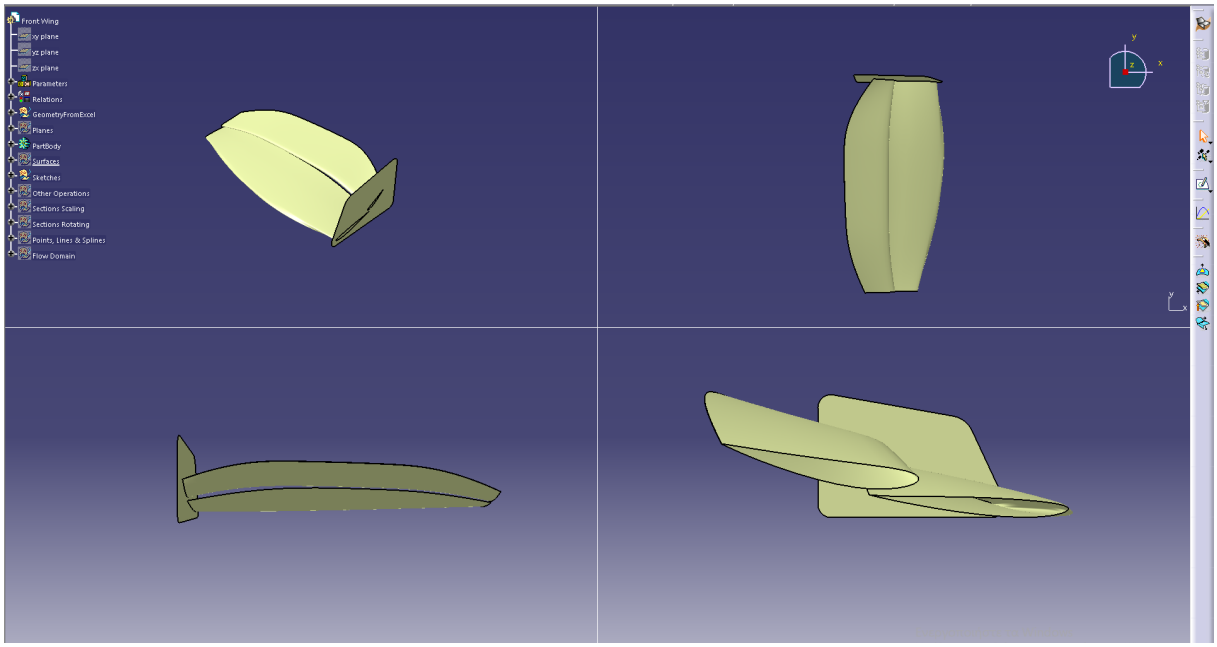

Figure 5.23 Surface model.

5.3.4 Solid Model

Following that, the Volumes Toolbar was utilized, particularly employing the **Close Surface** and **Volume Extrude** commands to completely solidify the wing and endplate respectively. Furthermore, the **Edge Fillet** command from the Operations Toolbar was applied to smooth the edges of the endplate *(Figure 5.24).*

In order to unite the three elements (the two wings and the endplate) the **Add** command from the Volumes Toolbar was employed.

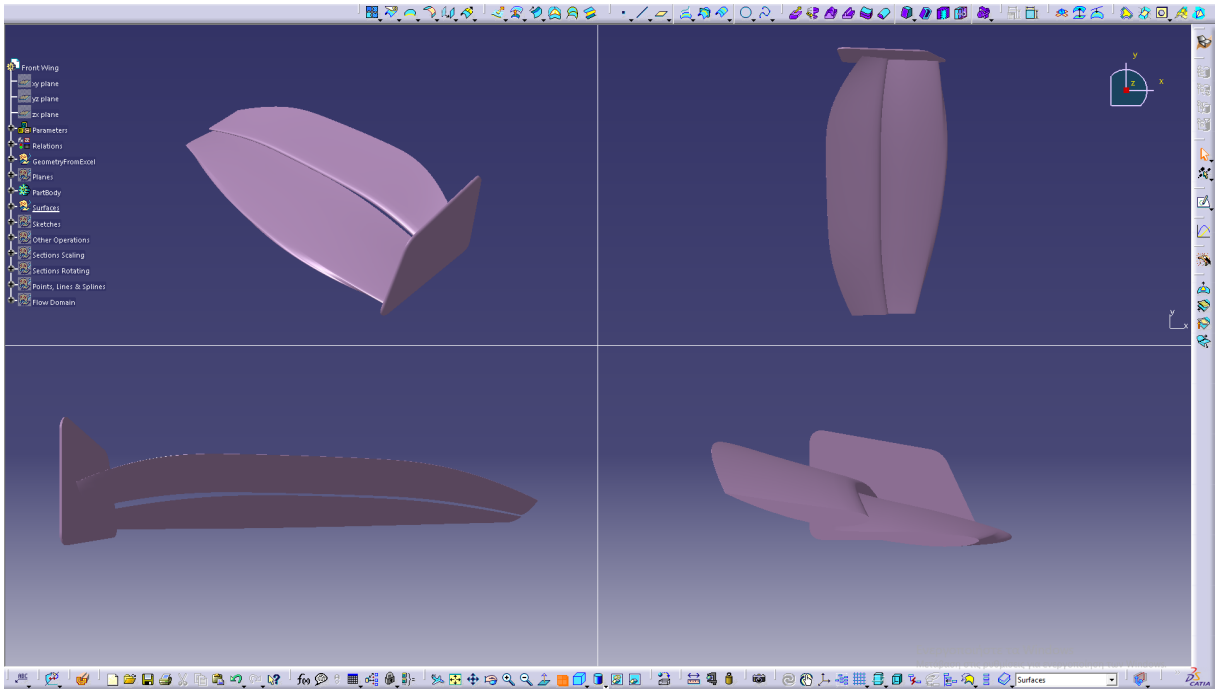

Figure 5.24 Solid model.

After configuring the desired parameter values, the final model form is depicted in Figure 5.25.

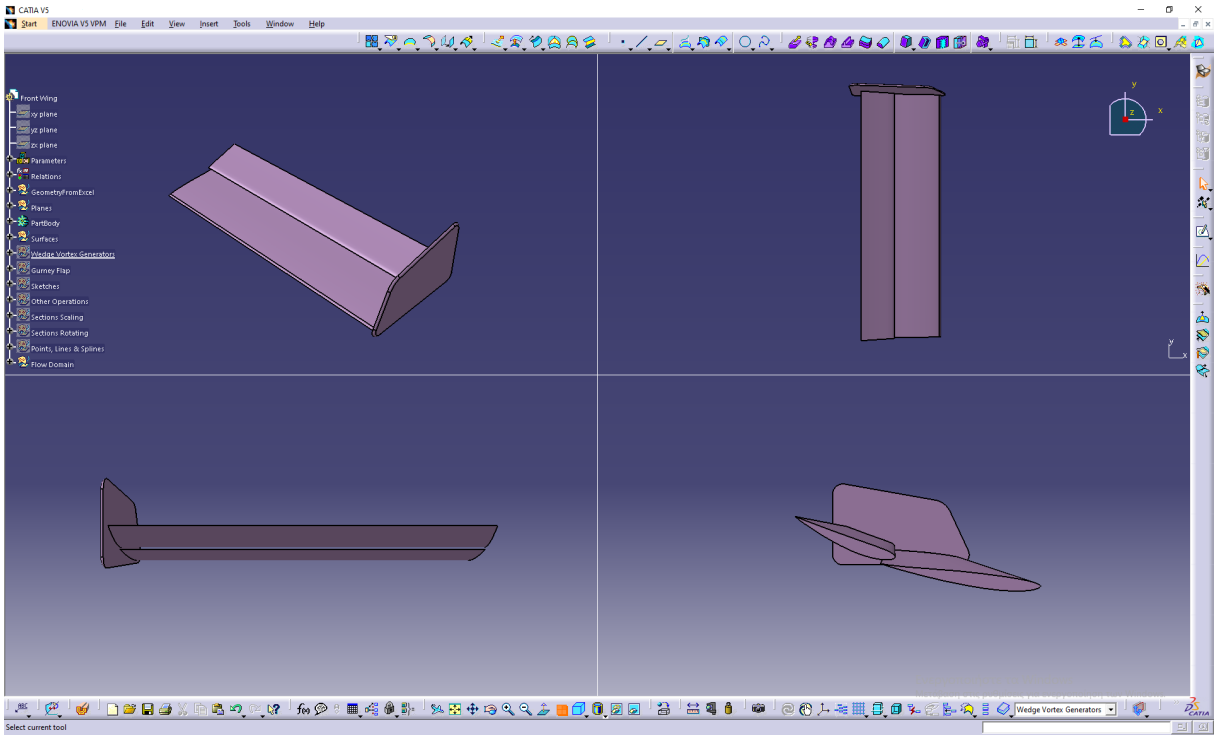

Figure 5.25 Final version of the model.

5.4 Creating the Flow Domain

The final phase in the design process involves establishing the Flow Domain, also known as the Fluid Domain. This domain is essential for conducting Computational Fluid Dynamics (CFD) simulations and forms a crucial component of the analysis.

In the realm of external aerodynamics, the Fluid Domain typically takes the shape of a rectangular box, simulating a virtual wind tunnel. Within this domain, the object of interest, such as a vehicle body or part, is positioned. It's imperative to maintain adequate spacing between the inlet, the geometry, and the outlet to ensure that boundary conditions align with the part's geometry. This spatial arrangement prevents downstream vortices from interfering with upstream solutions and ensures that pressure at the stagnation point evolves naturally (Oxyzoglou, 2017).

In CATIA, the Flow Domain was first designed using the **Sketch** command *(Figure 5.26),* and then it was solidified using the **Volume Extrude** command, from the Volumes Toolbar.

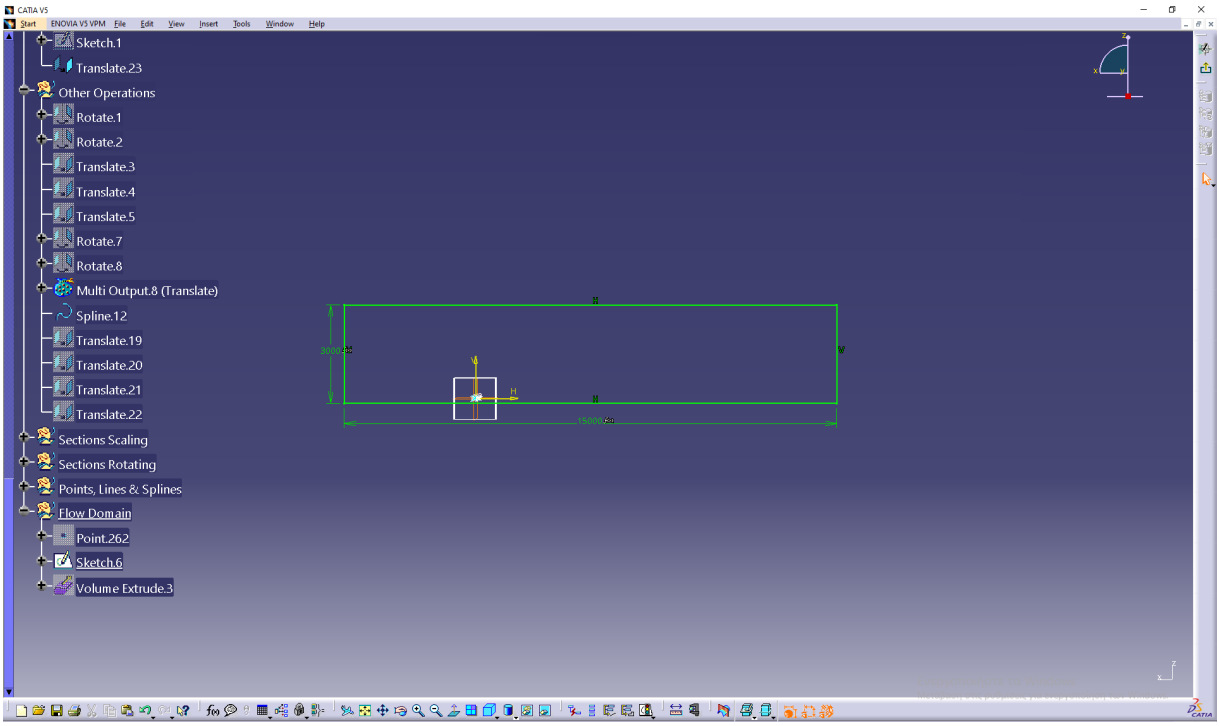

Figure 5.26 Flow Domain sketch.

Finally, using the **Remove**  command from the Volumes toolbar, the volume of the model was removed from the volume of the rectangular parallelepiped (Flow Domain). The remaining volume is the volume of the fluid around the model of the wing studied in the next stage of the project *(Figure 5.27).* Subsequent processing of the file requires saving it as an STP file. At this stage, the design of the model is completed.

Note: The positioning of the airfoil within the flow domain is also controlled parametrically.

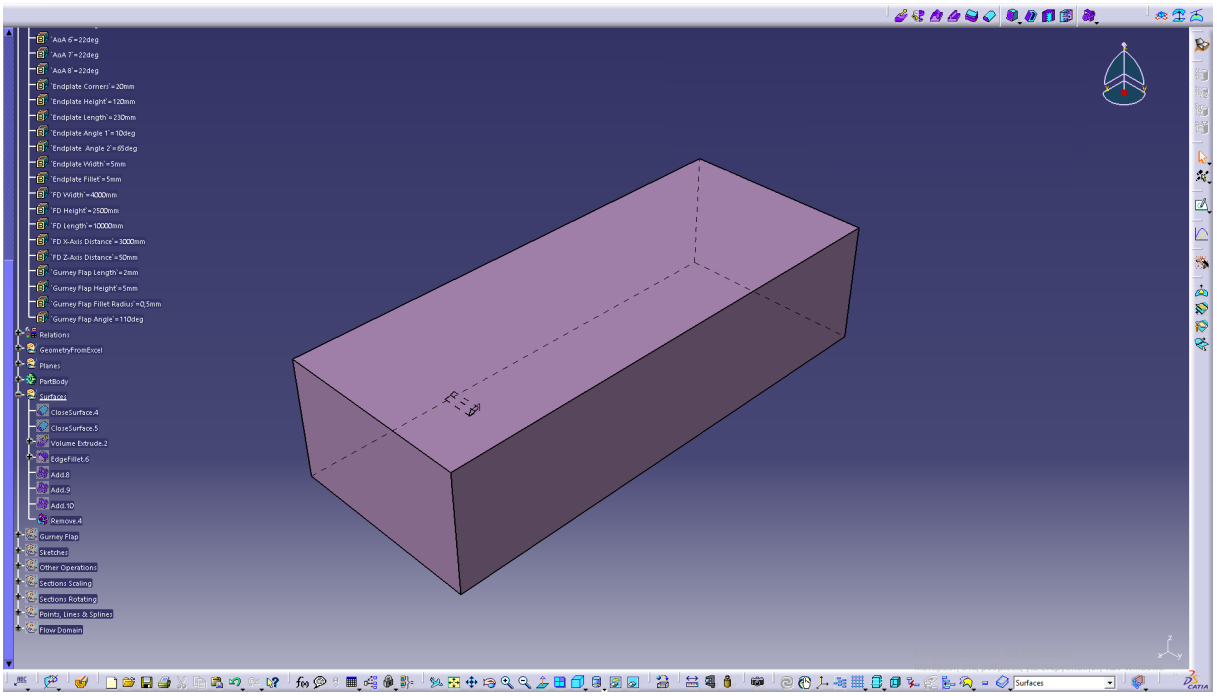

Figure 5.27 Complete stage of the flow domain.


CFX-Solver Manager
File Edit Workspace Tools Monitors Help
Workspace
Run CFX with mesh 001
Momentum and Mass
Heat Transfer
Turbulence (KO)
Wall and Boundary Scale
User Points
Out File
OUTER LOOP ITERATION = 163
Equation | Rate
U-Mom | 1.02
V-Mom | 1.01
W-Mom | 1.01
p-Mass | 0.90
H-Energy | 0.98
K-TurbKE | 1.02
O-TurbFreq | 1.01
OUTER LOOP ITERATION = 164
Equation | Rate
U-Mom | 1.02
V-Mom | 1.03
W-Mom | 1.00
p-Mass | 1.09
H-Energy | 1.04
K-TurbKE | 0.98
O-TurbFreq | 1.01
OUTER LOOP ITERATION = 165
Equation | Rate
U-Mom | 1.02
V-Mom | 1.01
W-Mom | 1.00
p-Mass | 1.12
1.0e+00
1.0e-01
1.0e-02
1.0e-03
1.0e-04
1.0e-05
1.0e-06
Variable Value
0
50
100
150
Accumulated Time Step
RMS P-Mass
RMS U-Mom
RMS V-Mom
RMS W-Mom
Running

CHAPTER 6

CFD SIMULATION RESULTS ANALYSIS

In this chapter the analysis of the simulations performed using the ANSYS 2019 R2 CFX software will be presented.

6.1 ANSYS CFX

Ansys CFX is a leading CFD software, developed by Ansys Inc, well-regarded for its application in turbo-machinery. It is known for streamlining development time with efficient workflows, advanced physics modeling capabilities, and accurate results, making it the gold standard in CFD software. Using Ansys CFX, engineers can perform key computations with minimal turnaround time.

This saved time paves the way for further simulations, fostering comprehensive product optimization. The advanced physics modeling capabilities of Ansys CFX equip engineers to take on intricate challenges within turbo-machinery applications. This reliable and precise software has undergone extensive validation. Its streamlined turbo setups and blade design tool integration save valuable time, redirecting focus to design optimization.

Whether it is blade design optimization, aeromechanics, turbulence modeling, or advanced material modeling, CFX stands as a dependable tool that delivers both time and cost efficiencies (Ansys, 2024).

6.2 Results Analysis

Incompressible, isothermal flow of air at 25 degrees Celsius was considered. The simulation was performed with an inlet flow velocity of 36 m/s and 10% turbulence intensity. The same slip velocity of 36 m/s was applied to the ground-wall, in order to simulate the relative motion of the vehicle with respect to the ground. 1 bar static pressure was imposed at the exit plane of the flow domain. A symmetry condition was also applied at the corresponding face of the flow domain. The upper and side walls of the flow domain were simulated as free-slip walls. High-resolution spatial discretization schemes were used for both flow and turbulence equations. Conservative auto timescale with a factor equal to 0.7 was used for time integration.

The first model simulated was the front wing, as designed in Chapter 5, “Design Process”, and depicted in Figure 5.25. Due to flow unsteadiness, the simulation was interrupted in order to optimize the previous design. This led to the remodeling of the front wing. This was repeated twice resulting in two new models being simulated.

6.2.1 Double Airfoil Front Wing with Gurney Flap - Model 2

In this first remodeling a Gurney flap was added to the last element of the wing. The parameters used to create the Gurney Flap are displayed in the table below. The final version of the second model is shown in Figure 6.1.

Parameter	Unit	Desrcription
Gurney Flap Length	Length (mm)	The Length of the Gurney Flap
Gurney Flap Height	Length (mm)	The Height of the Gurney Flap
Gurney Flap Fillet Radius	Lenght (mm)	The Radius of the Gurney Flap
Gurney Flap Angle	Angle (deg)	The Angle of the Gurney Flap

Table 2 - Parameters used in model 2.

Results

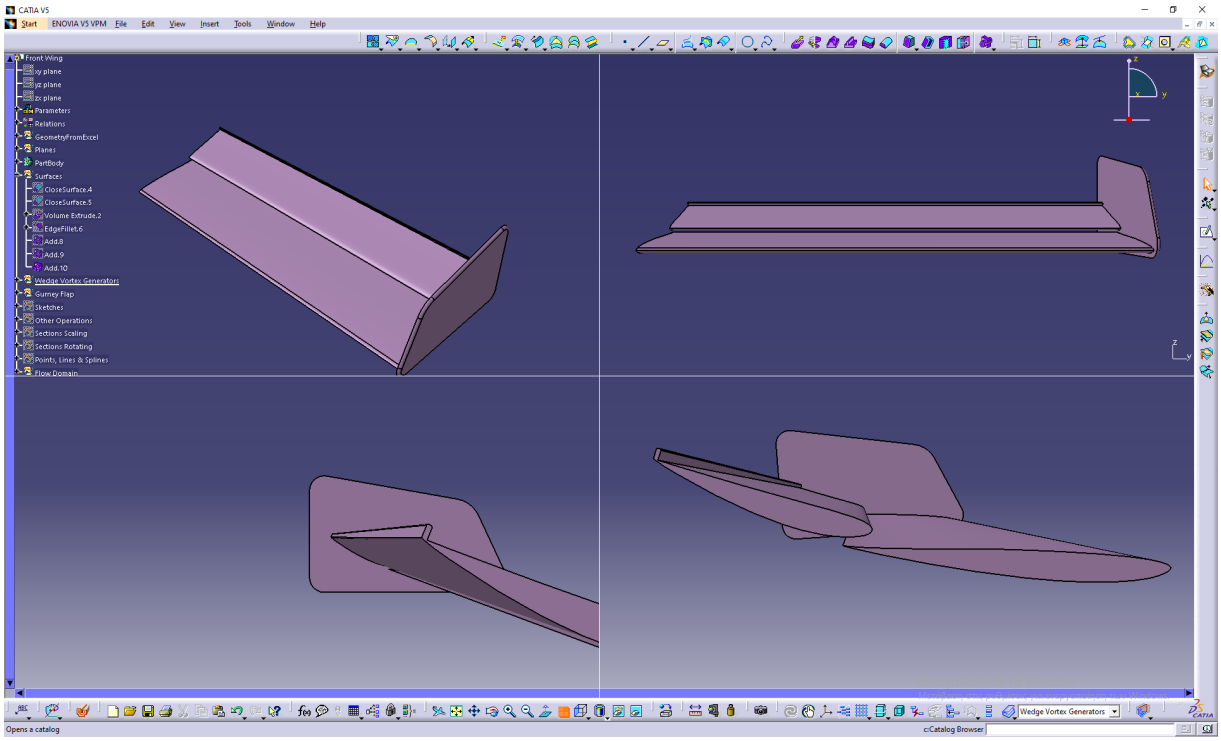

Figure 6.1 Initial front wing remodeling with Gurney Flap addition.

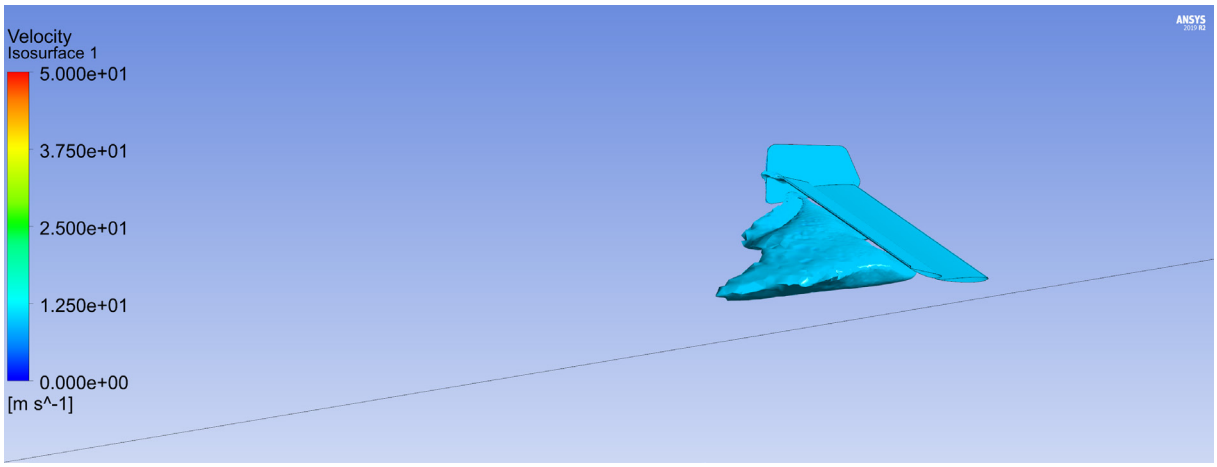

Figure 6.2 Visualization of the wake generated downstream of the front wing. Velocity iso-surface for 10 m/s. The wake is not uniformly distributed behind the wing, due to the existence of a vortex at the inner part of the endplate.

Figure 6.2 provides a visual representation of the wake that is produced downstream of the front wing. It specifically depicts a velocity iso-surface for a speed of 10 m/s. An intricate observation reveals that the wake does not distribute evenly behind the wing. This non-uniformity can be attributed to the presence of a vortex located at the inner section of the endplate. The presence of this vortex plays a significant role in the overall dynamics of the wake formation and distribution, which has implications for the aerodynamic performance of the wing.

Note: The iso-surface is a three-dimensional construct that represents points of a constant velocity within the fluid flow.

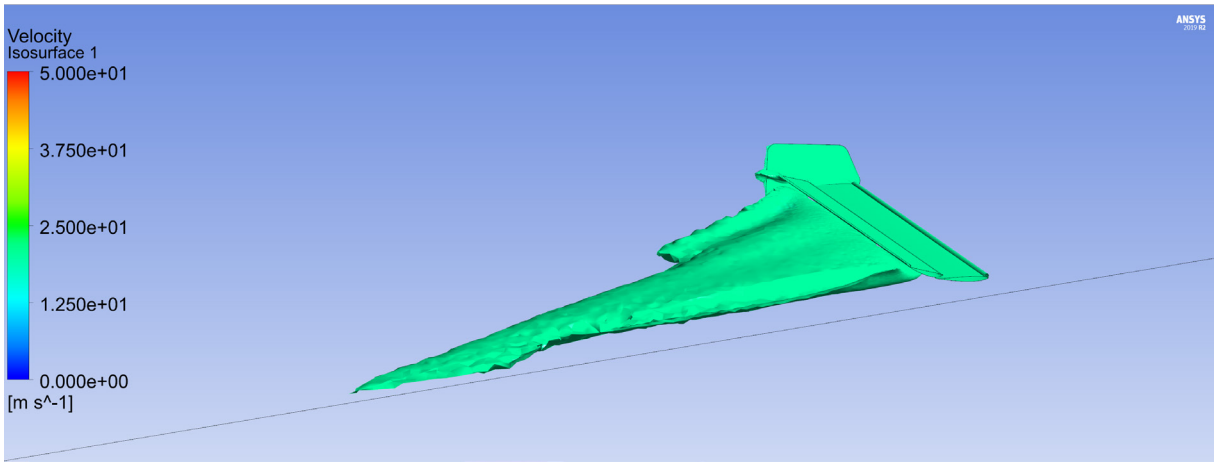

Figure 6.3 Visualization of the wake generated downstream of the front wing. Velocity iso-surface for 20 m/s. The wake is not uniformly distributed behind the wing, due to the existence of a vortex at the inner part of the endplate.

Figure 6.3 provides a visual representation of the wake that is generated downstream of the front wing, specifically on the velocity iso-surface for a speed of 20 m/s. The wake in this case is also not uniformly distributed behind the wing, due to a distinct vortex situated at the inner portion of

the endplate.

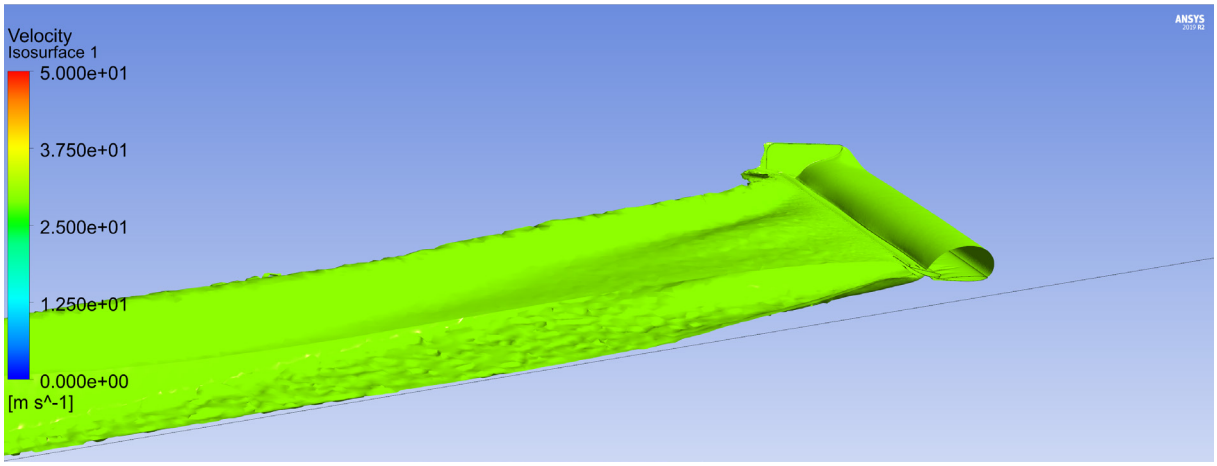

Figure 6.4 Visualization of the wake generated downstream of the front wing. Velocity iso-surface for 30 m/s.

Figure 6.4 provides a visual representation of the wake that is generated downstream of the front wing, on the velocity iso-surface for a speed of 30 m/s.

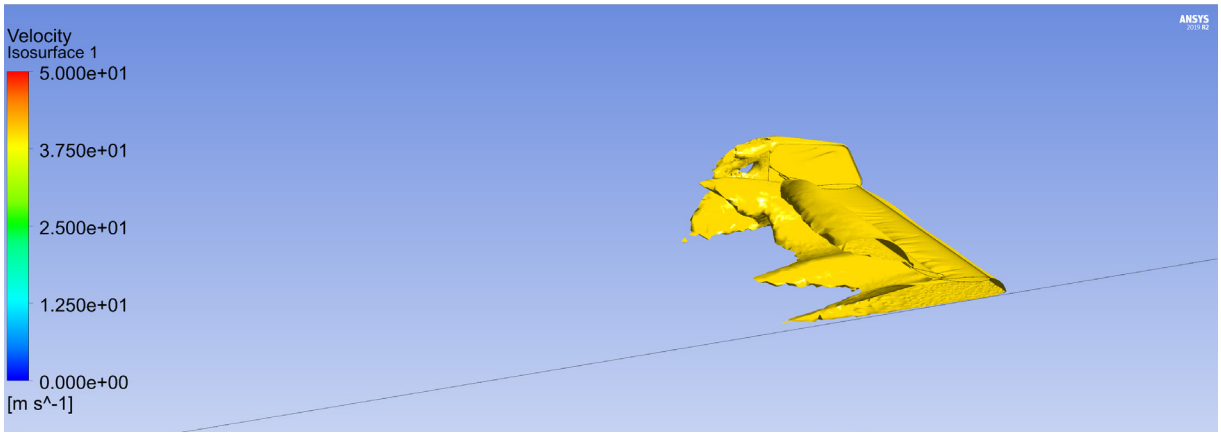

Figure 6.5 Visualization of the wake generated downstream of the front wing. Velocity iso-surface for 40 m/s.

Figure 6.5 provides a visual representation of the wake that is generated downstream of the front wing. The visualization represents a velocity iso-surface for a speed of 40 m/s.

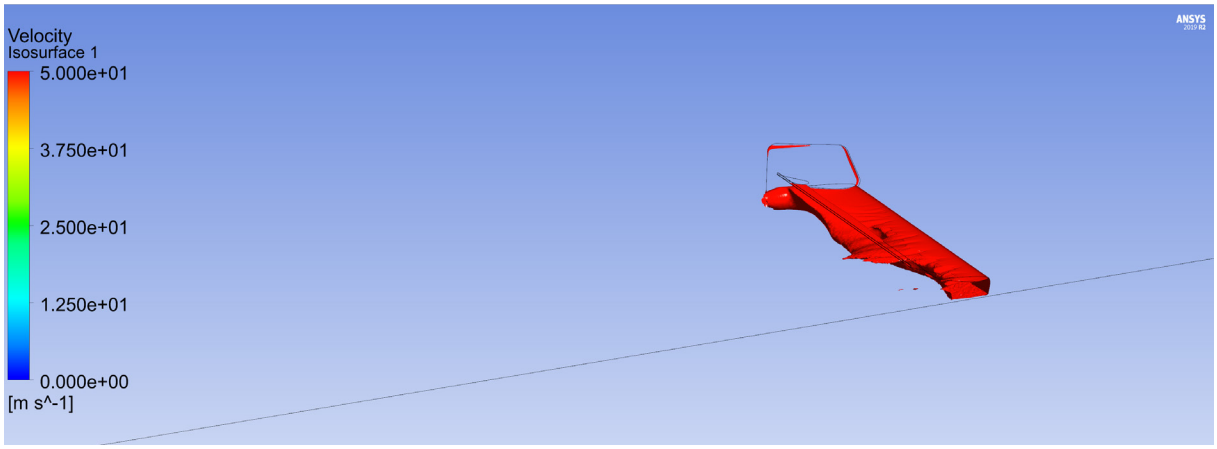

Figure 6.6 Visualization of the wake generated downstream of the front wing. Velocity iso-surface for 50 m/s. The region under the wing is characterized by accelerated flow, due to the contracted area.

Figure 6.6 provides a visual representation of the wake that is generated downstream of the front wing, specifically focusing on the velocity iso-surface for a speed of 50 m/s. The area underneath the wing attracts attention as it exhibits accelerated flow characteristics, attributed to the contracted area. This phenomenon highlights the influence of wing geometry on the flow dynamics, particularly in regions of contraction.

Figure 6.7 Static pressure distribution around the front wing, at the symmetry plane.

Figure 6.7 presents the static pressure distribution around the front wing of the vehicle, at the symmetry plane. This visual representation allows a clear understanding of how the pressure is dispersed.

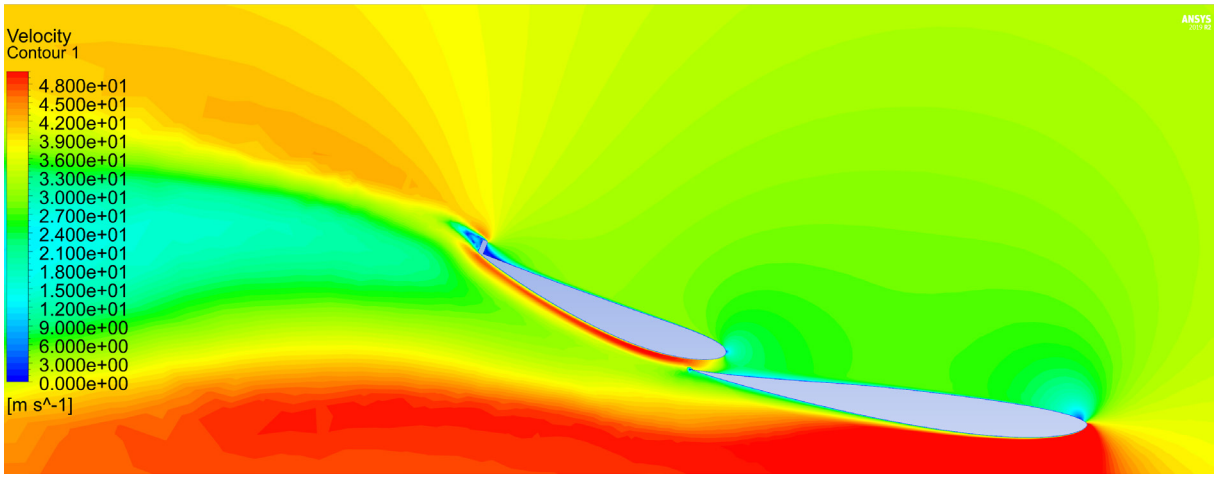

Figure 6.8 Velocity distribution around the front wing, at the symmetry plane. The small recirculation zone downstream of the Gurney Flap can be observed.

Figure 6.8 shows the velocity distribution around the front wing, which is illustrated at the symmetry plane. In this detailed representation, one can clearly observe the intricate patterns of velocity distribution that play a crucial role in the aerodynamics of the wing. In particular, one notable feature that can be discerned is the small recirculation zone located downstream of the Gurney Flap.

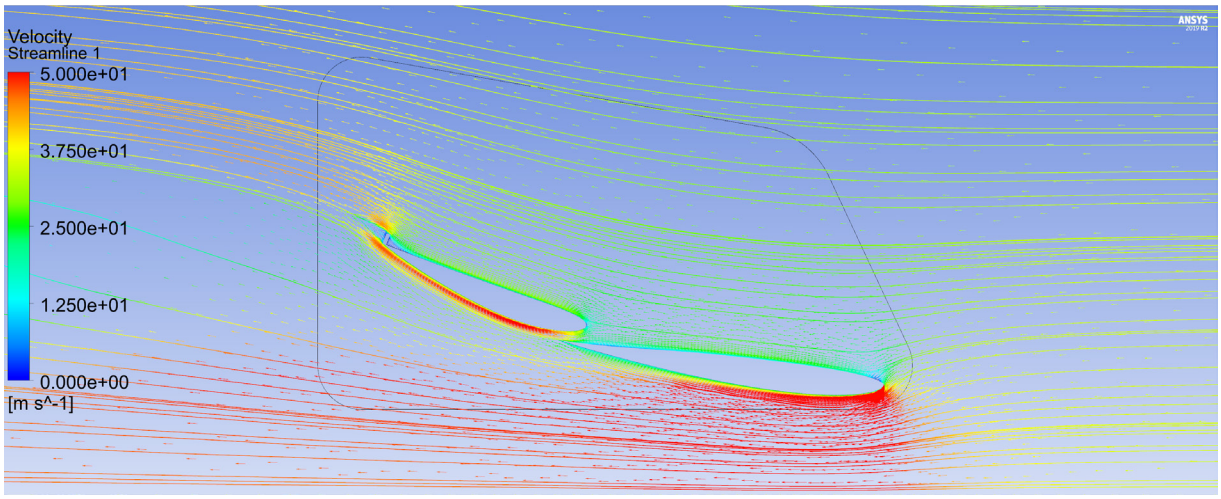

Figure 6.9 Velocity vectors and streamlines around the front wing, at the symmetry plane.

Figure 6.9 presents an intricate view of the velocity vectors and streamlines surrounding the front wing, at the symmetry plane. This visual representation offers a clear understanding of the aerodynamic behavior in this area.

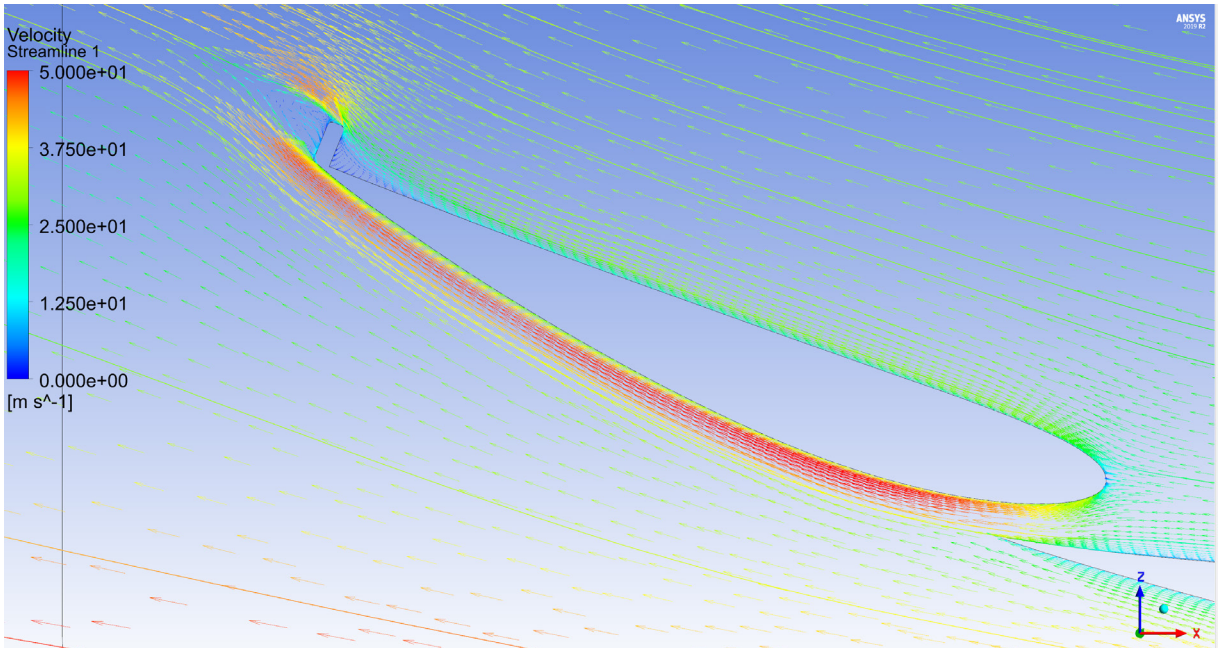

Figure 6.10 Close-up of the velocity vectors and streamlines around the front wing's Gurney Flap, at the symmetry plane.

Figure 6.10 provides a detailed close-up view of the velocity vectors and streamlines swirling around the Gurney Flap of the front wing. This figure is also focused on the symmetry plane.

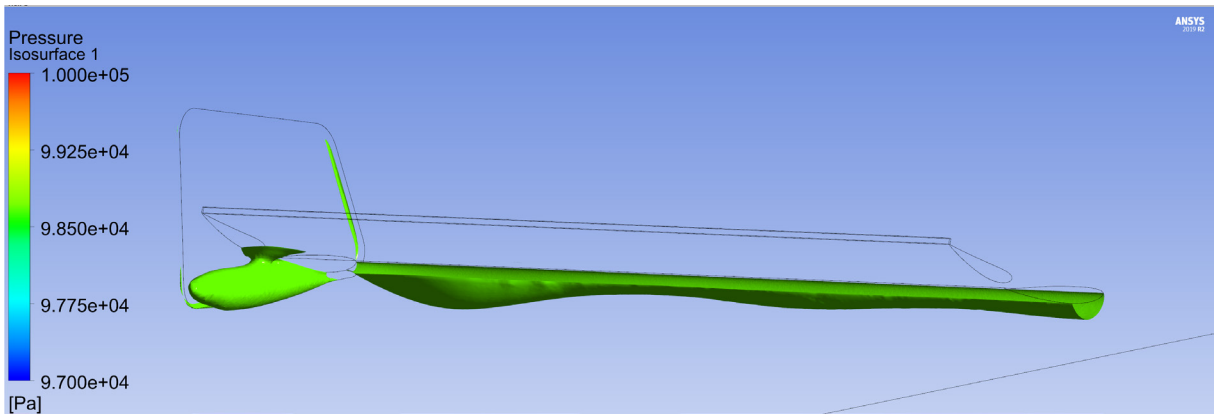

Figure 6.11 Static pressure iso-surface visualized for 98700 Pa around the front wing. The existence of a "conical" low pressure region at the inner face of the endplate indicates the position of a vortex.

Figure 6.11 demonstrates the static pressure iso-surface for 98700 Pa, focused around the area of the front wing. A noteworthy observation from the figure is the presence of a distinct "conical" region which is characterized by low pressure. This specific zone is located on the inner face of the endplate. The importance of identifying this region lies in the fact that it is indicative of the position of a vortex.

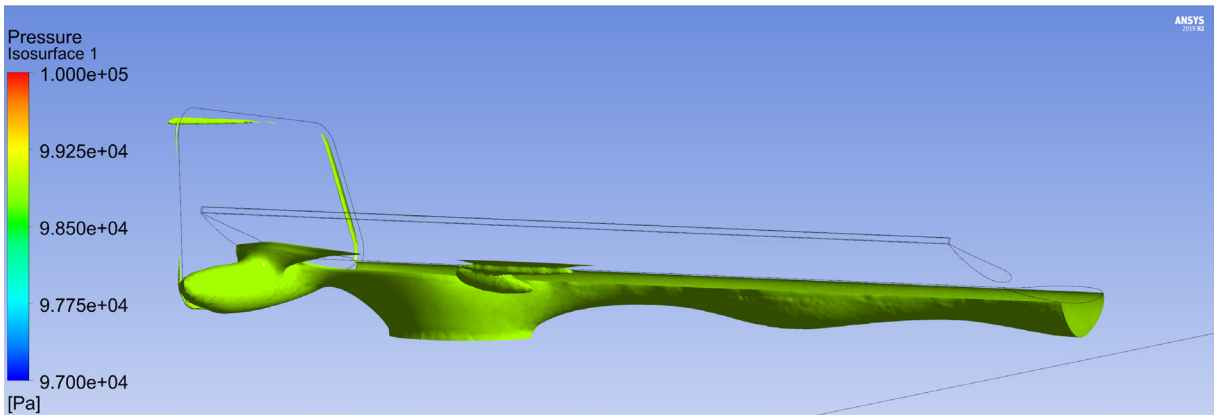

Figure 6.12 Static pressure iso-surface visualized for 98900 Pa around the front wing. The existence of a "conical" low pressure region at the inner face of the endplate indicates the position of a vortex.

Figure 6.12 provides a visualization of the static pressure iso-surface around the front wing, specifically for a pressure of 98900 Pa. One of the key observations from this figure is the existence of a "conical" low pressure region, which can be seen clearly on the inner face of the endplate. The presence of this distinct, conical low pressure area is indicative of the position of a vortex.

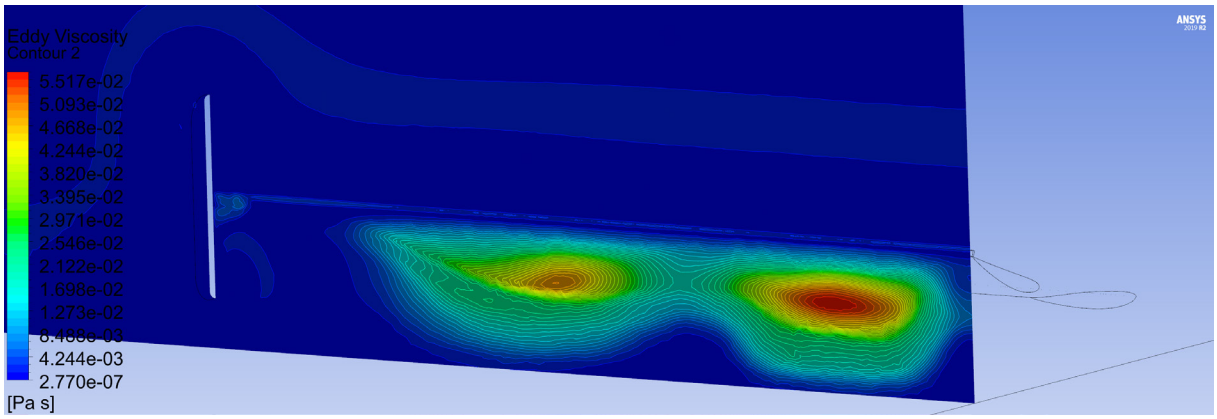

Figure 6.13 Eddie Viscosity contours on a transverse plane behind the front wing's trailing edge, indicating the separated flow under the wing. The formation of the vortex at the inner part of the endplate prevails the separation at the outer part of the wing.

Figure 6.13 presents Eddie Viscosity contours on a transverse plane located behind the trailing edge of the front wing, clearly indicating the separated flow occurring under the wing. More specifically, the formation of the vortex at the inner part of the endplate is a significant observation, as it prevails over the separation seen at the outer part of the wing. This suggests a dominance of the inner vortex, which is a critical aspect to consider in the design and performance optimization of such aerodynamic structures.

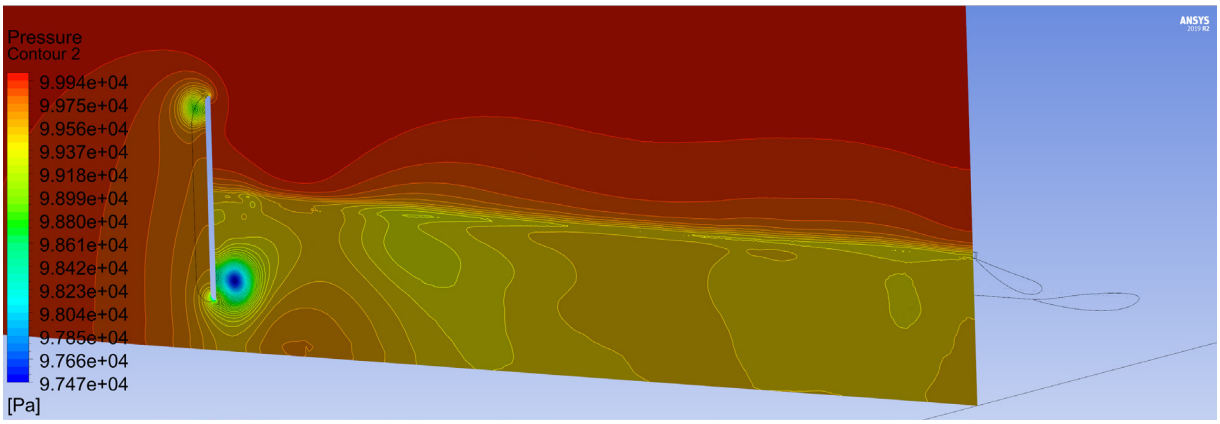

Figure 6.14 Static pressure contours on a transverse plane behind the front wing's trailing edge. The formation of two vortices at the endplate is evident. The upper one is on the external surface, while the lower one is formed in the internal surface of the endplate. The vortices are formed due to the pressure difference between the inner and outer flow. At the upper surface of the wing, the higher pressure pushes the flow over the endplate towards its external surface. The opposite is evident for the lower surface of the wing.

Figure 6.14 illustrates the static pressure contours on a transverse plane situated just behind the trailing edge of the front wing. It can be observed the formation of two distinct vortices at the endplate. The positioning of these vortices is quite evident - the upper vortex is found on the external surface, while the lower vortex has formed on the internal surface of the endplate. These vortices are a direct result of the pressure difference between the inner and outer flow of air. Furthermore, the mechanics at work on the upper surface of the wing become apparent - the pressure here is higher, and this effectively pushes the flow of air over the endplate and towards its external surface. Conversely, the lower surface of the wing displays the opposite behavior.

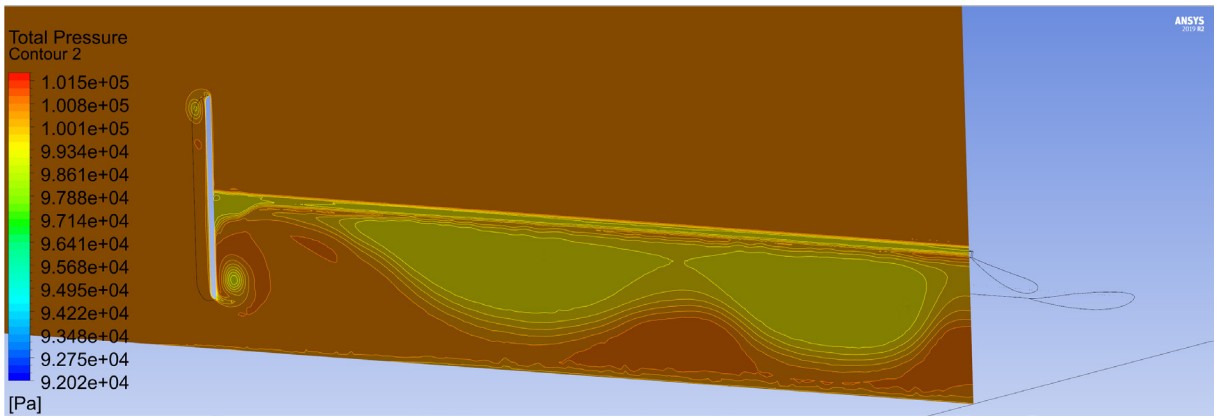

Figure 6.15 Total pressure contours on a transverse plane behind the front wing's trailing edge. The position of the separated flow can be observed, as well as the positions of the two vortices at the endplate.

Figure 6.15 showcases the total pressure contours on a transverse plane located just behind the trailing edge of the front wing. This visualization allows for a clear view of the position where the flow separates, which is a critical aspect of understanding the aerodynamics of the wing. Additionally, the formation and positions of the two vortices at the endplate are evident.

Figure 6.16 shows the velocity streamlines around the front wing. It can be observed the recirculating flow in the region where the air separates from the surface of the wing. Also evident is the vertical flow at the two vortices that form at the endplate.

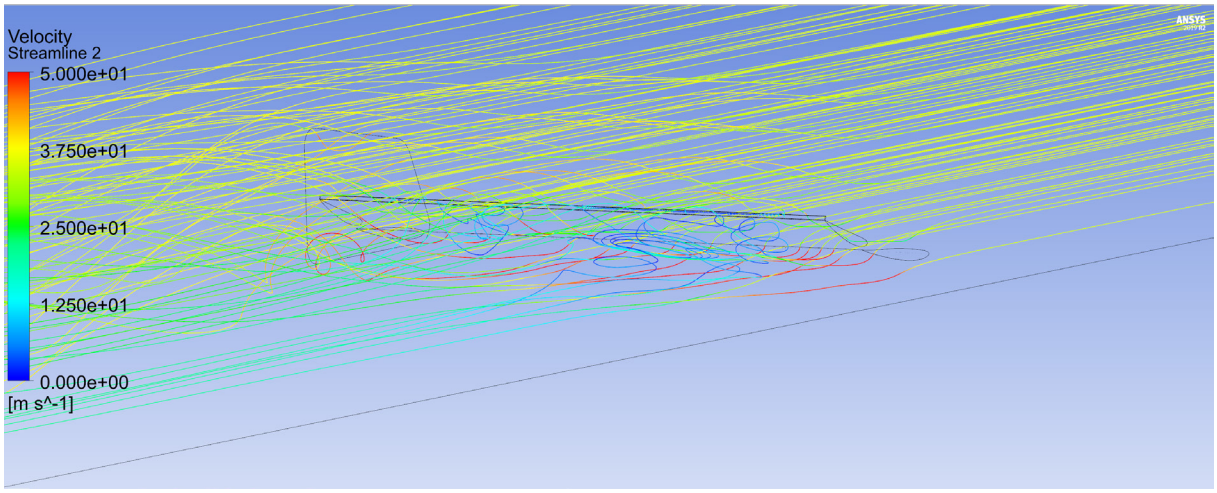

Figure 6.16 Velocity streamlines around the front wing. The recirculating flow at the separated region is evident, as well as the vertical flow at the two vortices formed at the endplate.

6.2.2 Double Airfoil Front Wing with Gurney Flap and Wedge Vortex Generators - Model 3

Model 2 was also remodeled, resulting in the third and final model (model 3). In this remodel wedge vortex generators were added across the suction side of the first element of the wing, as well as both airfoils were rescaled with larger chords. The wedge vortex generators can be seen in Figure 2.28 E, in subsection 2.7.1.5, “Vortex Generators”.

The parameters used to create the Wedge Vortex Generators are displayed in the table below.

Parameter	Unit	Desrcription
VG Height	Angle (deg)	The Height of the VGs
VG Width	Length (mm)	The Width of the VGs
VG Distance	Lenght (mm)	The distance between the VGs

Table 3 - Parameters used in model 3.

The Wedge VGs placed on the front wing are displayed in Figure 6.17. The final model can be seen in Figure 6.18.

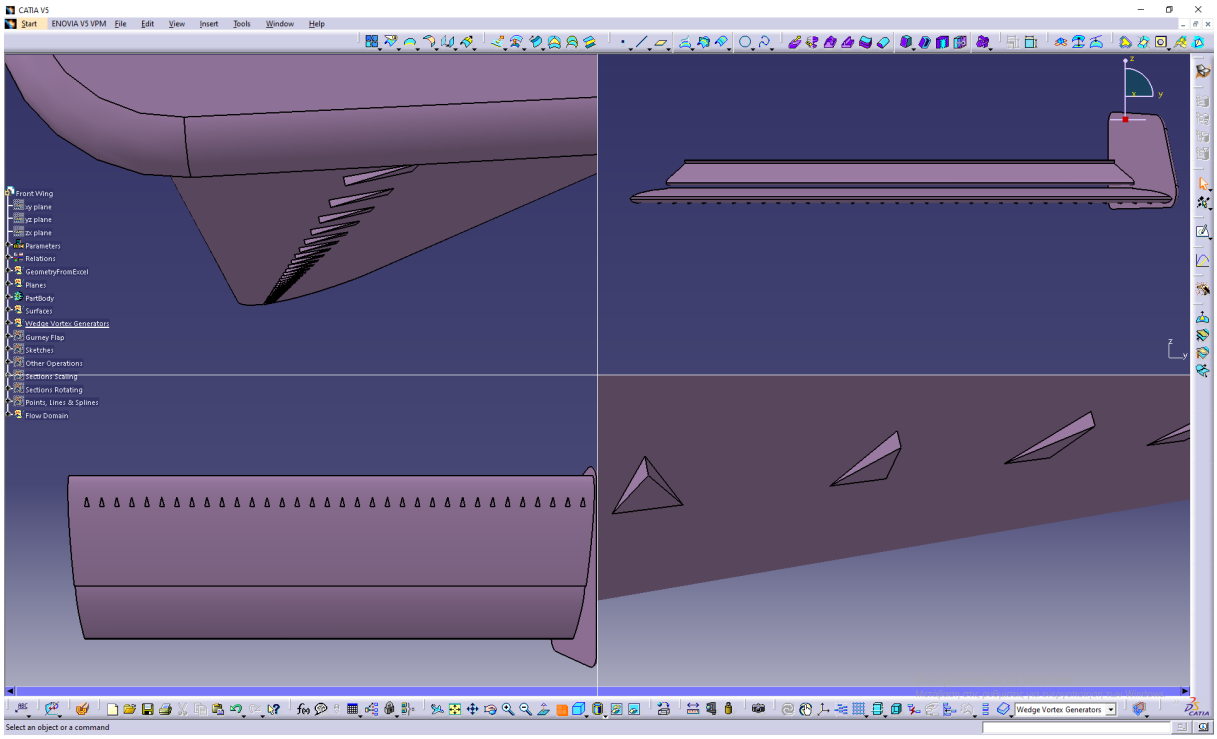

Figure 6.17 Wedge VGs placed on the suction side of the first element of the wing, resulting in model 3.

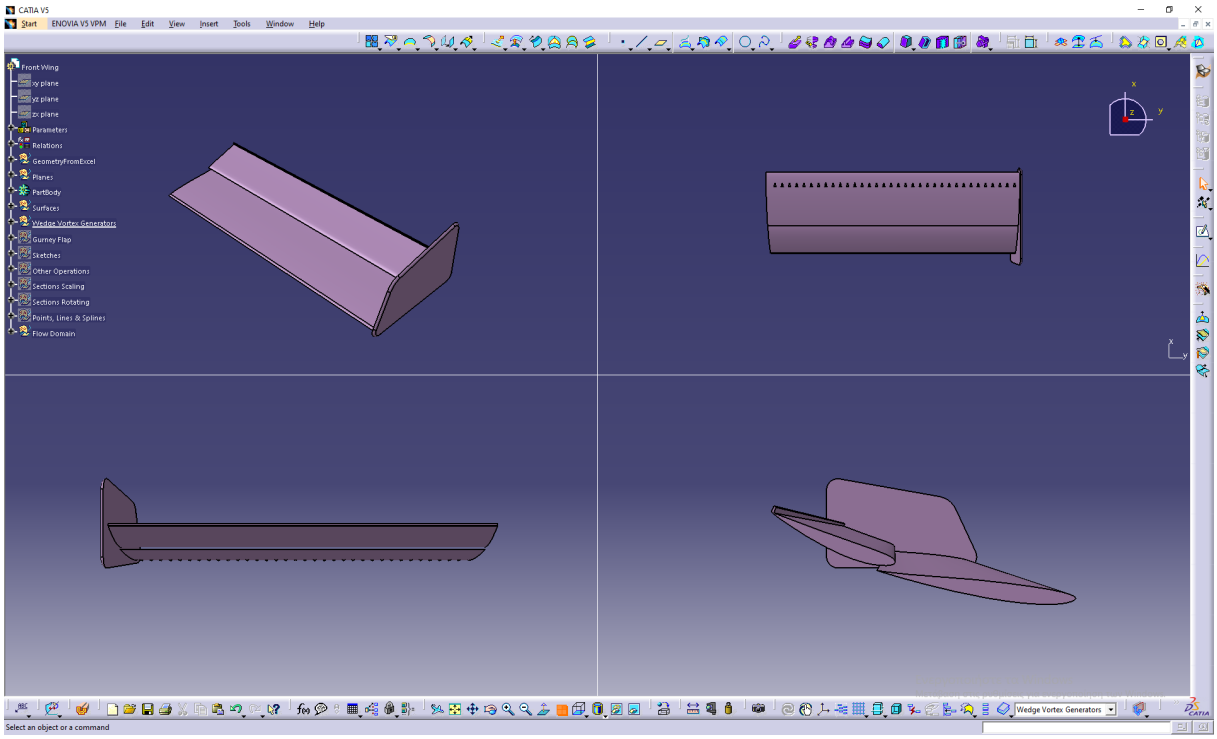

Figure 6.18 Final model featuring a Gurney Flap on the second element of the wing, and wedge VGs positioned across the suction side of the first element of the wing.

Results

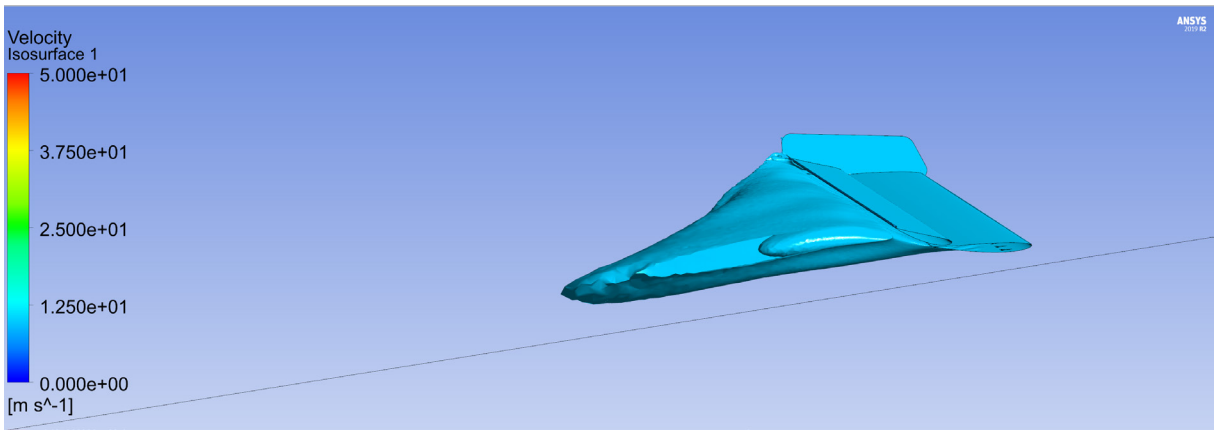

Figure 6.19 Visualization of the wake generated downstream of the front wing. Velocity iso-surface for 10 m/s. The wake is not uniformly distributed behind the wing, due to the existence of a vortex at the inner part of the endplate.

Figure 6.19 provides a visualization of the wake that is generated downstream of the front wing. This visualization gives a clear depiction of a velocity iso-surface for a speed of 10 m/s. One noteworthy observation about the wake is that it is not uniformly distributed in the area directly behind the wing. The reason for this lack of uniformity is attributed to the existence of a vortex located at the inner part of the endplate of the wing.

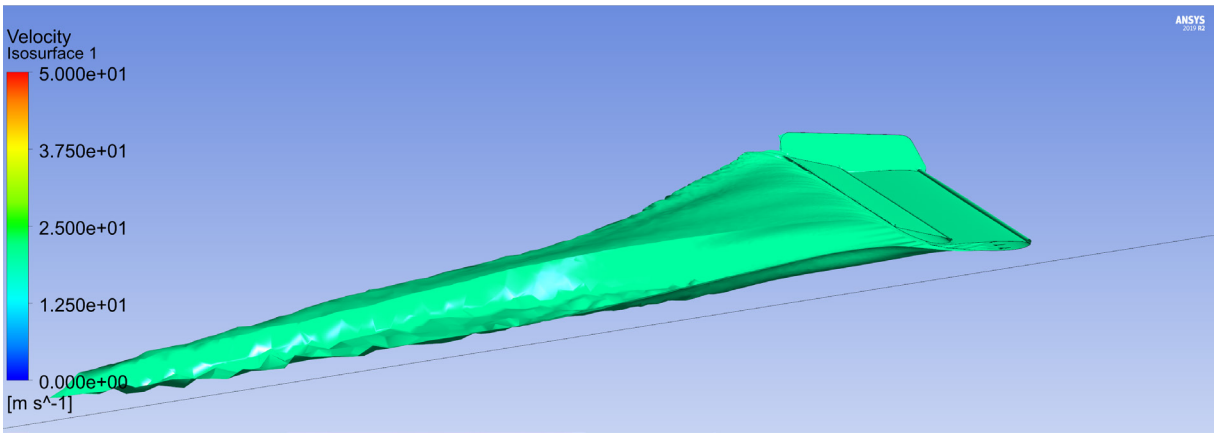

Figure 6.20 Visualization of the wake generated downstream of the front wing. Velocity iso-surface for 20 m/s. The wake is not uniformly distributed behind the wing, due to the existence of a vortex at the inner part of the endplate

Figure 6.20 provides a visualization of the wake that is generated downstream of the front wing, demonstrating a velocity iso-surface for a speed of 20 m/s. This figure gives a clear depiction of how the wake, rather than being uniformly distributed behind the wing, shows a distinct pattern. This uneven distribution is primarily due to the existence of a vortex which can be observed at the inner part of the endplate. The presence of this vortex significantly affects the dispersion of the wake, thereby creating a non-uniform flow behind the wing.

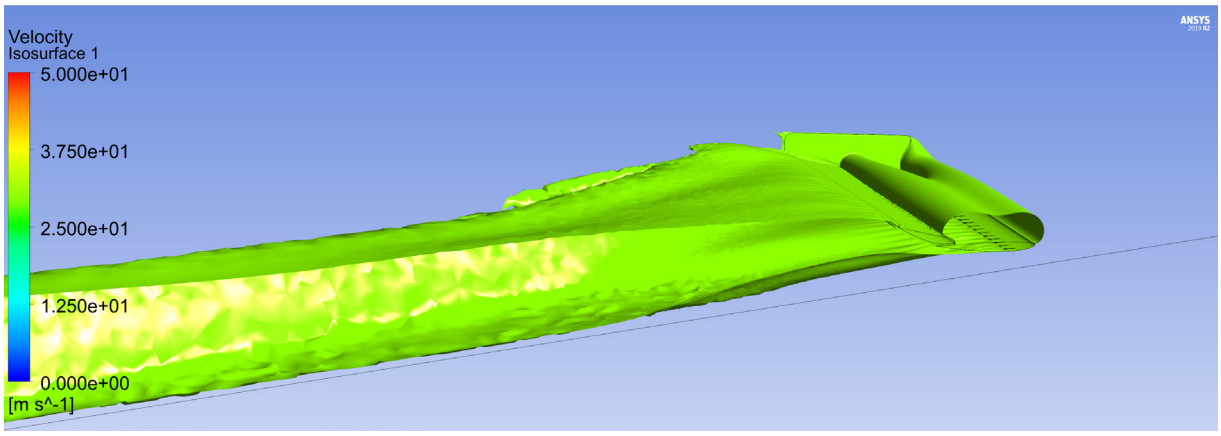

Figure 6.21 Visualization of the wake generated downstream of the front wing. Velocity iso-surface for 30 m/s.

Figure 6.21 presents a visualization of the wake that is generated downstream of the front wing. The velocity iso-surface for this visualization is set at 30 m/s.

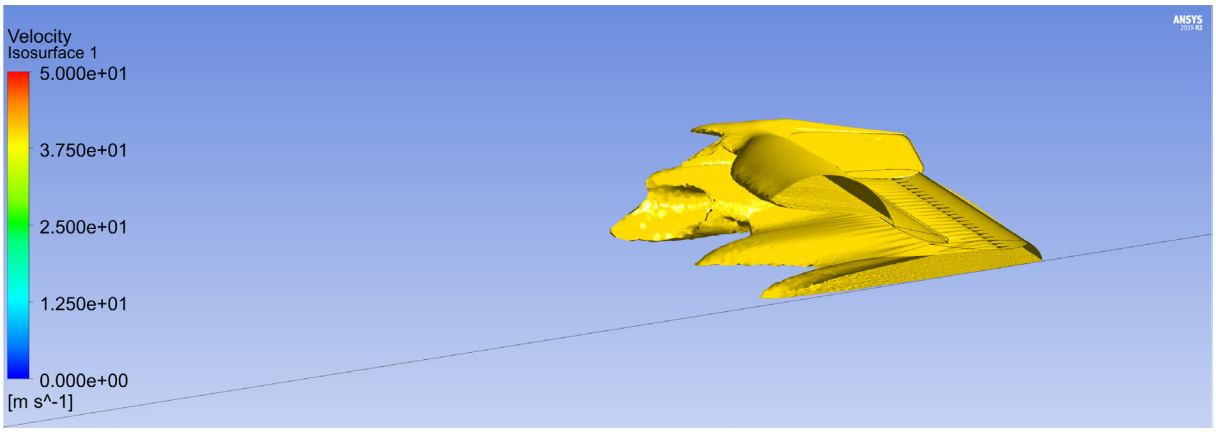

Figure 6.22 Visualization of the wake generated downstream of the front wing. Velocity iso-surface for 40 m/s.

Figure 6.22 provides a visualization of the wake that is generated downstream of the front wing. This image illustrates a velocity iso-surface for a speed of 40 m/s.

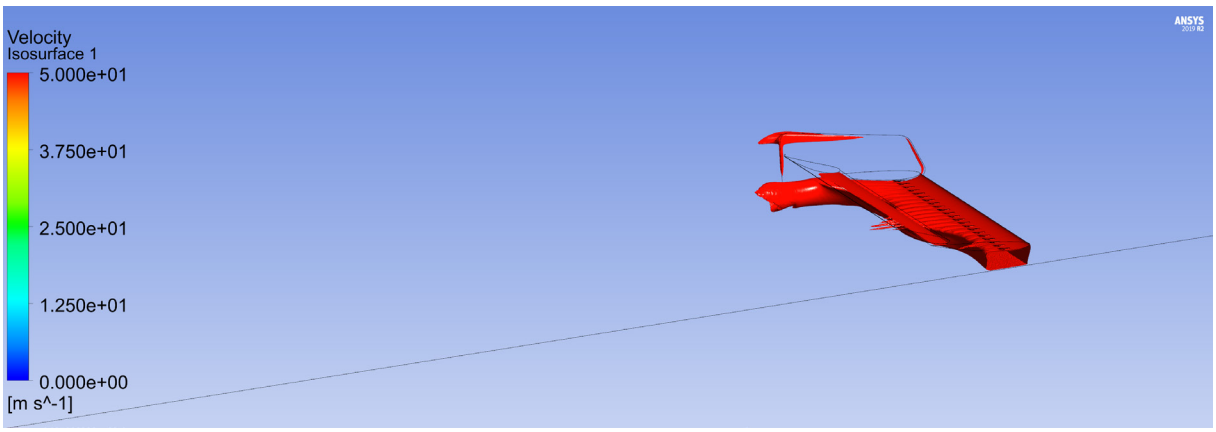

Figure 6.23 Visualization of the wake generated downstream of the front wing. Velocity iso-surface for 50 m/s. The region under the wing is characterized by accelerated flow, due to the contracted area.

Figure 6.23 provides a visualization of the wake generated downstream of the front wing. The velocity iso-surface for this visualization is set at 50 m/s. The specific region located under the wing is particularly noteworthy due to the accelerated flow that is present there. This unique characteristic is largely due to the contracted area that can be observed in this region.

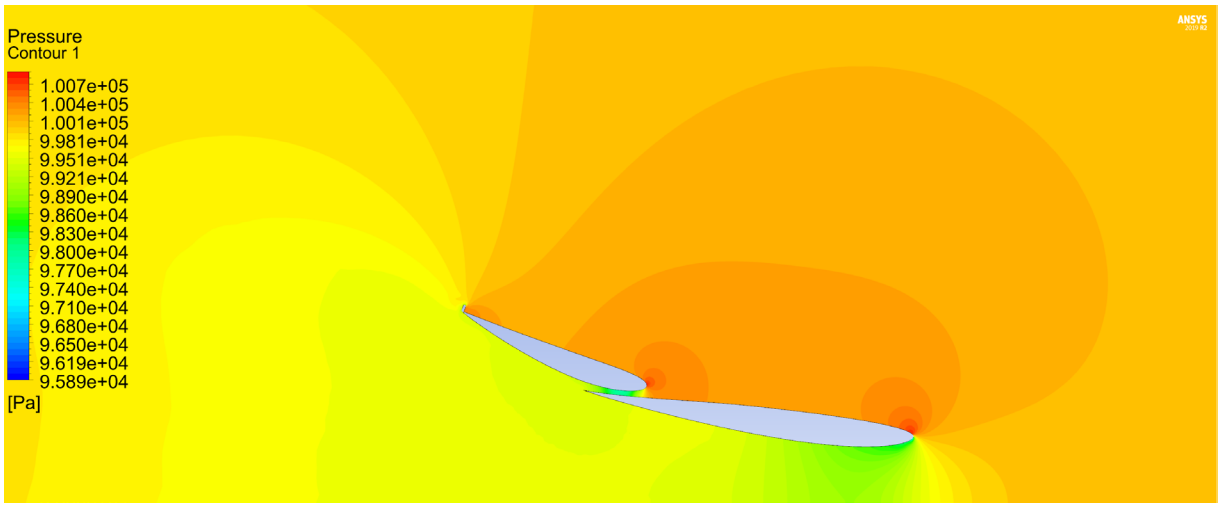

Figure 6.24 Static pressure distribution around the front wing, at the symmetry plane.

Figure 6.24 shows the static pressure distribution around the front wing, situated at the symmetry plane. This representation provides a detailed view of how the forces are distributed across the surface of the wing.

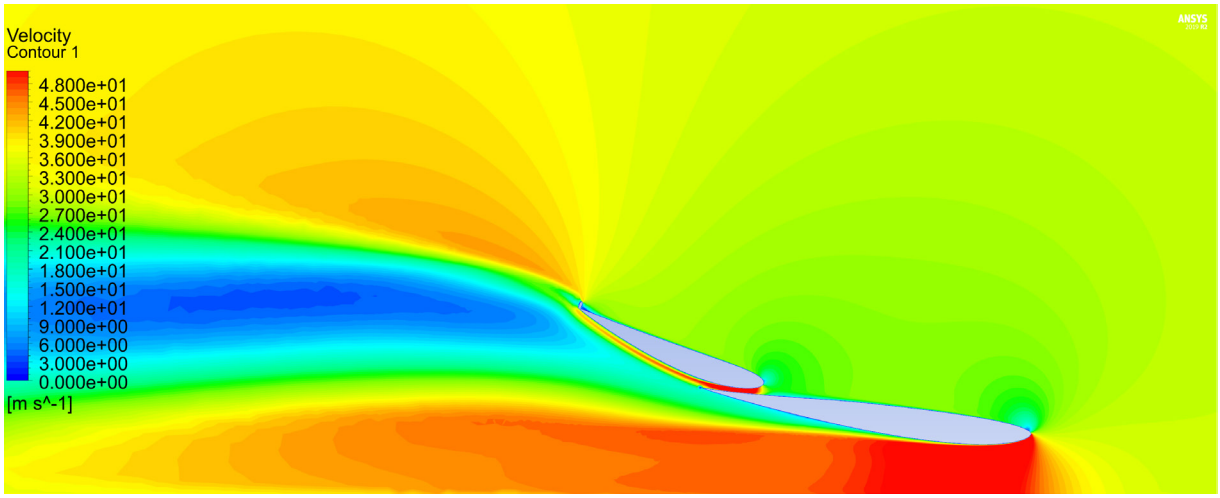

Figure 6.25 Velocity distribution around the front wing, at the symmetry plane. The small recirculation zone downstream of the Gurney Flap can be observed.

Figure 6.25 illustrates the velocity distribution surrounding the front wing, located at the symmetry plane. This graphic representation clearly shows the dynamics of the airflow. Notably, the small recirculation zone situated downstream of the Gurney Flap can be observed.

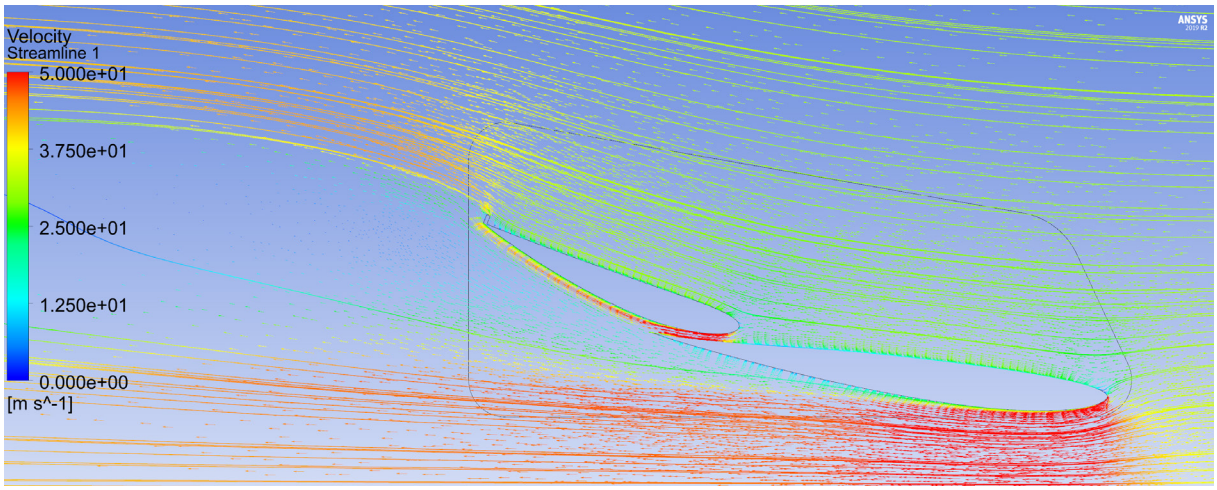

Figure 6.26 Velocity vectors and streamlines around the front wing, at the symmetry plane.

Figure 6.26 displays the velocity vectors and streamlines around the front wing. The visualization is presented at the symmetry plane. This comprehensive view allows for a thorough examination of the airflow dynamics, speed, and direction at different points around the front wing.

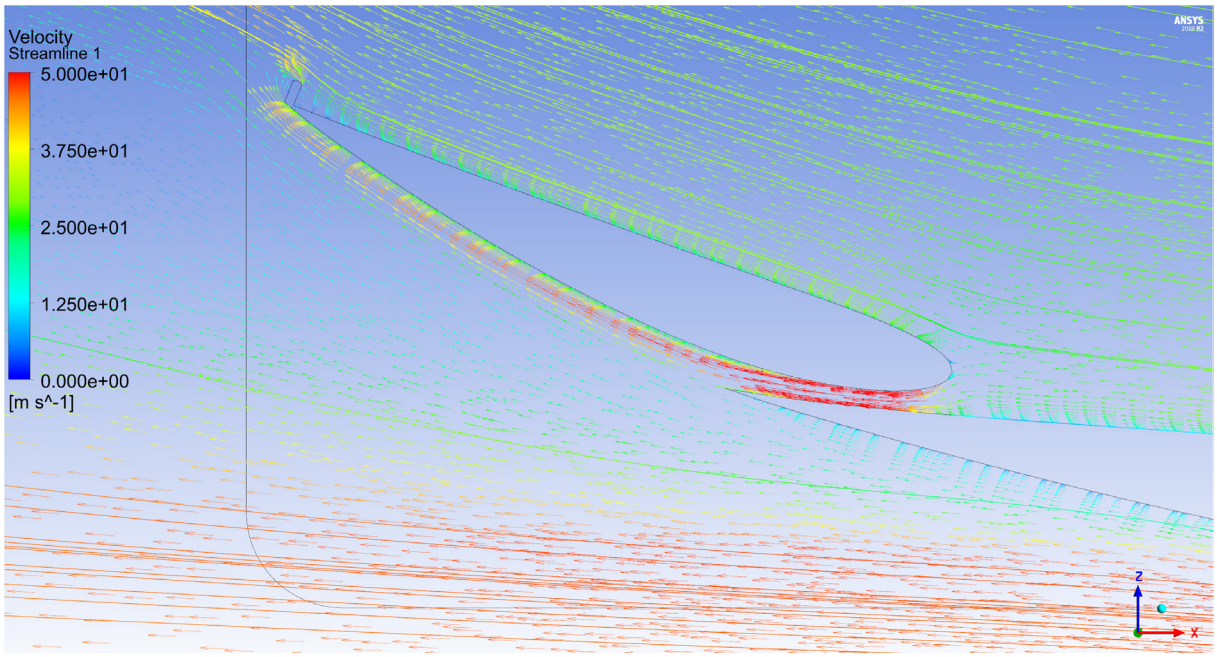

Figure 6.27 Close-up of the velocity vectors and streamlines around the front wing's Gurney Flap, at the symmetry plane.

Figure 6.27 provides a detailed, close-up view of the velocity vectors and streamlines that are present around the Gurney Flap. This examination is also at the symmetry plane.

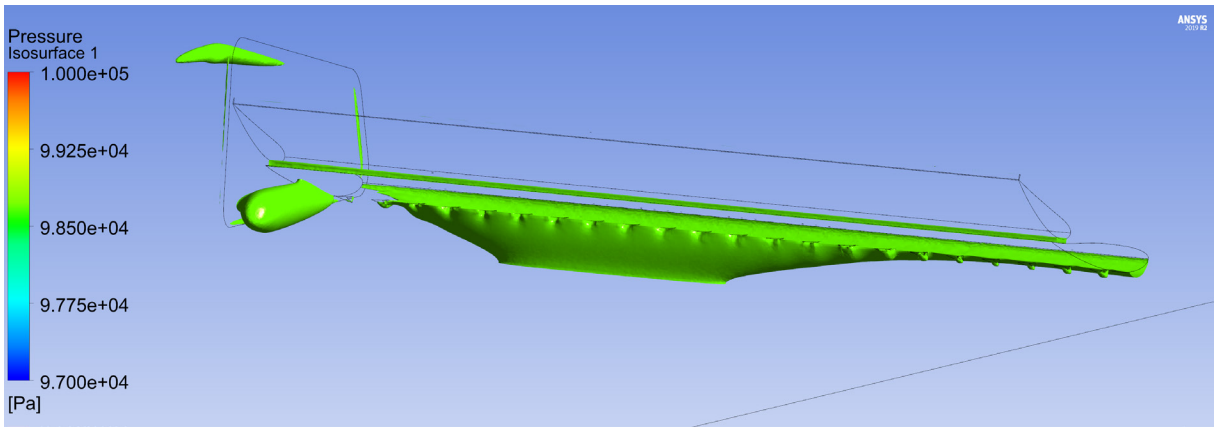

Figure 6.28 Static pressure iso-surface visualized for 98700 Pa around the front wing. The existence of a "conical" low pressure region at the inner face of the endplate indicates the position of a vortex.

Figure 6.28 presents a visualization of the static pressure iso-surface for 98700 Pa situated around the front wing. In this figure, the depiction of a distinct "conical" low pressure region can be noticed at the inner face of the endplate. This specific feature is critical as it signals the existence and location of a vortex.

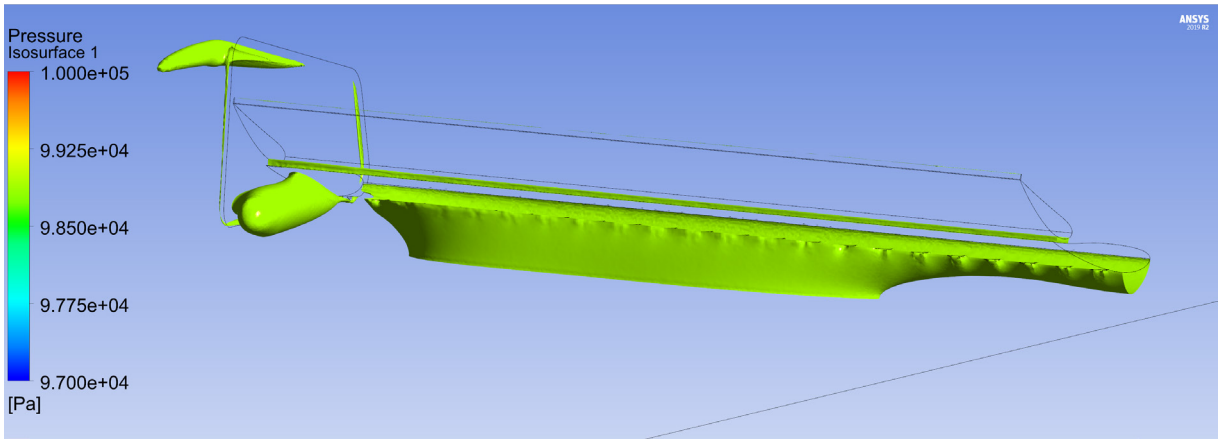

Figure 6.29 Static pressure iso-surface visualized for 98900 Pa around the front wing. The existence of a "conical" low pressure region at the inner face of the endplate indicates the position of a vortex.

Figure 6.29 demonstrates the visualization of a static pressure iso-surface for 98900 Pa located around the front wing. It is important to note the existence of a distinct low-pressure region, which appears in a unique "conical" shape, located at the inner face of the endplate. This specific feature is indicative of the position of a vortex.

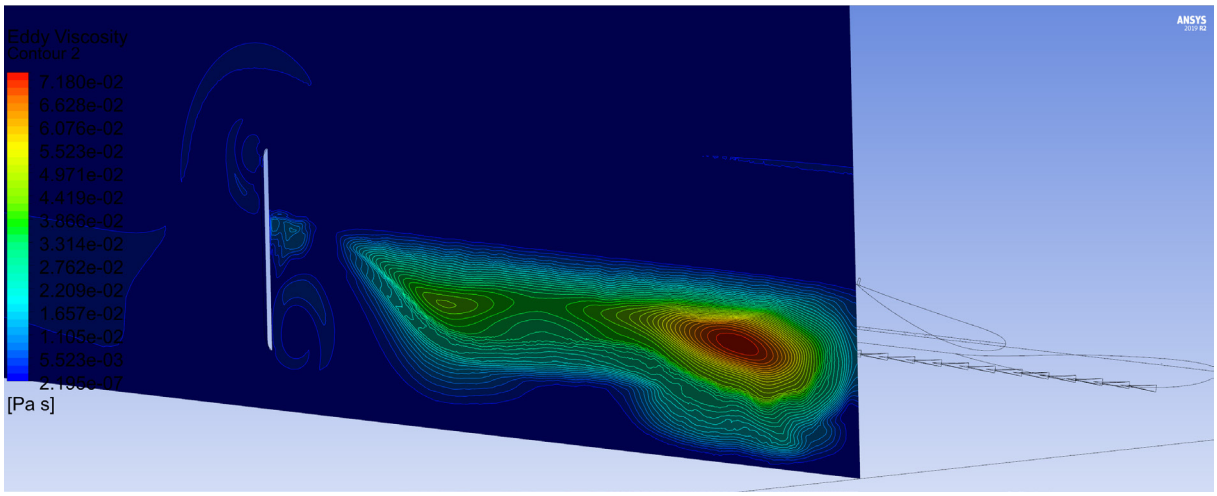

Figure 6.30 Eddie Viscosity contours on a transverse plane behind the front wing's trailing edge, indicating the separated flow under the wing. The formation of the vortex at the inner part of the endplate prevails the separation at the outer part of the wing.

Figure 6.30 presents the Eddie Viscosity contours on a transverse plane, located behind the front wing's trailing edge. The contours clearly demonstrate the separated flow which is occurring under the wing. Additionally, the formation of the vortex at the inner part of the endplate is also depicted. This vortex formation is particularly notable as it prevails over the separation that is observed at the outer part of the wing.

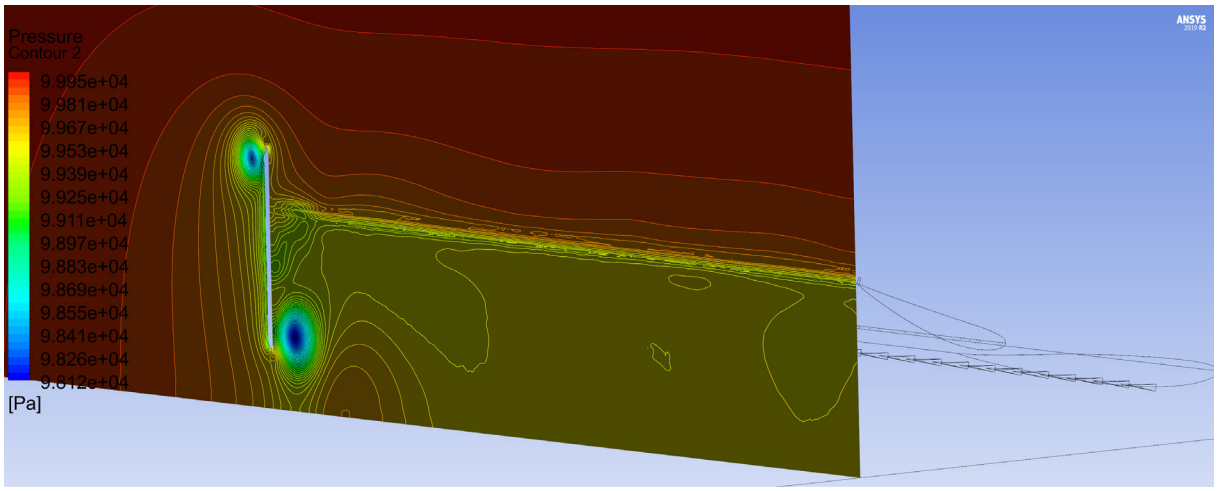

Figure 6.31 Static pressure contours on a transverse plane behind the front wing's trailing edge. The formation of two vortices at the endplate is evident. The upper one is on the external surface, while the lower one is formed in the internal surface of the endplate. The vortices are formed due to the pressure difference between the inner and outer flow. At the upper surface of the wing, the higher pressure pushes the flow over the endplate towards its external surface. The opposite is evident for the lower surface of the wing.

Figure 6.31 illustrates the static pressure contours on a transverse plane positioned behind the trailing edge of the front wing. What becomes immediately apparent is the formation of two distinct vortices at the endplate. The first vortex can be observed on the external surface of the endplate, located in the upper region, while the second vortex is formed on the internal surface of the

endplate, located lower. These vortices emerge as a direct result of the pressure difference that exists between the internal and external flow. When we look at the upper surface of the wing, we can see that the higher pressure forces the flow over the endplate, pushing it toward the external surface of the endplate. A contrasting scenario occurs for the lower surface of the wing where the opposite effect is clear.

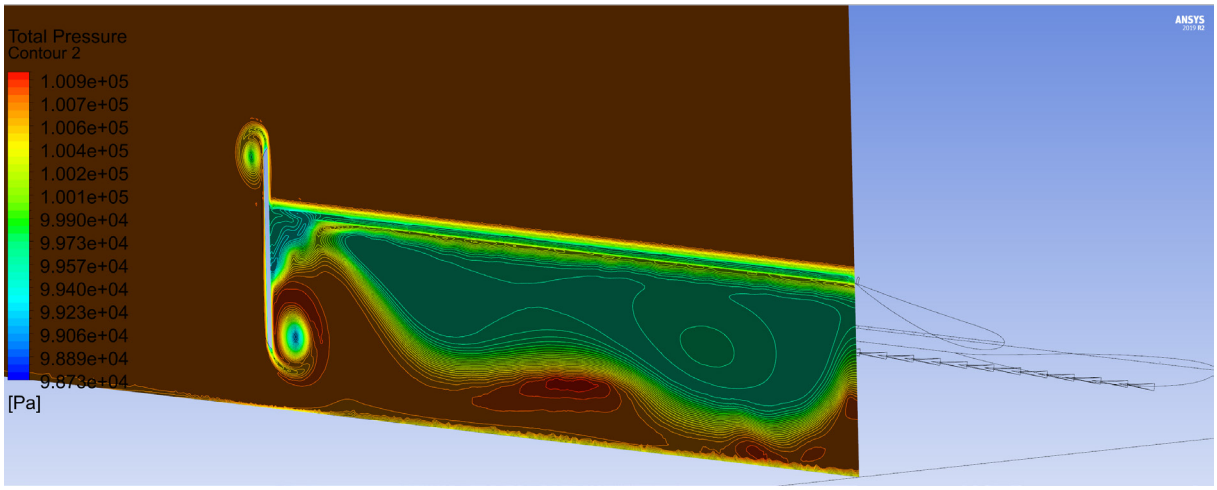

Figure 6.32 Total pressure contours on a transverse plane behind the front wing's trailing edge. The position of the separated flow can be observed, as well as the positions of the two vortices at the endplate.

Figure 6.32 displays the total pressure contours on a transverse plane located behind the trailing edge of the front wing. This graphic representation allows us to observe the precise location of the separated flow. In addition to this, we can also determine the positions of the two vortices that are formed at the endplate.

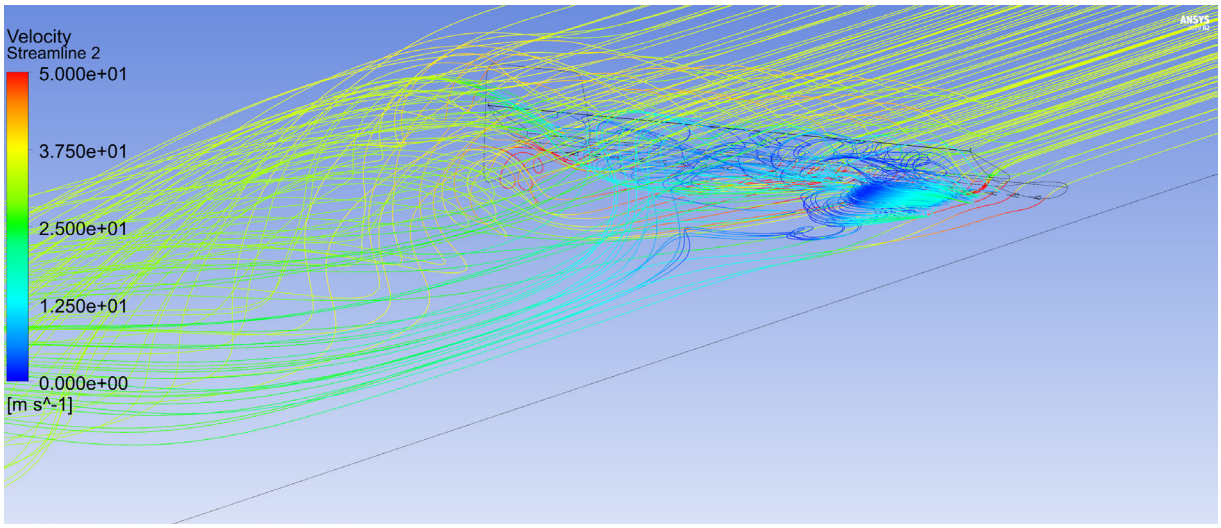

Figure 6.33 Velocity streamlines around the front wing. The recirculating flow at the separated region is evident, as well as the vertical flow at the two vortices formed at the endplate.

Figure 6.33 illustrates the velocity streamlines around the front wing. It is clear that there is recirculating flow present in the separated region, indicating a repetitive motion of particles in the fluid.

Additionally, the figure also presents the existence of vertical flow at the two vortices formed at the endplate.

6.2.3 Analysis Summary

From the previous analysis, it was revealed that the initial configuration with the simple double airfoils was inadequate to achieve a steady-state flow. The code did not converge to a steady-state solution. By adding the Gurney flap at the trailing edge of the second airfoil the convergence was substantially improved. However, a large recirculation zone was formed behind the rear airfoil. The computed forces upon the double wing were L=209.5N and D=42.4 N, L/D =4.94 (for half the wing), with the Lift considered insufficient for the application at hand. For this reason, the 3rd model was rescaled with larger chords for both airfoils, and the Vortex Generators were added. For this case, the computed forces were L= 274N and D = 54.84 N (for half the wing) with L/D = 5.0. As it can be observed, a small increase to the L/D was achieved, while the larger values of Lift and Drag are due to the increased chord of the two airfoils, compared to the previous design. The flow under the front airfoil with the VGs demonstrated a higher uniformity, due to the formed vortices. It is noteworthy for both cases that the existence of the vortex at the inner bottom side of the endplate has a favorable result on the reduction of the detached flow at the outer part of the double wing. This requires further investigation, as it can be utilized as a means for further reduction of the detached flow.

BIBLIOGRAPHY

Abbott, I.H. and Doenhoff, V (1959). *Theory of Wing Sections: Including a Summary of Airfoil Data*. New York: Dover Publications.

Ansys, Inc (2024). Ansys CFX | Industry-Leading CFD Software. Available at: https://www.ansys.com/products/fluids/ansys-cfx [Accessed 23 Feb. 2024]

Anderson, J (2017). *Fundamentals of aerodynamics.* New York: Mcgraw-Hill.

Aristotle Racing Team (2018). *Racing Cars*. Available at: https://aristotleracing.gr/racing-cars/ [Accessed 8 Feb. 2024].

Bhatnagar, U.R (2014). *Formula 1 Race Car Performance Improvement by Optimization of the Aerodynamic Relationship between the Front and Rear Wings.* Master Thesis.

Carpentiers, N (2018). *Tech F1i: The Birth of a Formula 1 Car.* Available at: https://f1i.com/magazine/magazine-technical/289948-birth-formula-1-car-conceptual-work.html [Accessed 14 Mar. 2023].

Centaurus Racing Team (2018). *Our Cars - Centaurus Racing Team*. Available at: https://centaurusracing.gr/en/our-cars/ [Accessed 8 Feb. 2024].

Chavda, P. and Ajudia, D (2018). 'An Aerodynamics Analysis of Rear Wing of Formula – 1 Car Using Eppler E423 as Wing Profile', *International Journal of Research in Advent Technology,* 6(12).

Dahlberg, H (2014). *Aerodynamic Development of Formula Student Race Car*. Bachelor Thesis. KTH Royal Institute of Technology. Available at: https://kth.diva-portal.org/smash/record.jsf?pid=diva2%3A737287&dswid=-8077 [Accessed 14 Mar. 2023].

Dharmawan, M.A., Ubaidillah, Nugraha, A.A., Wijayanta, A.T. and Naufal, B.A (2018). ' Aerodynamic Analysis of Formula Student Car ', *AIP Conference Proceedings*. doi: https://doi.org/10.1063/1.5024107

Doddegowda, P., Bychkovsky, A.L. and George, A.R (2006). 'Use of Computational Fluid Dynamics for the Design of Formula SAE Race Car Aerodynamics ', *SAE 2006 World Congress & Exhibition*. doi: https://doi.org/10.4271/2006-01-0807

Drela, M (2013). *XFOIL Subsonic Airfoil Development System*. Available at: https://web.mit.edu/drela/Public/web/xfoil/ [Accessed 2 Nov. 2023].

Drela, M. and Giles, M (1987). 'ISES - a two-dimensional Viscous Aerodynamic Design and Analysis Code', *25th AIAA Aerospace Sciences Meeting*. doi: https://doi.org/10.2514/6.1987-424

Fareeq, S (2015). *Aerodynamic Evaluation of Racing Wings of a Formula Car*. MSc Project Report. University of Hertfordshire. Available at: https://www.researchgate.net/publication/290964900 [Accessed 18 Feb. 2023].

FIA Foundation (2024). *FIA Foundation | Safe Motor Sport*. Available at: https://www.fiafoundation.org/our-work/safe-motor-sport [Accessed 2 Jun. 2023].

Formula 1 (2019). *F1 Firsts: Aerodynamic Wings*. Available at: https://www.formula1.com/en/latest/video.f1-firsts-aerodynamic-wings.6060943098001.html [Accessed 18 May 2023].

Formula SAE (2024). *Formula SAE.* Available at: https://www.fsaeonline.com [Accessed 18 Nov 2023].

Gupta, S. and Saxena, K (2017). 'Aerodynamics Analysis of a Formula SAE Car ', *13th International Conference on Heat Transfer*. Slovenia, 17-19 July. Available at: http://hdl.handle.net/2263/62356 [Accessed 9 Mar. 2023].

Hasanovic, V (2018). *Formula 1 Aerodynamics - Introduction - F1technical.net*. Available at: https://www.f1technical.net/features/21555 [Accessed 13 Apr. 2023].

Hetawal, S., Gophane, M., Ajay, B.K. and Mukkamala, Y (2014). 'Aerodynamic Study of Formula SAE Car', *Procedia Engineering '12th Global Congress on Manufacturing and Management'*, 97, pp.1198–1207. doi: https://doi.org/10.1016/j.proeng.2014.12.398

Houghton, E.L. and Carpenter, P.W (2003). *Aerodynamics for Engineering Students*. 5th edn. Oxford: Butterworth - Heinemann.

Hu, H.H (2012). 'Computational Fluid Dynamics', In: P.K. Kundu, I.M. Cohen and D.R. Dowling, eds., *Fluid Mechanics 5th Edition*. Academic Press, pp.421-472. doi: https://doi.org/10.1016/C2009-0-63410-3

Igglezakis, D (2016). Αξιολόγηση και Πιστοποίηση του Κώδικα Υπολογιστικής Ρευστομηχανικής *GALATEA*. Diploma Thesis. Technical University of Crete. doi: https://doi.org/10.26233/heallink.tuc.66291

Jabalera López, B (2010). *Analysis and Design of a Functional 3D-CAD Seat Model*. Diploma Thesis. Graz University of Technology. Available at: http://hdl.handle.net/2099.1/9942 [Accessed 27 Oct. 2023].

Jackson, F (2018). 'Aerodynamic Optimisation of Formula Student Vehicle Using Computational Fluid Dynamics', *Fields: Journal of Huddersfield Student Research*, 4(1). doi: https://doi.org/10.5920/fields.2018.02

Jalappa, G (2015). *Design and Optimization of Undertray for Formula SAE Race Car Using CFD Analysis*. Master Thesis. University of Texas. Available at: https://docplayer.net/196972029-Design-and-optimization-of-undertray-for-formula-sae-race-car-using-cfd-analysis-girish-bangalore-jalappa.html [Accessed 3 Apr. 2023].

Katz, J (1995). *Race Car Aerodynamics : Designing for Speed*. 2nd ed. Cambridge, MA: Bentley Publishers.

Katz, J (2006). 'Aerodynamics of Race Cars ', *Annual Review of Fluid Mechanics*, 38(1), pp.27–63. doi: https://doi.org/10.1146/annurev.fluid.38.050304.092016

Kerkhoven, J.D.G (2008). *Design of a Formula Student Race Car Chassis*. Master Thesis. Eindhoven University of Technology. Available at: https://www.academia.edu/38764744 [Accessed 4 Oct. 2023].

Kurec, K., Remer, M. and Piechna, J (2019). 'The Influence of Different Aerodynamic Setups on Enhancing a Sports car's Braking', *International Journal of Mechanical Sciences*, 164, p.105140. doi: https://doi.org/10.1016/j.ijmecsci.2019.105140

Leishman, J.G (2023). *Airfoil Geometries*. Available at: https://eaglepubs.erau.edu/introductiontoaerospaceflightvehicles/chapter/airfoil-geometries/ [Accessed 28 Mar. 2023].

Leloudas, S (2015). *On the Optimal Design of Airfoils.* Diploma Thesis. Technical University of Crete.

Leloudas, S.N., Eskantar, A.I., Lygidakis, G.N. and Nikolos, I.K (2020). 'Low Reynolds Airfoil Family for Small Horizontal Axis Wind Turbines Based on RG15 Airfoil'. *SN Applied Sciences,* 2(371). doi: https://doi.org/10.1007/s42452-020-2161-1.

Loução, R., Duarte, G.O. and Mendes, M.J.G.C (2022). 'Aerodynamic Study of a Drag Reduction System and Its Actuation System for a Formula Student Competition Car'. *Fluids,* 7(9), p.309. doi: https://doi.org/10.3390/fluids7090309.

Luu, V (2015). *Methodology Development for Parametric CAD Modeling in CATIA V5 to Aid Simulation Driven Design Using Turbine Volute as a Case Study*. Master Thesis. Linköping University. Available at: https://www.semanticscholar.org/paper/Methodology-development-for-parametric-CAD-modeling-Luu/b75d892d7f9e6932e074319b9f7d420f3c2487a1 [Accessed 22 Nov. 2023].

Mercedes-AMG Petronas Formula One Team (2022). *What Is Downforce and Why Is It so Important in F1?* Available at: https://www.youtube.com/watch?v=edZycMFeEkU [Accessed 13 Apr. 2023].

Milliken, W.F. and Milliken, D.L (1995). *Race Car Vehicle Dynamics*. Warrendale, Pa, U.S.A.: Sae International.

Mortel, F (2003). *Cranfield Team F1: The Front Wing*. MSc Thesis. Cranfield University. Available at: https://docplayer.net/11114204-Cranfield-university-f-mortel-cranfield-team-f1-the-front-wing-school-of-engineering-cranfield-college-of-aeronautics-msc-thesis.html [Accessed 5 Jun. 2023].

Moye, J (2022). *The Science behind the next-gen FORMULA 1 Car*. Available at: https://www.amazon.science/latest-news/the-science-behind-the-next-gen-2022-f1-car [Accessed 26 Nov. 2022].

Nasir, R.E.M., Mohamad, F., Kasiran, R., Adenan, M.S., Mohamed, M.F., Mat, M.H. and Ghani, A.R.A (2012). 'Aerodynamics of ARTeC's PEC 2011 EMo-C Car ', *Procedia Engineering 'International Symposium on Robotics and Intelligent Sensors 2012 (IRIS 2012)'*, 41, pp.1775–1780. doi: https://doi.org/10.1016/j.proeng.2012.07.382

Nichols, J (2021). *Downforce in F1: the King of Formula 1 Physics*. Available at: https://www.cmcmotorsports.com/blogs/the-drift/downforce-in-f1-the-king-of-formula-1-physics [Accessed 3 Dec. 2022].

Novo, E (2018). *The Potential of CATIA in Structural Design*. Diploma Thesis. Universitat Politècnica de València. Available at: http://hdl.handle.net/10251/112821 [Accessed 22 Nov. 2023].

Oxyzoglou, I (2017). *Design & Development of an Aerodynamic Package for an FSAE Race Car*. Diploma Thesis. University of Thessaly. doi: http://dx.doi.org/10.13140/RG.2.2.24595.37920/1

Pakkam, S.S (2011). *High Downforce Aerodynamics for Motorsports.* Master Thesis. North Carolina State University.

Parmar, P., Parikh, M., Johny, N. and Sharma, S (2018). 'Aerodynamic Optimization of Formula Student Car', *International Journal of Creative Research Thoughts (IJCRT)*, 6(2). Available at: https://www.researchgate.net/publication/341575449_Aerodynamic_Optimization_of_Formula_Student_Car [Accessed 1 Apr. 2023].

Partridge, J (2021). *How Do Formula 1 Front Wings Work? | Formula 1 Technology*. Available at: https://f1chronicle.com/how-do-formula-1-front-wings-work-f1-technology/ [Accessed 20 Feb. 2023].

Paulius, S (2022). *A Legend Who Revolutionized Formula One – Colin Chapman*. Available at: https://dyler.com/blog/38/a-legend-who-revolutionized-formula-one-colin-chapman [Accessed 12 Mar. 2023].

Pehan, S. and Kegl, B (2002). 'Aerodynamics Aspects of Formula S Racing Car', *7th International Design Conference.* Dubrovnik. pp. 1109-1118. Available at: https://www.designsociety.org/publication/29705/Aerodynamics+Aspects+of+Formula+S+Racing+Car [Accessed 3 Mar. 2023]

Pretorius, L (2022). *What Is Ground Effect in F1?* Available at: https://onestopracing.com/what-is-ground-effect-in-f1/ [Accessed 4 Apr. 2023].

Prom Racing (2021). *Technical Presentations – Prom Racing Team*. Available at: https://promracingteam.com/technical-presentations/ [Accessed 8 Feb. 2024].

Promtong, M., Priyadumkol, J., Namchanthra, S. and Suvanjumrat, C (2020). 'Investigation of Aerodynamic Performance of Four Potential Airfoils for a Formula SAE Car: a 2D Validation Study', 3*4th Conference of the Mechanical Engineering Network of Thailand.* Thailand, 15-17 July. Available at: https://www.researchgate.net/publication/343053885 [Accessed 12 Apr 2023]

Rab, M.F.U., Alam, M.J., Akhlaque, A. and Mahrukh, M (2018). 'Comparative Analysis of High-Lift Airfoils for Motorsports Applications', *12th International Conference on Advances in Fluid Mechanics.* Slovenia doi: http://dx.doi.org/10.2495/AFM180171

Rad, M. and Kazemi, F.J (2001). 'Effect of Camber and Thickness on the Aerodynamic Properties of an Airfoil in Ground Proximity', *International Journal of Engineering,* 14(280).

Raymer, D.P (1992). *Aircraft Design : A Conceptual Approach.* 2nd ed. Washington, DC: American Institute of Aeronautics and Astronautics, Inc.

Reza, M.M.S., Mahmood, S.A. and Iqbal, A (2016). 'Performance Analysis and Comparison of High Lift Airfoil for Low Speed Unmanned Aerial Vehicle', *International Conference on Mechanical, Industrial and Energy Engineering.* Bangladesh, 26-27 December.

Riblett, H (1988). *What Are Wortman Airfoils??*.

Roy, S., Das, B. and Biswas, A (2021). 'Influence of Camber Ratio and Thickness Ratio on the Airfoil Performance', In: P. Pradhan, B. Pattanayak, H.C. Das and P. Mahanta, (eds.) *Recent Advances in Mechanical Engineering*. Singapore: Springer. doi: https://doi.org/10.1007/978-981-15-7711-6_72

SAE International (2024). *Standards Development*. Available at: https://www.sae.org/standards/development [Accessed 5 Oct. 2023].

Sánchez Alacid, J.F (2009). *Parameter Studies of a Machine Feed Axis Testbed in Time Domain by Application of Multibody Simulation*. Diploma Thesis. Karlsruhe Institute of Technology. Available at: http://hdl.handle.net/10317/953 [Accessed 10 Dec. 2023].

Selig, M (2023). *Michael Selig*. Available at: https://www.michaelselig.com [Accessed 9 Aug. 2023].

Selig, M.S., John Francis Donovan and David Bruce Fraser (1989). *Airfoils at Low Speeds.* Virginia Beach: H. A. Stokley, Cop.

Seljak, G (2008). *Race Car Aerodynamics*. University of Ljubljana. Available at: https://docplayer.net/21172064-Race-car-aerodynamics-gregor-seljak.html [Accessed 3 Mar. 2023]

Senthilkumar, P.B., Parthasarathy, M., Aravind, L., Narayanan, R.G.S., Vegesh, B. and Sam Nelson, D.R (2021). 'Design and Analysis of a Rear Diffuser in a Sedan Car', *Materials Today: Proceedings*, 59(2), pp.1324–1339. doi: https://doi.org/10.1016/j.matpr.2021.11.542

Soliman, P.A., Martins, M.E.S. and Schommer, A (2015). 'Formula SAE Aerodynamics: Design Process with Focus on Drivability', *24th SAE Brasil International Congress and Display*. doi: https://doi.org/10.4271/2015-36-0359

Somerfield, M. and Piola, G (2023). *How F1's New Rules Era Has Impacted Front Wing Philosophy*. Available at: https://www.autosport.com/f1/news/how-f1s-new-rules-era-has-impacted-front-wing-philosophy/10422705/ [Accessed 18 Jan. 2024].

Stinton, D (1983). *The Design of the Aeroplane*. Oxford: BSP Professional Books.

Toet, W (2013). 'Aerodynamics and Aerodynamic Research in Formula 1', *The Aeronautical Journal*, 117(1187), pp. 1-26. doi: https://doi.org/10.1017/S0001924000007739

Tremayne, D (2006). *The Science of Formula 1 Design*. Sparkford: Haynes Publishing.

Tzanakis, A (2012). *Conceptual and Aerodynamic Design of an Urban Vehicle*. Diploma Thesis. Technical University of Crete. doi: https://doi.org/10.26233/heallink.tuc.12918.

Upadhye, S., Khairwa, D., Nagpure, M., Mangrulkar, A., Deotale, A. and Nagpure, H (2021). 'Estimation of Drag and Down Forces using Aerodynamic Profile on Formula Student Vehicle', *International Research Journal of Engineering and Technology (IRJET)*, 8(8), pp. 188-193 Available at: https://www.irjet.net/volume8-issue08 [Accessed 18 Feb. 2023].

Vadgama, T.N., Patel, A., Thakkar, D. and Vala, J (2015). 'Structural Analysis of Formula One Racing Car', *International Journal of Advance Research in Engineering,* 2(5).

Vardhan, H (2023). *F1 Front Wing: the Key to Aerodynamic Efficiency*. Available at: https://www.linkedin.com/pulse/f1-front-wing-key-aerodynamic-efficiency-harsha-vardhan/ [Accessed 23 Feb. 2023].

Versteeg, H. and Malalasekera, W (2007). *An Introduction to Computational Fluid Dynamics : the Finite Volume Method*. Harlow: Pearson Education.

Wilson, J (2021). *The Shape That Shapes the Aviation Industry: the Airfoil Shape*. Available at: https://ctipft.com/the-shape-that-shapes-the-aviation-industry-the-airfoil-shape [Accessed 10 Mar. 2023].